A New Absolute Total Cross-Section for Photodisintegration of Beryllium-9

Charles William Arnold

A dissertation submitted to the faculty of the University of North Carolina at Chapel Hill in partial fulfillment of the requirements for the degree of Doctor of Philosophy in the Department of Physics and Astronomy.

Chapel Hill
2011

Approved by:

T. B. Clegg, Advisor

C. R. Howell, Advisor

H. J. Karwowski, Reader

C. Iliadis, Reader

D. Reichart, Reader

Abstract

CHARLES WILLIAM ARNOLD: A New Absolute Total Cross-Section for Photodisintegration of Beryllium-9.
(Under the direction of T. B. Clegg and C. R. Howell.)

Models of the r-process are extremely sensitive to the rate of production of ^{9}Be, because the $\alpha(\alpha n,\gamma)^9$Be reaction is the primary mechanism for bridging the unstable mass gaps at A=5 and A=8 in explosive environments that are rich in neutrons. A sequential two body process of $\alpha+\alpha \rightarrow {}^8\mathrm{Be} + n \rightarrow {}^9\mathrm{Be}$ is the primary channel for synthesis of ^{9}Be. It is impossible to measure this reaction sequence in a laboratory, because no appreciable amount of ^{8}Be ($\tau_{\mathrm{lifetime}} = 10^{-16}$ s) could ever be produced, and then subsequently bombarded with neutrons. However, the $^8\mathrm{Be}(n,\gamma)^9$Be cross-section may be deduced from the $^9\mathrm{Be}(\gamma,n)^8$Be cross-section using the reciprocity theorem. This thesis reports on a new measurement of the $^9\mathrm{Be}(\gamma,n)^8$Be reaction cross section with an unprecedented accuracy, and a precision of ±4.6%. From these new measurements, the astrophysical $\alpha(\alpha n,\gamma)^9$Be reaction rate has been determined with similar accuracy and precision. This new rate will give insights into the conditions necessary for the r-process to occur in explosive environments like Type II supernovae.

Table of Contents

List of Tables

List of Figures

1 Introduction and Motivation

1.1 Introduction

Nucleosynthesis is a general term for creation of new nuclei, by processes which add or remove mass and/or charge from an existing nucleus. It is useful to distinguish three general types of nucleosynthesis, though various classification schemes exist. *Big-bang nucleosynthesis* [Fie06], the first type, leads to the synthesis of light elements within the first few minutes of the universe. *Stellar nucleosynthesis* [Sie02], the second type, refers to nuclear reactions that occur within stars. This includes the proton-proton chain [Sal52], the CNO cycle [Cau62], the 3-α process [Nom85, Lan86], and a slow neutron capture process called "s-process" [Gal98]. The third type is *explosive nucleosynthesis*, which generally includes the synthesis of nuclei formed in explosive environments characterized by high-temperatures and short time-scales. These process include a rapid neutron capture process (r-process) [Woo92], a rapid proton capture process (rp-process) [van94] and a rapid alpha reaction processes (α-process) [Woo92]. *Big-bang nucleosynthesis* was a single event which happened at the beginning of the universe. The present discussion will focus on the second and third types of nucleosynthesis which are currently taking place throughout the universe.

1.2 Nucleosynthesis Models

In stars, the accumulation of nuclei heavier than iron produced by *stellar nucleosynthesis* reactions is relatively slow. Of particular interest to this discussion are the reaction products specific to the s-process. The s-process is responsible for almost half of the abundance of nuclei heavier than iron. However, when s-process abundances are subtracted from solar-system abundances, the residual abundance pattern has structure. Two broad peaks are observed at A $\cong$ 130 and A $\cong$ 190. Furthermore, some of these elements cannot be produced by slow neutron-capture at all (see Fig. 1.1). The origin of this structure in the plot of mass

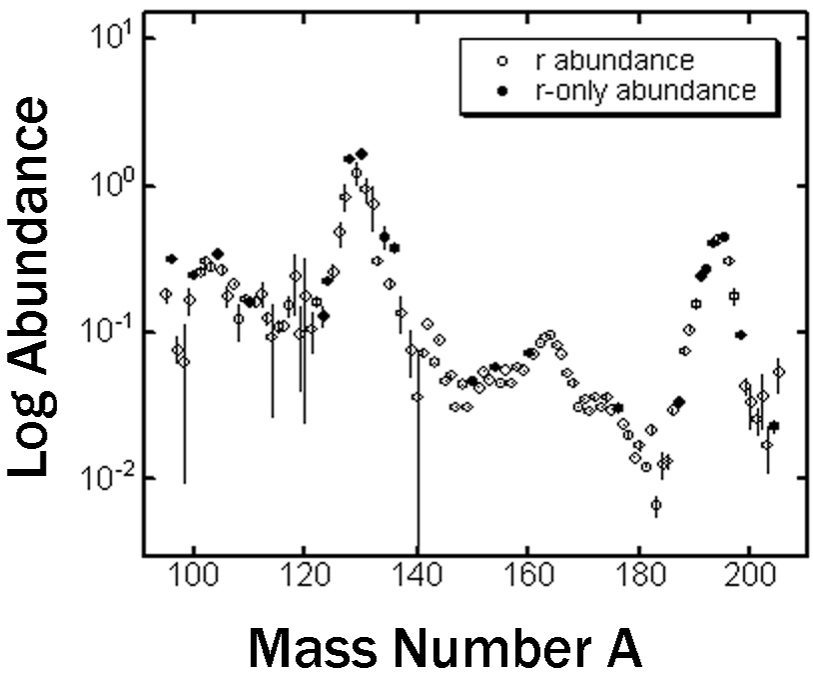

Figure 1.1: Plot of relative nuclear abundance, normalized to Si = 10^6, vs. mass number, A. Structure is observed in the region of heavy elements after having accounted for s-process elements. Dark circles are abundances which are only produced by the r-process. Image from Ref. [Ili07]; used with permission.

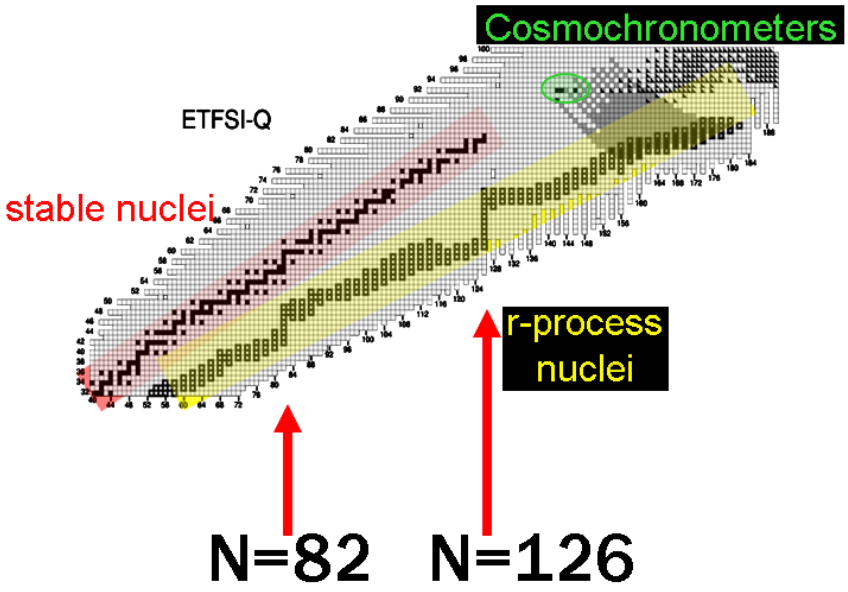

Figure 1.2: Stable nuclei and r-process path nuclei are highlighted in red and yellow respectively. The heavy nuclei uranium and thorium (highlighted green) can only be produced by the r-process. The neutron magic shell closures at N=82 and N=126 become waiting points during the r-process. The full shells resist the addition of more neutrons, which allows for eventual β-decay. Image from Ref. [Ili07]; used with permission.

abundance is the r-process.

Explosive nucleosynthesis, like the r-process, likely happens in supernovae [Woo94], in neutron star mergers [Fre99], and presumably in any high-temperature (T $\approx$ 1.0 $T_9 = 10^9$ K) and high neutron flux ($\phi \approx 10^{22}$ n/(cm^3·s)) environment. At present, the case for an indisputable r-process site has not been been made. A recent analysis argues for the necessity of multiple sites [Qia07]. Supernovae have long been cited as potential r-process factories because they produce the explosive conditions necessary for the r-process, and they occur with enough frequency to make substantial abundances. In what follows, it will be shown that the abundance of heavy nuclei coming from explosive nucleosynthesis at a type II supernova site is intrinsically linked to the rate of production of ^{9}Be.

1.2.1 Supernovae

As mentioned previously, supernovae provide the explosive environment that r-process requires. However, not every supernova supports the r-process. *Type-I* supernovae lack the presence of hydrogen, which distinguishes them from *Type-II* supernovae, which do contain hydrogen. *Type-II* supernovae, therefore, represent younger and more massive stars than *type I's*. Furthermore, *type-Ia* supernovae represent an accreting white-dwarf plus companion as the explosion mechanism, while types *Ib*, *Ic*, and *type II* all represent core-collapse supernovae

[Arn96]. *Type-II* supernovae are believed to produce suitable conditions for the r-process.

The behavior of a core-collapse supernovae has been explained by Woosley [Woo05], and so only important details will be repeated here. A star of 8 to 25 solar masses passes through the stages of hydrogen, helium, carbon, neon, oxygen, and silicon fusion at its core, continuously growing hotter and more dense. The core eventually becomes an iron-group core of about 1.4 solar masses. The energy to resist gravity's pressure is lost through neutrino emission, electron capture and photodisintegration. An Earth-sized iron-core, collapses with a velocity of ~ 1/4 c into a single neutron-rich nucleus about 30 km in diameter, supported by nuclear repulsion. The sudden cessation of collapse generates a rebounding shock wave which ultimately stalls as it attempts to push through the matter outside of the core that is still in-falling. The proto-neutron star (PNS) briefly continues accreting matter while radiating ~ 10^{53} erg (10^{46} J) in the form of neutrinos - nearly 10% of its rest mass. Convection is required at this point to spur on the supernova explosion. For those who model supernovae, this last point has made the effort to simulate explosions from core-collapse very difficult. Recent work has made advances in the ability to model the core-collapse in three-dimensions [Nor10]. Rotation and magnetism likely have roles in the explosion mechanism as well. The stage is now set for the r-process.

1.2.2 The r-process

The r-process produces about half of the abundance of nuclei heavier than iron [Woo05]. It requires an environment where neutron captures occur so rapidly that the newly formed nucleus does not have enough time to β-decay before capturing another neutron. Eventually, the neutron rich nuclei approach the neutron dripline, or a nuclear shell is filled (at the "magic" numbers), at which point further neutron captures are so unstable to neutron-decay that β-decays will occur. In the latter case, the nucleus begins to wiggle up the chart of nuclides, increasing in proton number, until the nucleus is stable enough to capture neutrons again. The r-process turns off after a matter of seconds, leaving an abundance of heavy neutron-rich nuclei far from stability. These nuclei, in turn, begin their journey to stability, converting neutrons to protons via β-decay.

Constraining the location and frequency of the r-process has the benefit of providing a means for dating the universe. Because the r-process is the only mechanism which can produce uranium and thorium isotopes, and because the ratio of these abundances appears to be almost insensitive to the parameters of the explosive environment [Ots03], understanding the sites and the frequency with which the r-process occurs would provide a nuclear cosmochronometer. Improvements to understanding the r-process will necessarily involve astrophysical observations and improvements to nuclear reaction data.

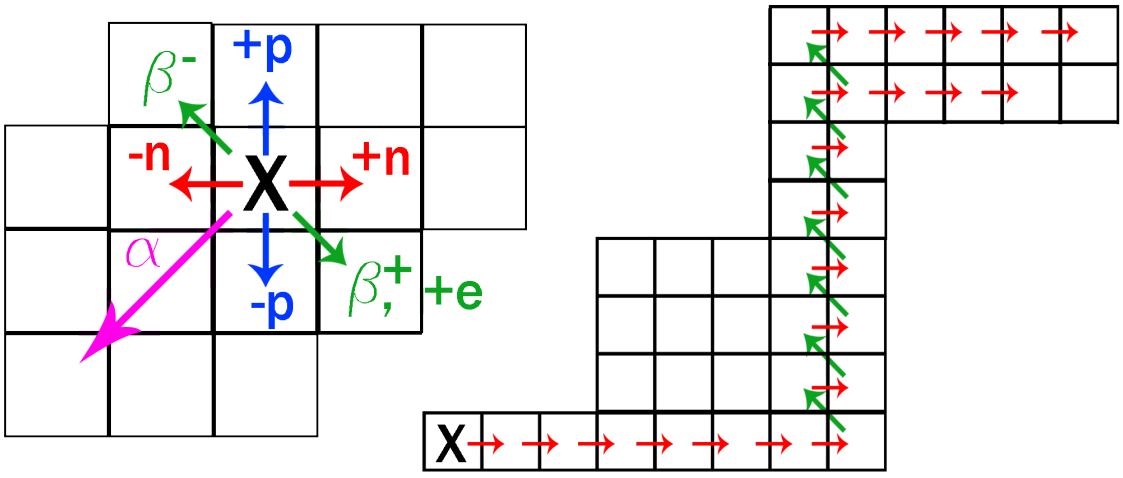

Figure 1.3: (left) The various processes that can change the nucleon number of nucleus "X" include neutron capture, neutron decay, proton capture, proton decay, alpha capture and alpha decay. β^- decay, β^+ decay, and electron capture convert neutrons to protons, or vice versa without changing the nucleon number. (right) During the r-process, neutron capture happens so rapidly that very neutron rich nuclei are quickly synthesized. At some point, β^- decay wins out and nuclei wiggle up magic shell closures until neutron capture can take over again.

1.2.3 α-process

The α-process [Woo92] is a brief period of charged-particle reactions (CPR) and neutron capture which starts after the supernova explosion has cooled to 5 billion kelvin from an initial 10 billion kelvin over the course of a few seconds. In this stage of nucleosynthesis, a reaction path is needed which bridges the unstable mass gaps at A = 5 and A = 8. In the given scenario, the most efficient path to A > 8 is $\alpha + \alpha \rightarrow {}^8\text{Be}+n \rightarrow {}^9\text{Be}+\alpha \rightarrow {}^{12}C + n$ [Ter01]. As cooling continues it is this reaction which largely establishes the neutron-to-seed-nucleus ratio for the coming r-process. The r-process is extremely sensitive [Sas06] to the ratio of seed-nuclei to free neutrons. Too few seed-nuclei will produce a lacking abundance, while too many seed nuclei produced in the α-process will starve the r-process of neutrons. Thus, establishing a precise rate for the formation of ^{9}Be via the $\alpha(\alpha n, \gamma)^9$Be reaction is required for modeling nucleosynthesis in supernovae accurately. Figure 1.4 from Ref. [Woo05] gives a detailed description of this stage of nucleosynthesis.

1.3 The ^{9}Be Nucleus

The ^{9}Be nucleus is the only stable configuration for nine nucleons. Much work has gone into studying the possible arrangements of this system. Many works [Sho99, Ita01, Des01, Des02, Ita03, Fre04] have taken nuclear clustering and molecular orbit model approaches

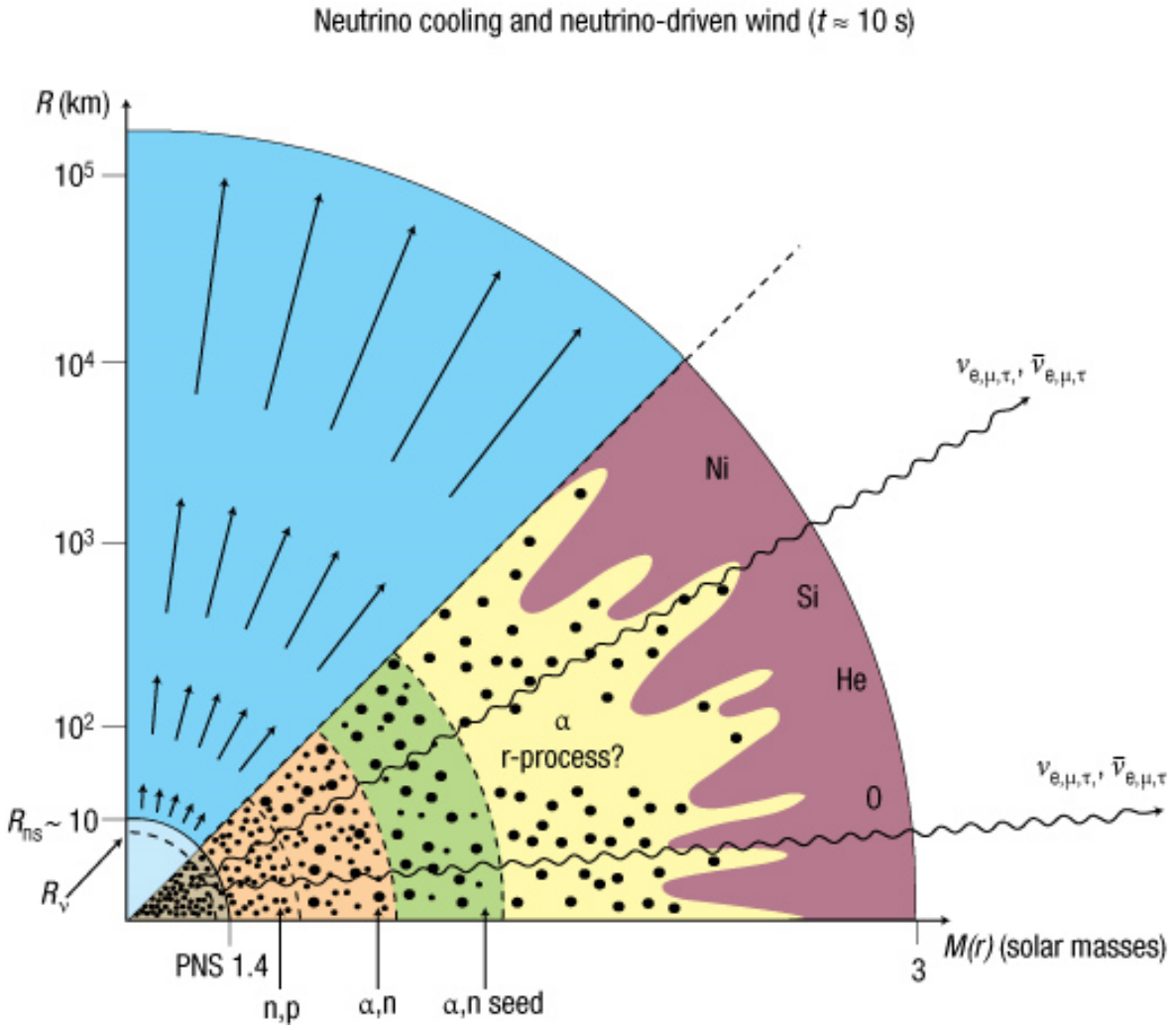

Figure 1.4: Neutrinos (ν_e,ν_μ,ν_τ and their antiparticles) drive a wind from the surface of the cooling PNS creating the r-process isotopes. The wind begins as a flux of neutrons and protons lifted from the surface of the PNS (here 1.4 solar masses and 10 km in radius) by neutrinos originating at the neutrinosphere (R_ν). As these nucleons flow out, an excess of neutrons is created by the capture of antineutrinos on protons. As the nucleons cool, all the available protons combine with neutrons to make α-particles until one is left, in the orange region, with a mixture of only α-particles and unbound neutrons. Further cooling leads to the assembly of a few α-particles into nuclei in the iron group (seed) by reactions involving neutrons and α-particles (green region). As the temperature declines still further, from 3 billion kelvin to 1 billion kelvin, all neutrons are captured on this seed making the heavy r-process nuclei. Because the efficiency of the reactions that assemble α-particles into seed increases with the density, lower density in the wind keeps the seed number small and increases the number of neutrons that can be captured on each. Figure and caption from Ref. [Woo05]; used with permission.

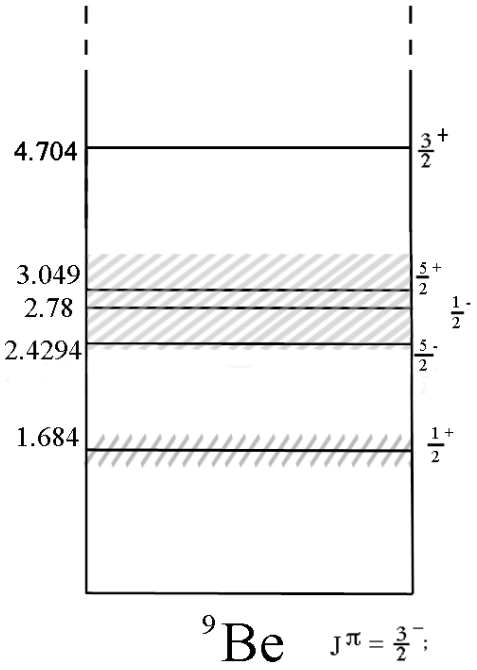

Figure 1.5: Energy levels of ^{9}Be. Image adapted from [Til04].

to describe ^{9}Be. This section will summarize recent experimental information about the structure of the ^{9}Be nucleus in addition to some relevant model descriptions.

1.3.1 Structure of ^{9}Be

The ^{9}Be nucleus is an ensemble of 4 protons and 5 neutrons. Measurements of inelastic scattering of electrons, protons, ^{3}He, and ^{4}He have sought to resolve the excited states of ^{9}Be. This discussion of excited states in ^{9}Be will be limited to a few of the lowest excited states because only these states are relevant for the present astrophysical discussions. The five lowest excited states in ^{9}Be are shown in Fig. 1.5.

The ^{9}Be nucleus is often referred to as a Borromean nucleus. A Borromean structure consists of three components which are linked together in such a way that removing one of the links leaves the remaining components unlinked (see Fig 1.6). Given the instability of the ^{8}Be ($\tau = 10^{-16}$ s) and ^{5}He ($\tau = 10^{-21}$ s) systems, ^{9}Be is clearly a Borromean construction of two α-particles and a neutron. In the next section I will mention some useful approaches for describing a nuclear system like ^{9}Be.

1.3.2 Clusters and Nuclear Molecules

The idea of clustering in nuclei originated in the late 1920's. The proton, α, and β particles had been identified by this time, and it was thought by some that the alpha particle

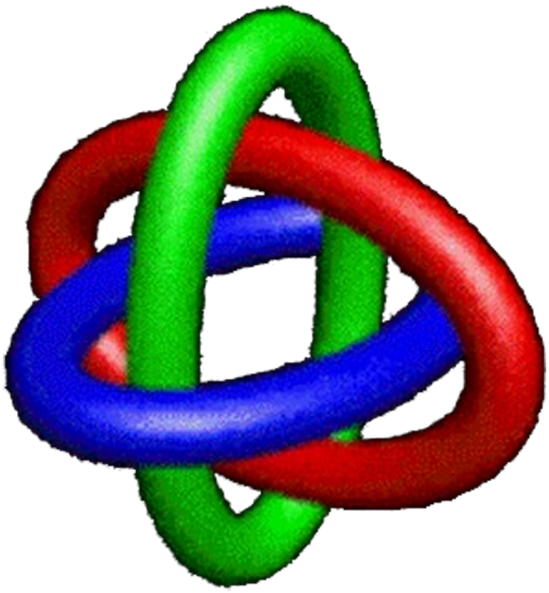

Figure 1.6: A three-dimensional representation of Borromean Rings. Removing one link leave the remaining rings unlinked.

was a collection of 4 protons and two nuclear electrons [Pag30]. Early attempts to describe nuclei as composed of groups of alpha particles were soon abandoned with the discovery of the neutron in 1932 [Cha32] (Incidentally, the neutrons were produced by bombarding ^{9}Be with α-particles from polonium). This discovery ushered in single-particle descriptions of nuclei, and clustering models were not significantly investigated again until the mid 1950's [Per56]. Within the last 30 years, complex cluster structures have been identified in nuclei, and cluster models have predicted states in N=Z (called α-conjugate or self-conjugate) light nuclei that are not reproduced by the shell model [vO06]. Clustering in nuclei conceptually leads to a molecular description of nuclei. The addition of so called "valence neutrons" to otherwise α-conjugate nuclei are observed to enhance nuclear stability in multi-cluster states where neutrons become the analog of covalently bonded electrons in atoms [vO06]. Using this formalism, it may be understood ^{9}Be to behave like two α-particles and with an orbiting neutron. While this description is simplistic, it still offers useful insights into the structure of ^{9}Be.

Why Clusters?

Nuclear properties can be derived using the A-body Schrödinger equation,

$$\left[-\frac{\hbar}{2M}\sum_{i=1}^{A}\nabla_i^2 + V(r_1,...,r_A)\right]\psi(r_1,...,r_A) = i\hbar\frac{\partial}{\partial t}\psi(r_1,...,r_A,t). \tag{1.1}$$

Here V is a potential and r_i represents space, spin and isospin for the i_{th} nucleon.

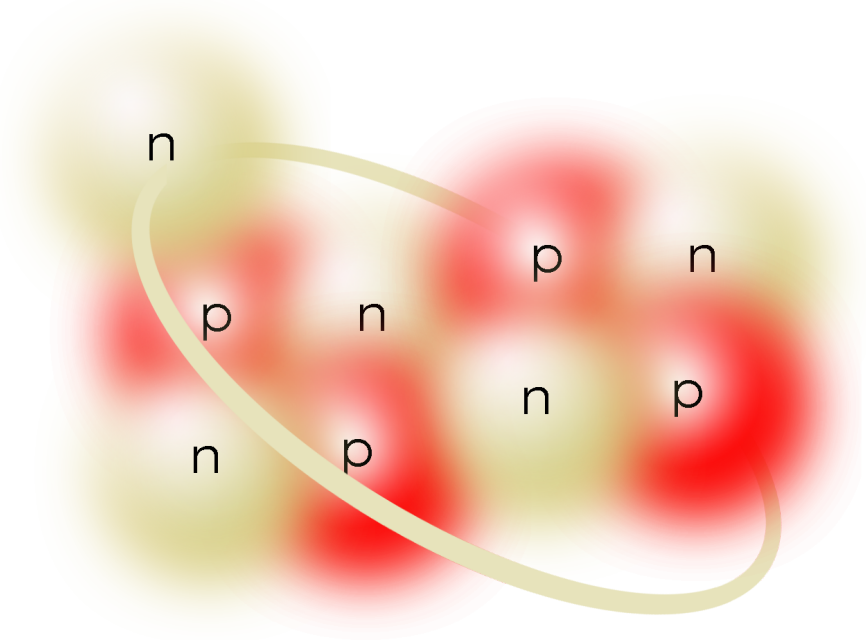

Figure 1.7: A neutron orbiting two alpha clusters.

Assuming only a two-body, non-relativistic potential of the form:

$$V(r_1, ..., r_A) = \sum_{i=1}^{A} \sum_{j>i}^{A} V_{ij}, \tag{1.2}$$

and combining 1.1 and 1.2 yields

$$\left[-\frac{\hbar}{2M} \sum_{i=1}^{A} \nabla_i^2 + \sum_{i=1}^{A} \sum_{j>i}^{A} V_{ij} \right] \psi(r_1, ..., r_A) = i\hbar \frac{\partial}{\partial t} \psi(r_1, ..., r_A, t) \tag{1.3}$$

for the A-body Schrödinger equation.

Now it becomes clear why a cluster model is attractive. The number of degrees of freedom can be reduced by a factor of four by considering interacting alpha particles rather than interacting protons and neutrons [Per56]. The 8-body problem of ^{8}Be reduces to a two body problem. A 12-body problem like ^{12}C reduces to a three-body problem, and so on.

Though some of the computational advantages of cluster models are diminished by cheaper and faster computing, models that have attempted to handle all nuclear interactions observe clustering effects within nuclei [Fre04]. Certainly, a new and accurate absolute cross section measurement of ^{9}Be$(\gamma, n)^{8}$Be will provide a new basis for comparison with all relevant nuclear models for ^{9}Be.

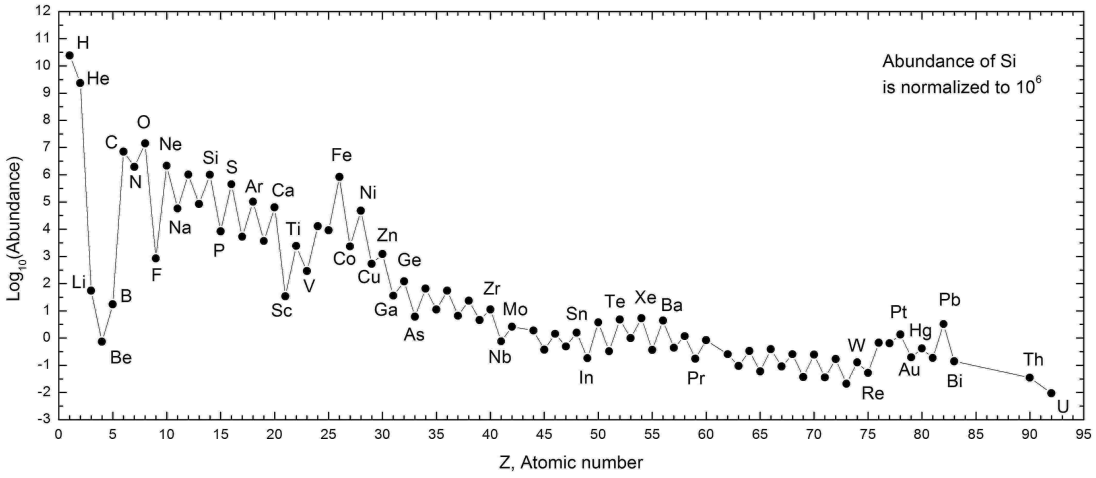

Figure 1.8: ^{9}Be is the least abundant of light nuclei. As Z increases, abundance does not return to the level of ^{9}Be until Niobium (^{93}Nb; Z=41). The abundance of ^{9}Be is comparable to Hg and Pt. Image generated with numerical data from [Lod03].

1.3.3 Nuclear Properties

The ^{9}Be nucleus has unique properties which make it interesting to astrophysics. First, ^{9}Be has the lowest neutron separation energy (S_n) of stable nuclei. Second, it is the least abundant among light nuclei [Lod03](see Fig. 1.8). Finally, the ^{9}Be production reaction is often one of only two three-body reactions considered important for nucleosynthesis. The other three-body reaction is the triple-α reaction.

1.4 Why a new measurement?

Measuring the ^{8}Be$(n,\gamma)^{9}$Be reaction is impossible because of the short lifetime of the ^{8}Be nucleus ($\tau_{\text{lifetime}} = 10^{-16}$ s). The ^{9}Be$(\gamma,n)^{8}$Be reaction, however, is measurable, and may be used to deduce the ^{8}Be$(n,\gamma)^{9}$Be cross-section by using the reciprocity theorem. In fact, this reaction has been measured several times previously. Photodisintegration data of ^{9}Be, and analyses are apparently abundant [Rus48, Ham49, Sne50, Mob50, Ham53, Noy54, Edg57, Gib59b, Jak61, Joh62, Ber67, Cle68, Sal70, Hug75, Fuj82, Bar83, Kue87, Gor92, Efr98, Bar00, Uts00, Muk05, Esh05, Bur10], which invites the question, "why should it be measured again?". The answer is twofold. First, abundance predictions are incredibly sensitive to the choice of $\langle\alpha\alpha n\rangle$ rates that currently exist. Figure 1.9 shows abundance yields that are different by orders of magnitude for different rates [Ang99, Sum02, Cau88]. Notice that a 25% change in the NACRE rate can translate to a difference of nearly two orders of magnitude or more using the parameters shown. Surely a reaction rate which exhibits this kind of sensetivity must be measured as accurately as possible, and it can only be measured by accurately

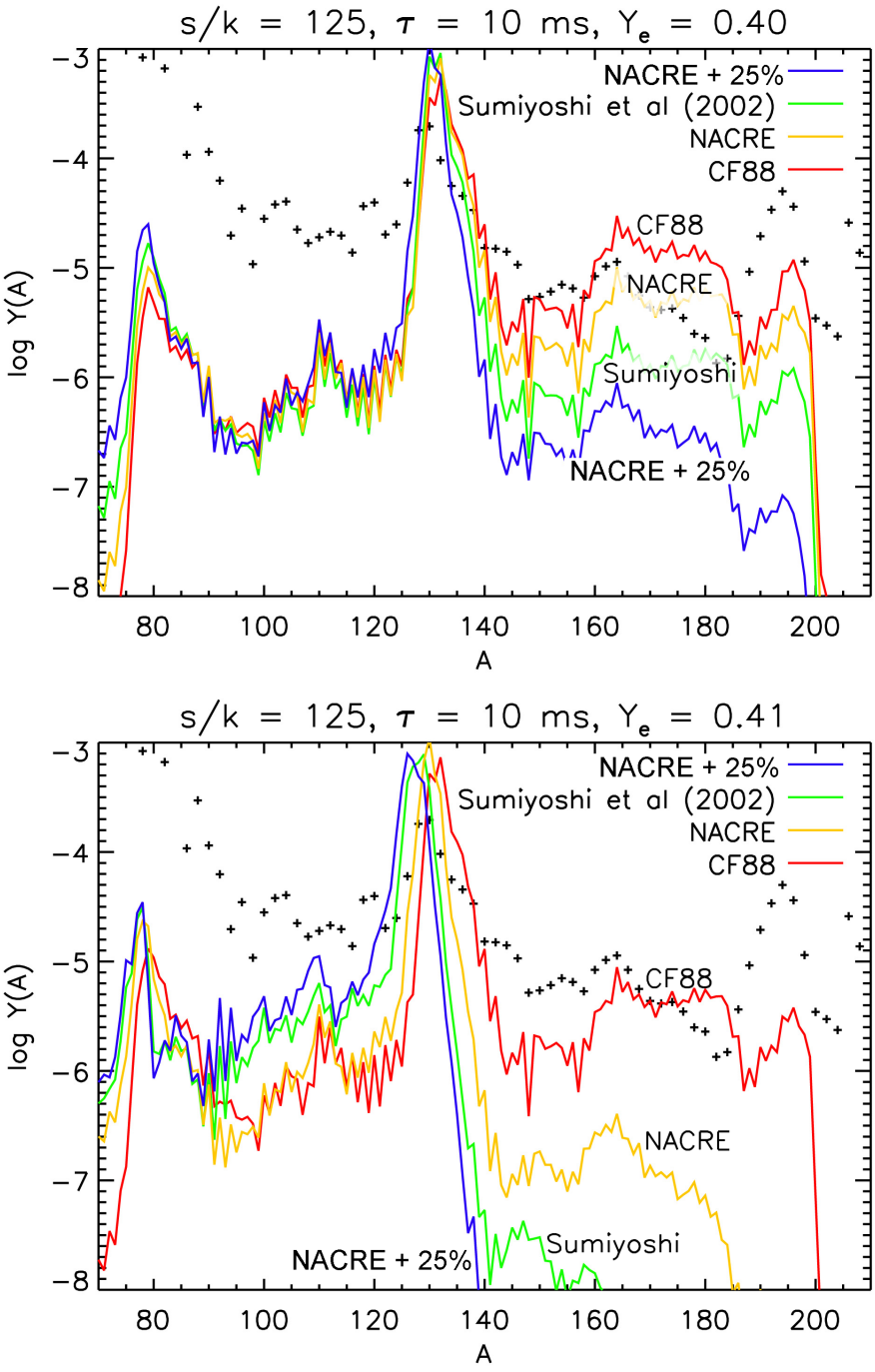

Figure 1.9: Plots of expected abundance patterns using identical simulations with the only variant being different $\langle \alpha\alpha n \rangle$ rates ([Ang99], [Cau88], [Sum02]). Points are observed abundance. Abundance can vary by orders of magnitude for even modest differences in the $\langle \alpha\alpha n \rangle$ rate which is used. Image from [Sur10].

determining the ^{9}Be$(\gamma, n)^{8}$Be cross section.

Second, very accurate (γ, n) cross-section measurements have been made possible by the combination of new intense sources of γ-rays, and neutron detectors with large solid angle coverage and high efficiencies. The Triangle Universities Nuclear Laboratory's (TUNL) high intensity γ source (HIγS) [Lit97] is able to produce monoenergetic γ-ray beams. These beams are produced by inverse Compton scattering of free electron laser (FEL) photons, and have nearly Gaussian energy distributions ΔE/E = 1% (FWHM), and flux = 5×10^{6} $\gamma \cdot \mathrm{cm}^{-2}$ s^{-1}. Our laboratory also has a Model IV inventory sample counter (INVS), on loan from Los Alomos National Laboratory (LANL), which provides a maximum neutron detection efficiency of nearly 60%.

Measurements of the photodisintegration of ^{9}Be have taken many forms. The γ-ray sources used have come from radioactive isotopes, bremsstrahlung sources and virtual photons from inelastic electron scattering. Only recently has production of γ-rays from inverse Compton scattering of FEL photons become a new standard in γ-ray production. Furthermore, accurate cross section measurements involving neutral particles have long been plagued by small and/or uncertain detection efficiencies.

A recent cross section measurement of photodisintegration of ^{9}Be by Utsunomiya *et al.* [Uts00] used γ-rays from inverse Compton scattering and a ~6% efficient neutron detector with nearly 4π solid angle coverage. The resonance widths, locations, and transition strengths derived from their data were used to calculate a new astrophysical rate which, in the temperature region most important for the r-process, exhibited comparable behavior to a standard NACRE rate calculation [Ang99]. However, the γ-ray beams produced for the Utsunomiya measurement exhibited a saw-tooth energy distribution, with an energy spread of "a few percent" [Uts00]. The much narrower 1% energy spread of our γ-ray beam at HIγS makes possible much more detailed mapping of the cross section in the astrophysically important energy range of 1.5 MeV $\leq$ E_{γ} $\leq$ 5.2 MeV.

An even more recent measurement from Burda *et al.* [Bur10] used virtual photons from inelastic electron scattering to excite a ^{9}Be target, and interpreted the resonance parameters of the first excited state. They found a transition strength for the first excited state with a magnitude of about 1/2 of that of Ref. [Uts00], but in agreement with other (e, e') measurements [Kue87].

A direct measurement of the cross section for photodisintegration of ^{9}Be using the high resolution γ-ray beam at HIγS that spans from below the two-body threshold (1.6654 MeV) to 5.2 MeV should add clarity to the situation and permit a new and accurate determination the astrophysical rate for the $\alpha(\alpha n, \gamma)^{9}$Be reaction. The following chapters will discuss the experimental details (Chap. 2), the methods used and precision attained in characterizing the neutron detector (Chap. 3), the data collection (Chap. 4), our new ^{9}Be$(\gamma, n)^{8}$Be cross section results (Chap. 5), and a discussion of the $\alpha(\alpha n, \gamma)^{9}$Be rate interpreted from the

data (Chap. 6). Chapter 7 contains appendices that include a description of target preparation methods (Sect. 7.1), tables of $^{9}\mathrm{Be}(\gamma, n)^{8}\mathrm{Be}$ cross-section data (Sect. 7.2), parameters from fits (Sect. 7.3) and the computer code used to determine the $\langle \alpha\alpha n \rangle$ rates which derive from the present fits (Sect. 7.4).

2 The Experiment

2.1 Introduction

Data for the ^{9}Be$(\gamma, n)^{8}$Be reaction were taken at the HIγS facility at TUNL. Our experimental method was as follows. Collimated monoenergetic γ-ray beams of 1.5 MeV$\leq$ E$_\gamma$ $\leq$ 5.2 MeV were incident on a thick ^{9}Be target. An absolute measure of the number of neutrons from the reaction was made using a well-characterized thermalization counter that has a high-efficiency for detecting low-energy neutrons. The absolute flux of the incident γ-rays was measured using a large NaI detector called "*Molly*", which has a total efficiency of 100% for γ-rays in the experimental energy range (1.5 MeV $\leq$ E$_\gamma$ $\leq$ 5.2 MeV). In addition, a heavy water target was bombarded under the same experimental conditions as the ^{9}Be sample for cross-calibrating the ^{9}Be$(\gamma, n)^{8}$Be measurements with the ^{2}H$(\gamma, n)^{1}$H cross-section [Sch05] and for neutron detector efficiency benchmarking. A graphite target was also used at each beam energy to determine beam-induced backgrounds in the neutron detector.

The following sections give details about the experimental methods and their justifications. Section 2.2 provides a detailed experimental overview. Section 2.3 describes the detectors used for this measurement, the manner in which they were characterized, and the precision achieved.

2.2 Experimental Setup

Intense γ-ray beams ($\phi \approx 10^{8}\gamma$/s) are routinely produced at HIγS by inverse-Compton scattering FEL photons from electron bunches circulating in a storage ring [Wel09]. For the present experiment, a high degree of energy-resolution was deemed more important than the highest possible flux. The most important reasons were to map the detailed behavior of the cross section at the three-body (1.573 MeV) and two body (1.6654 MeV) thresholds and across a resonance at 2.431 MeV. Achieving 1% energy resolution meant sacrificing γ-ray flux. The

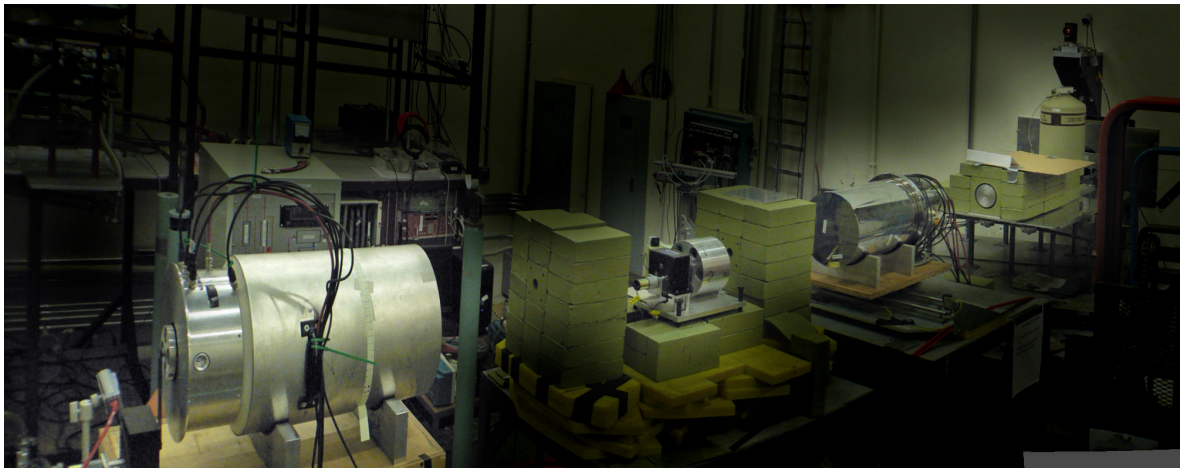

Figure 2.1: Images of the experimental setup for measurement of the ^{9}Be$(\gamma, n)^{8}$Be cross-section at HIγS. Important elements are highlighted and are discussed in the present section.

Target Material	Nominal ℓ (cm)	Density (g/cm^3)	Molar Mass (g/mol)	Nuclei per molecule	# nuclei per cm^2
^{9}Be	2.54	1.848	9.012	1	3.136×10^{23}
Graphite	2.54	1.700	12.01	1	2.892×10^{23}
D_2O	7.59	1.106	20.04	2	5.045×10^{23}

Table 2.1: Targets used in the present experiment and their physical properties. Avogadro's number (N_A=6.022$\times$ 10^{23}) converts moles to number of atoms. The number of nuclei per cm^2 shown does not include a thick target correction (discussed in Sect. 4.6).

present data were taken using beams with $10^5\ \gamma/s\ \leq\ \phi\ \leq 10^6\ \gamma$/s.

A photograph and a schematic diagram of the experimental setup are shown in Figs. 2.1 and 2.2 respectively. The γ-rays were collimated to a diameter of 12 mm by lead collimators that were 30.5 cm thick in a room designated as the "collimator hut". The collimated beam then passed through three thin scintillating paddles which were attached to five photomultiplier tubes (PMT). These acted as a relative γ-ray flux monitor. The γ-rays then entered the experimental room known as the "Gamma-Vault", and passed through a 2.54 cm diameter "clean-up" collimator (CC) which was ~20.3 cm in thickness of lead. The γ-rays travel ~ 1.5 m in air before reaching a second CC (2.54 cm diameter, 20.3 cm thick) that was placed directly in front of the neutron detector, shielding it from γ-rays which may have scattered.

Next, the γ-rays were incident on either one of the three targets (^{9}Be, D_2O, graphite) or nothing as they passed through the neutron detector. To increase the efficiency of data collection, the samples were remotely rotated into position using a four-position Geneva mechanism which assured reproducible alignment on the γ-ray beam axis. Alignment of the target to the beam was confirmed using an alignment pellet and a γ-ray beam imaging system [Sun09] (see

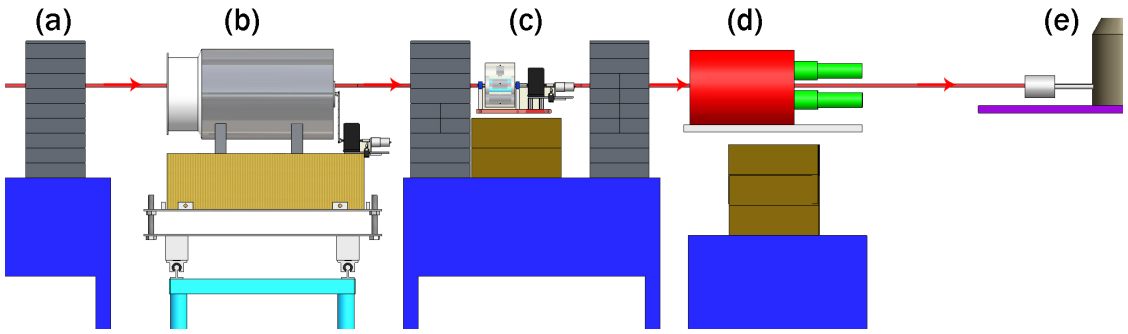

Figure 2.2: Schematic diagram of the experimental setup for the ^{9}Be$(\gamma, n)^{8}$Be reaction measurements at HIγS. After collimation, the γ-ray beam passes through scintillation paddles (not shown) and into the target room. The 1.2 cm diameter γ-ray beam passes through the following elements: (a) "clean-up" collimator wall; (b) the D_2O sample located near the longitudinal center of the neutron counter; (c) machined lead attenuators located between lead collimator walls; (d) a NaI detector;(e) a HPGe detector.

Fig. 2.3).

After passing through the neutron-detector, the γ-rays passed through a flux-attenuation device (ϕAD), located between a third and fourth CC (each 2.54 cm diameter and 20.3 cm thick). The ϕAD contained five different lead attenuators of thicknesses ranging between 1.72 and 10.18 cm. Each attenuator could be placed on the beam axis via a remotely-controlled, six-position Geneva mechanism. Unattenuated beam was available under these conditions as well. The ϕAD allowed the user to attenuate the γ-rays by various factors ranging from ~2 to 100.

After passing through the ϕAD and CCs, the remaining γ-rays were incident on either the large NaI detector (*Molly*), or the high purity germanium (HPGe) detector, depending on whether flux or γ-ray energy was being measured. The purpose for attenuating the beam using the ϕAD was to keep flux on target at ~100 times the amount of flux on the face of *Molly*. Using this arrangement, online measurements of absolute γ-ray flux could be made with negligible pile-up effects. Also, data acquisition (DAQ) dead-times were assured to be small.

Absolute measurements the number of γ-rays on target, and the number of emitted neutrons from the reaction were needed to determine the total cross section for the ^{9}Be$(\gamma, n)^{8}$Be reaction. The next sections describe methods for absolute characterization of the neutron detector used in this experiment and the γ-ray detector *Molly*.

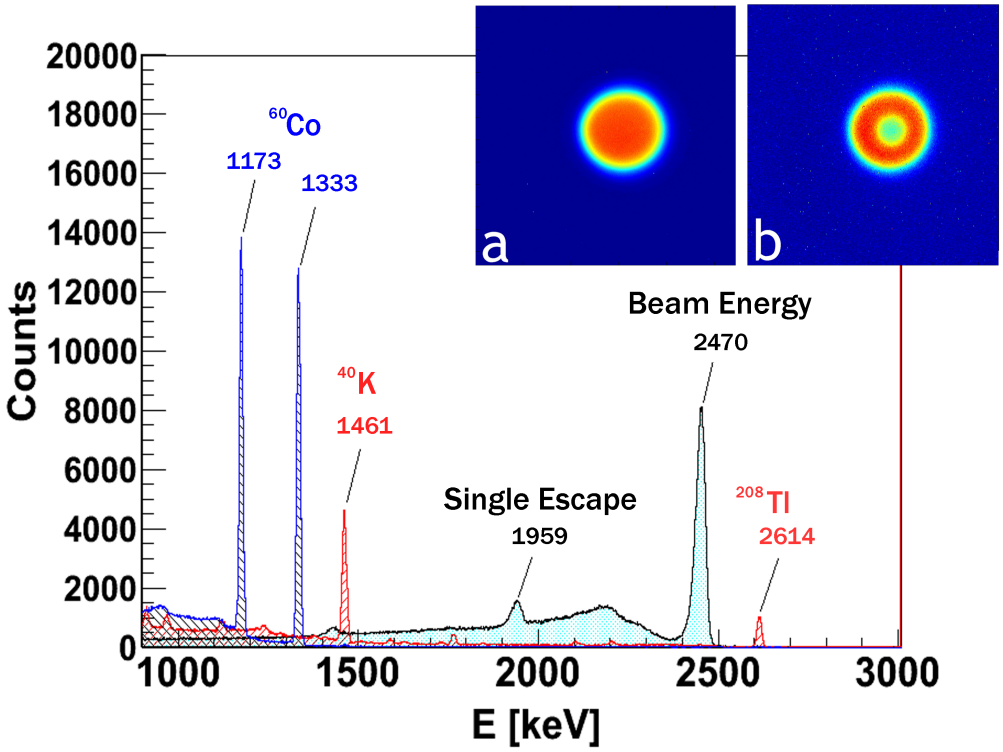

Figure 2.3: A HPGe spectrum for 2.470 MeV γ-ray beam with dE/E = 1%. Spectra of calibration γ-rays from ^{60}Co, ^{40}K, and ^{208}Tl are overlaid. Images showing confirmation of target alignment are inset.
(a) An unattenuated beam profile. Flux was nearly constant across the central portion and decreased rapidly at the edges.
(b) Contrast from a lead alignment pellet confirmed the placement of the target with respect to the beam.

2.3 Detectors

2.3.1 Neutron Counter

The neutron detector was a model IV inventory sample counter (INVS) developed at Los Alamos National Laboratory [SJ93]. This detector was designed for fast, non-destructive assay of radioactive materials. Specialized inserts for the axial bore of this counter were made to adapt it for use as the primary neutron detector for in-beam (γ,n) total cross-section measurements. Development and testing of this counter took place at TUNL using hadron beams in the tandem Van de Graaff accelerator laboratory and in the γ-ray beam at HIγS.

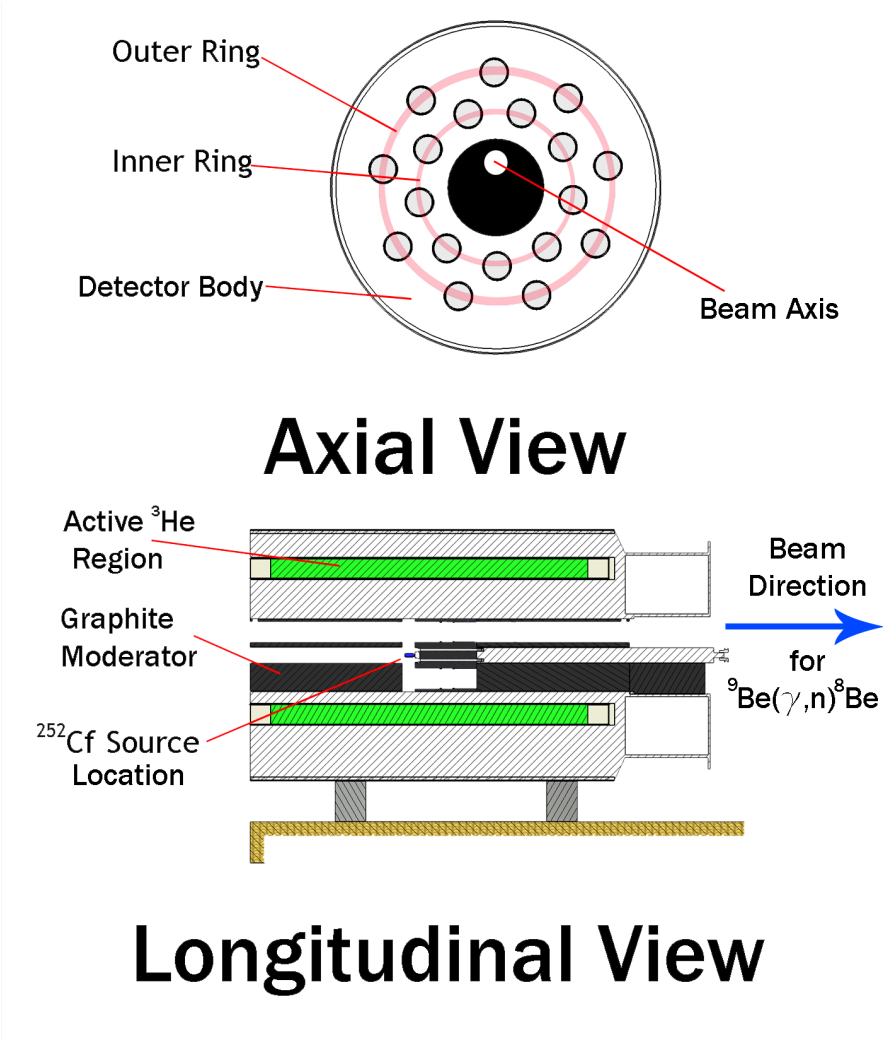

Figure 2.4: Two cross-sectional views of the neutron detector. The arrangement of inter-cavity moderator material corresponds to the experimental geometries used in the ^{252}Cf source and the $^2\mathrm{H}(\gamma, n)^1\mathrm{H}$ reaction experiments.

The active detection elements in the INVS counter are 18 tubular proportional counters,

each containing 6 atm of ^{3}He. The tubes are arranged in two concentric rings at radii 7.24 cm and 10.60 cm, each containing nine equally spaced detectors (see Fig. 2.4). The detectors are embedded in a cylindrical polyethylene body 46.2 cm long and 30.5 cm in diameter, which serves as a neutron moderator. The detector body has an 8.9 cm diameter axial cavity designed to contain the neutron source. For the rest of the thesis the term *longitudinal center* refers to the center of the detector with respect to the length of the detector body, and is distinguished from the term *axial center* which refers to the axis of the detector. Various views of the INVS are shown in Fig. 2.4.

Thermalization of the neutrons within the detector body increases the probability for initiating the ^{3}He$(n,p)^3$H reaction within the embedded tubes. An energy of 763.7 keV, shared between the outgoing proton and triton, is released in each reaction. Most of the kinetic energy is lost to ionization of ^{3}He, which is detected as an electrical pulse on the central electrode of each tube which is biased to +1780 V. A fixed threshold effectively discriminates against low-pulse-height signals generated by γ-rays and electronic noise. Signals above the threshold generate ~50 ns wide TTL pulses using on-board electronics. On-board signal-processing electronics within the detector produce three TTL logic output signals; the inner ring (I); the outer ring (O); and the logical OR of the I and O pulses (T). Whenever one or more tubes in the inner (outer) ring detect a neutron, a pulse is generated on the I (O) output. For neutrons with energies less than about 2 MeV, the I/O ratio can provide a coarse determination of the mean energy of the detected neutrons.

2.3.2 Scintillating Paddles

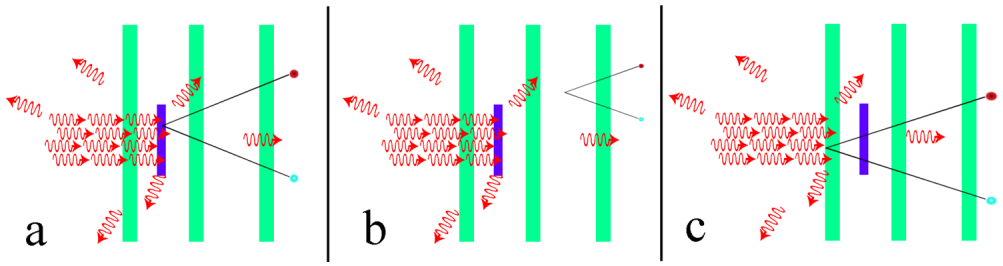

Figure 2.5: A schematic diagram of the scintillating paddles. (a) Pair-production from γ-rays on the lead foil are interpreted as a signal by coincidence and anti-coincidence logic. Pair-production at a location other than the foil as in (b) and (c) were vetoed by the circuit.

The relative incident γ-ray beam flux was continuously monitored using a system of three plastic scintillating paddles located upstream of the experimental setup. A coincidence / anti-coincidence circuit processed the signals from the photomultiplier tubes (PMTs) attached to the scintillators to reduce background. The circuit was designed to be sensitive to electron-positron pair production from a lead foil as shown in Fig. 2.5. The paddles were located at the end of the collimator hut, just before the entrance to the gamma vault.

2.3.3 Large NaI Crystal Detector (*Molly*)

The absolute γ-ray fluxes were determined by a cylindrical 25.4 cm × 35.6 cm NaI detector located behind the target on the γ-ray beam axis. The γ-ray beam flux incident on *Molly* was reduced by lead attenuators located immediately in front of the detector and downstream of the experimental setup. First, an attenuator was chosen, and measurements of attenuated flux were made. Subsequently, flux measurements were performed with the original attenuator removed, and a different attenuator, or no attenuator in the γ-ray beam. The paddles always measured unattenuated γ-ray flux, and thus provided a relative flux normalization. The attenuation from this arrangement was measured at several γ-ray energies.

A threshold setting on the NaI detector at approximately 550 keV reduces the expected ~100% total detection efficiency; therefore a total γ-ray detection efficiency of 98.3% was adopted in accordance with modeling using the Monte-Carlo neutral particle code MCNPX [MCN07]. A plot of *Molly*'s total efficiency and *Molly*'s efficiency for detection above a 550 keV threshold are displayed in Fig. 2.6.

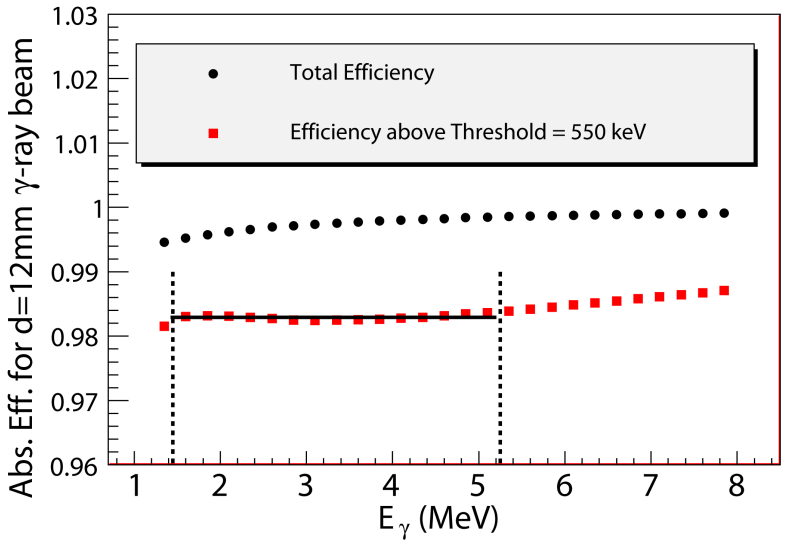

Figure 2.6: Plot of γ-ray detection efficiency of *Molly* for the total integration of the absorbed energy spectrum, and the efficiency integrated above 550 keV vs. γ-ray energy as determined by MCNPX simulations. Dashed lines mark the range of experimental γ-ray energies. The constant fit (solid line) over the experimental range gives the best value for the efficiency of γ-ray detection.

2.3.4 High Purity Germanium Detector

The energy resolution of the γ-ray beam was determined using a high purity Germanium (HPGe) detector placed on the γ-ray beam axis. For the energy range 1.5 MeV $\leq$ E_γ $\leq$ 5.2

MeV, the HPGe has resolution on the order of a few keV. A radioactive ^{60}Co source, and naturally present ^{40}K and ^{208}Tl provided energy calibration lines. The FWHM of the γ-ray beam as determined by the HPGe was typically between 1 and 3%. A typical γ-ray energy spectrum is shown in Fig 2.3.

3 Detector Characterizations

3.1 Introduction

For accurate cross section measurements, it was essential to determine the absolute energy-dependent detection efficiencies of the INVS counter and *Molly*, since they were the principal detectors used to determine the ^{9}Be$(\gamma, n)^{8}$Be reaction cross-section. In this chapter, I will describe the experimental and computational approaches used to characterize these two detectors.

3.2 Neutron Counter Tests

Four different sources, able to emit a known number of neutrons, were used to measure the efficiency of the INVS counter. Efficiency here is generally defined as

$$\epsilon \equiv \frac{N_{detected}}{N_{emitted}}. \tag{3.1}$$

First, a ^{252}Cf source, calibrated by the National Institute of Standards and Technology (NIST) generated a flux of neutrons known to ± 4.4% [Tho09]. Second, a coincidence experiment using the ^{2}H$(d, n)^{3}$He reaction provided a mono-energetic source of 2.26 MeV neutrons with the flux known to ± 10%, and gave insight into the thermalization time of neutrons in the INVS. Third, an investigation of the ^{7}Li$(p, n)^{7}$Be reaction produced <1 MeV neutron sources with fluxes known to ±6.6% [Gib59a]. Finally, the ^{2}H$(\gamma, n)^{1}$H reaction was used to produce tunable sources of monoenergetic neutrons ($0.1 \leq E_n \leq 1.0$ MeV) with fluxes known to ±3% accuracy [Sch05]. A comparison of all experimental data with Monte Carlo models demonstrates varying levels of agreement.

3.2.1 ^{252}Cf

Californium-252 is a standard calibration source for neutron detectors. The effective half life of ^{252}Cf is 2.645 years. Alpha particle emission and spontaneous fission produce a neutron yield of 2.314 × 10^6 neutrons/s/μg [Mar99]. The energy spectrum of neutrons from ^{252}Cf is well known [Smi57]. A calibrated ^{252}Cf source provides a single measurement of efficiency representing the response of the detector to a broad spectrum of neutron energies.

The ^{252}Cf source used consisted of 3.15 ng of active powdered material encapsulated within a small aluminum pellet. The source was suspended on the axis of the detector approximately 3.4 cm from longitudinal center. A graphite moderator filled most of the volume of the cavity to increase detection efficiency. A table of neutron activity versus date was provided by NIST [Tho09]. The experimentally determined efficiency for this configuration (shown in Fig. 2.4) was 40.5 ± 1.8 %. Using the definitions of I and O from Sect.2.3.1, the experimentally determined I/O ratio was 1.52 ± 0.01.

The dependence of the detection efficiency on the position of the source within the central cavity was determined by making measurements with the source placed at different positions within the central bore. Measurements on the central axis were made along the entire length of the detector. The detection efficiency has a maximum value at the longitudinal center and drops off smoothly as the source is moved in either direction away from the center along the detector axis. The shape of the position dependency is a purely geometric acceptance effect and can be approximated analytically for point sources with isotropic neutron emission. The measured detection efficiency as a function of the source position along the central axis of the counter is shown in Fig. 3.1 and is compared to simulated and calculated efficiencies.

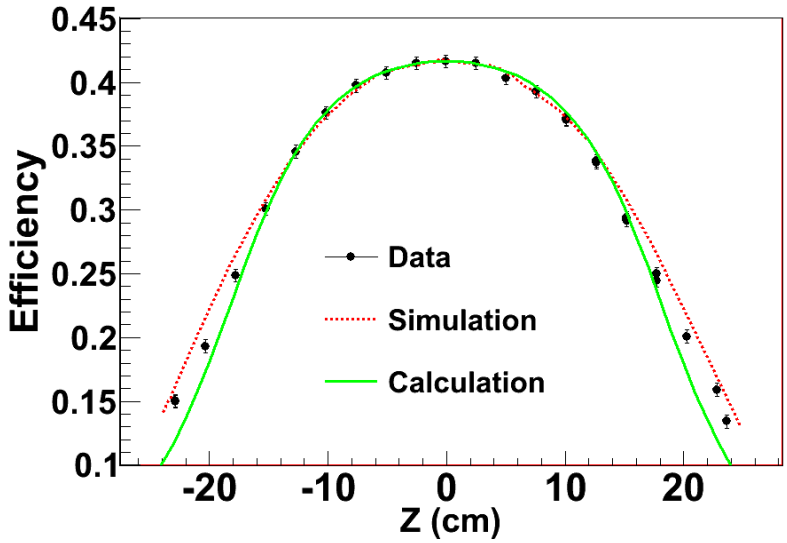

Figure 3.1: Efficiency vs. Z-axis position for a ^{252}Cf source in an open detector geometry.

The relative efficiency is directly proportional to the angular acceptance of the counter as a function of z, which is given by the equation below for an isotropic point source of neutrons.

$$\epsilon \propto d\Omega \approx \ 4\pi - 2\pi \left[\left(1 - \frac{L/2 - z}{\sqrt{(L/2 - z)^2 + r^2}} \right) + \left(1 - \frac{L/2 + z}{\sqrt{(L/2 + z)^2 + r^2}} \right) \right] \tag{3.2}$$

Here, r is the radius of the opening at the end of the detector, L is the active length of the ^{3}He gas, and z = 0 at L/2. This function is maximum when z = 0. For an open cavity geometry, the change in the efficiency over the length of an 8-cm long sample, centered on the axis at the longitudinal center, is approximately 1%. For a geometry like the one shown in Fig. 2.4 the changes in efficiency are negilgibly small over a length of nearly 20 cm centered on the logitudual center (see Fig. 3.1). For sources located off its central axis, the detection efficiency changes by less than 0.5% . The radial dependence of the efficiency is also mostly a geometric acceptance effect.

3.2.2 ^{2}H$(d,n)^3$He

The ^{2}H$(d,n)^3$He reaction was used to measure the efficiency for monoenergetic 2.26 MeV neutrons. The associated particle technique was used with the recoil ^{3}He nucleus detected in a silicon surface barrier detector inside an evacuated chamber. A schematic diagram of the experiment setup is shown in Fig. 3.2. The neutron counter was positioned so that its central axis coincided with the symmetry axis of the cone of neutrons associated with the ^{3}He particles detected in the silicon detector on the opposite side of the incident beam axis. The distance from the longitudinal center of the counter to the deuterium target was set so that the diameter of this neutron cone was smaller than the diameter of the central cavity through the detector. The energy of the incident deuteron beam and the detection angle of the silicon detector were set to produce 2.26-MeV neutrons emitted along the central axis of the counter. With this method the efficiency is computed as

$$\epsilon = \frac{N_n}{N_{^3He}} \tag{3.3}$$

where $N_{^3He}$ is the total number of detected ^{3}He-particles and N_n is the total number of neutrons detected in coincidence with the detected ^{3}He particles. The deuterium targets used in these measurements were ~ 100 μg/cm^2 thick deuterated polyethylene (C_2D_4) evaporated onto a 10 μg/cm^2 thick carbon foil. The deuteron beam energy incident on the foil was 2.0 MeV, and the average beam current on the C_2D_4 foil was ~20 nA. The cross-sectional profile of the deuteron beam at the foil was circular with a diameter of approximately 0.5 cm. Each of the two silicon detectors (one in-plane and one out-of-plane) had a solid angle acceptance d$\Omega = \pi/60$ sr, and each was located at a scattering angle of $\theta_{lab} = 26.50°$. Neutrons associated with detection of ^{3}He in the in-plane Si detector exited the target at $\theta_{lab} = 117.1°$

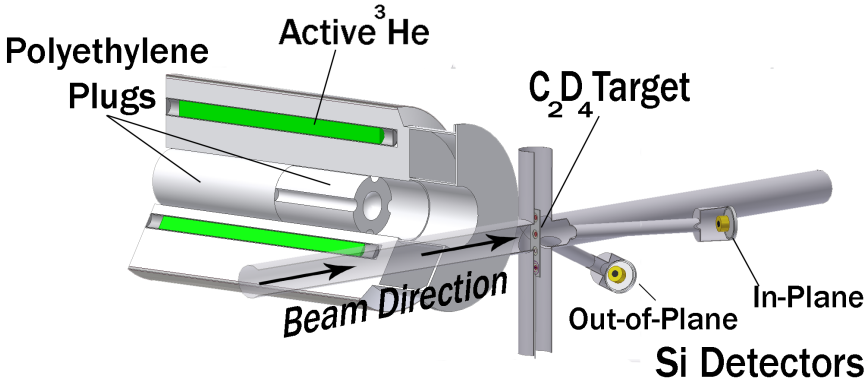

Figure 3.2: Schematic diagram of the experimental setup for the efficiency measurements made using the ^{2}H$(d,n)^3$He reaction at the tandem accelerator facility.

along the central axis of the neutron counter. The rear half of the central cavity was plugged with polyethylene to scatter neutrons traveling through the central cavity into the body of the counter. The out-of-plane Si detector was used to measure the rate of accidental coincidences.

Efficiency and thermalization time were deduced simultaneously using a time-to-amplitude converter (TAC), which recorded the time between a charged particle detection in the silicon detector and a neutron detection in the INVS. A threshold setting effectively discriminated against deuteron elastic scattering events. The effective TAC range was 22.5 μs. The TAC was calibrated using a pulser which was independent of the INVS that started and stopped the TAC with known delay. Because the INVS is a thermalization counter, detection efficiency is time-dependent on a microsecond time-scale. A peak in the TAC spectrum at ~3 μs suggests a source of delay exists caused by charge collection and signal processing in the INVS counter. This delay reduces the effective TAC range to 22.5 μs from 25.5 μs, which is where the experimental TAC spectrum ends. The present result for the neutron detection efficiency at E_n = 2.26 MeV, over a 22.5 μs range is 11.0 ± 1.1%. A histogram of an experimental TAC spectrum is shown in Fig. 3.3.

3.2.3 ^{7}Li$(p,n)^7$Be

The ^{7}Li$(p,n)^7$Be reaction was used to measure the energy-dependent detection efficiency over an energy range that overlaps with that covered by the ^{2}H(γ,n) source reaction below about 0.7 MeV and to provide data for a neutron source with the intensity distribution peaked at forward angles relative to the central detector axis [Bur74, Bur72]. The cross section for ^{7}Li$(p,n)^7$Be reaction is large and has been accurately measured [Gib59a] making it a good neutron source for calibrating the efficiency of detectors at low energies [Sek76].

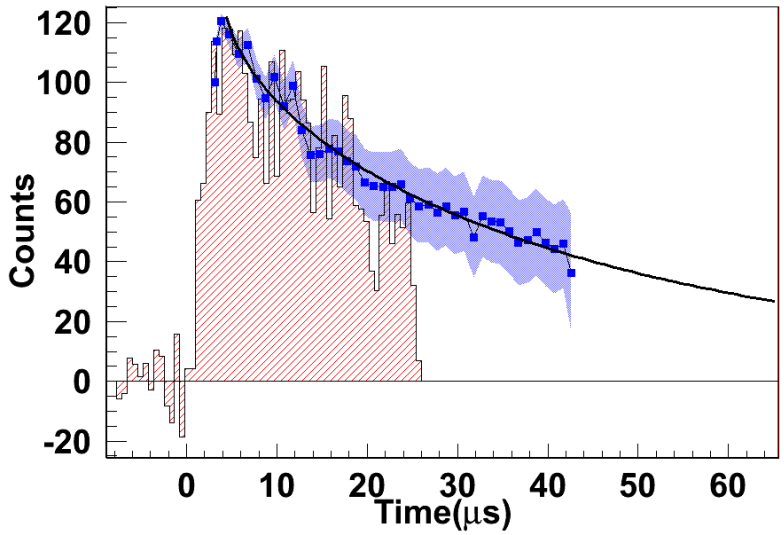

Figure 3.3: The histogram is a background subtracted TAC spectrum from the ^{2}H$(d,n)^3$He experiment. A simulated TAC spectrum (blue points with uncertainty band) is shown in comparison to the experimental histogram. The solid curve is a fit to the simulated spectrum. The fit (solid line) predicts that most neutron detection occurs outside the 22.5 μs experimental window.

Experimental Setup

The experimental arrangement is shown in Fig. 3.4. The proton beam was tuned through a double collimator set onto the LiF neutron production target. The cross-sectional profile of the beam on target was circular with a diameter of 5 mm, and the average beam current on target was 100 nA. The energies of the proton beams incident on the LiF target were between 1.88 and 2.46 MeV. The neutron production target was comprised of 39.8 μg/cm^2 of LiF evaporated onto a 8.3 μg/cm^2 thick carbon backing. (Details of target production are found in Sect. 7.1.) Targets were located on the axis of the INVS counter inside an evacuated beam pipe at 14.2 cm from the longitudinal center. The transmitted proton beam was collected in a voltage-suppressed Faraday cup at the end of the beam pipe. A polyethylene plug was placed just beyond the end of the beam pipe to increase detection efficiency. Backgrounds were measured by putting beam through both an empty target ring identical to the one that supported the LiF target, and a target ring that supported only a carbon backing. In total, beam-induced and environmental backgrounds amounted to $\leq 0.1\%$ of real counts.

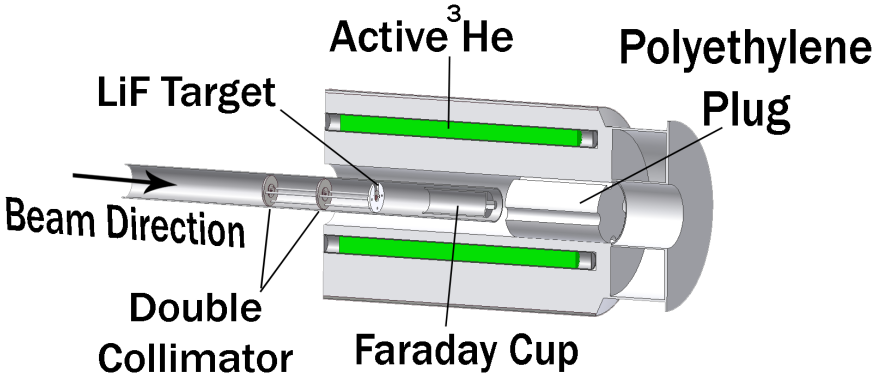

Figure 3.4: Schematic diagram of the experimental setup for the efficiency measurements made using the ^{7}Li$(p,n)^7$Be reaction at the tandem accelerator facility.

Results

The detection efficiency as a function of proton energy was calculated using

$$\epsilon(E_p) = \frac{N_n}{N_p N_t \sigma(E_p)} \tag{3.4}$$

where N_n is the total number of neutrons detected, N_p is the number of protons collected in the Faraday cup, N_t is the number of target nuclei per unit area, and $\sigma(E_p)$ is the total cross-section of the ^{7}Li$(p,n)^7$Be reaction at proton energy E_p.

The data (see Fig. 3.5) display a relative minimum in efficiency near $E_p = 2.13$ MeV followed by a relative maximum near $E_p = 2.32$ MeV. These shifts in efficiency coincide with rapid changes in the angular distribution of neutrons [Bur72, Bur74]. Though statistical uncertainties were very small, systematic uncertainties for target thickness and cross-section contributed 3.5% and 5%, respectively, resulting in an overall systematic uncertainty of 6.6%.

3.2.4 ^{2}H$(\gamma,n)^1$H

The ^{2}H$(\gamma,n)^1$H measurement was unique among the experiments described here in that it produced nearly monoenergetic neutrons with very small flux uncertainties. Several efficiency measurements were made that highlighted the energy-dependent response of the detector. Because the ^{9}Be$(\gamma,n)^8$Be was performed in the exact same manner as ^{2}H$(\gamma,n)^1$H, the efficiency determination here is the one used for interpreting the ^{9}Be$(\gamma,n)^8$Be data.

Experimental Setup

The target consisted of approximately 3.2 g of 99.8% enriched D_2O sealed inside a thin-walled polyethylene tube that was 7.62 cm long. The target was located at longitudinal center,

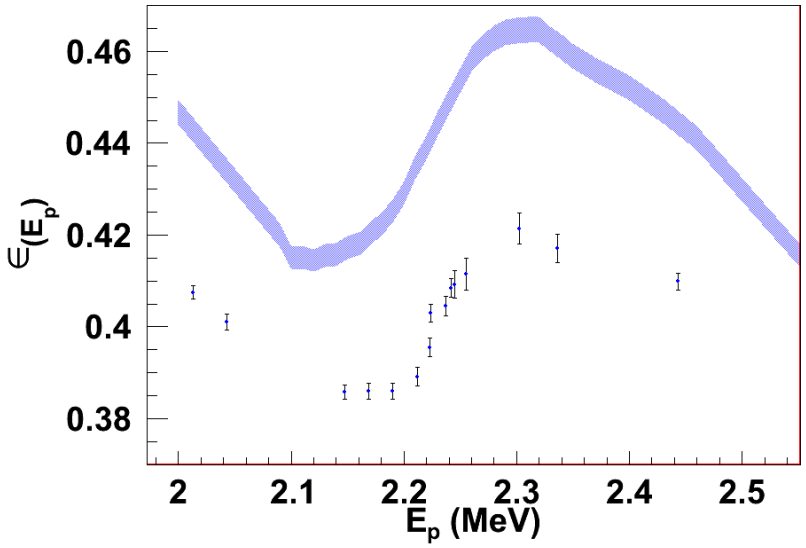

Figure 3.5: For the ^{7}Li$(p,n)^7$Be reaction, a comparison of $\epsilon(E_p)$ as determined by experiment (points) and by simulation (band). MCNPX simulations reproduce the shape of the efficiency curve well. See discussion in Sect. 3.3.1.

but 2.9 cm above axial center, and occupied one of the four 2.54 cm diameter azimuthal holes in the rotatable graphite cylinder described previously.

Background

Two sources of neutron backgrounds existed in this experiment. Environmental backgrounds caused by cosmic-ray neutron production and other neutron sources in the setup area were typically 0.2 n/s per ^{3}He tube for a total of 3.6 n/s. The second source of background in the neutron detector arose from γ-ray-beam-induced counts. Gamma-rays that scatter from the target can deposit enough energy to register a signal above the threshold. This type of background was measured by bombarding a graphite target with the γ-ray beam. Beam-induced backgrounds, which were explicitly taken into account, amounted to approximately 2.5 counts/10^6 γ-rays on target, which was typically $\leq 1\%$ of real counts.

Results

Detection efficiency for neutrons from γ-rays on a heavy water sample can be explicitly calculated from

$$\epsilon_n(E_\gamma) = \frac{N_n \chi(E_\gamma) \epsilon_\gamma}{f N_\gamma N_t \sigma(E_\gamma)}, \tag{3.5}$$

where N_n is the number of neutrons detected, $\chi(E_\gamma)$ is the measured, energy-dependent attenuation by lead, ϵ_γ is the efficiency of γ-ray detection, N_γ is the number of γ-rays detected,

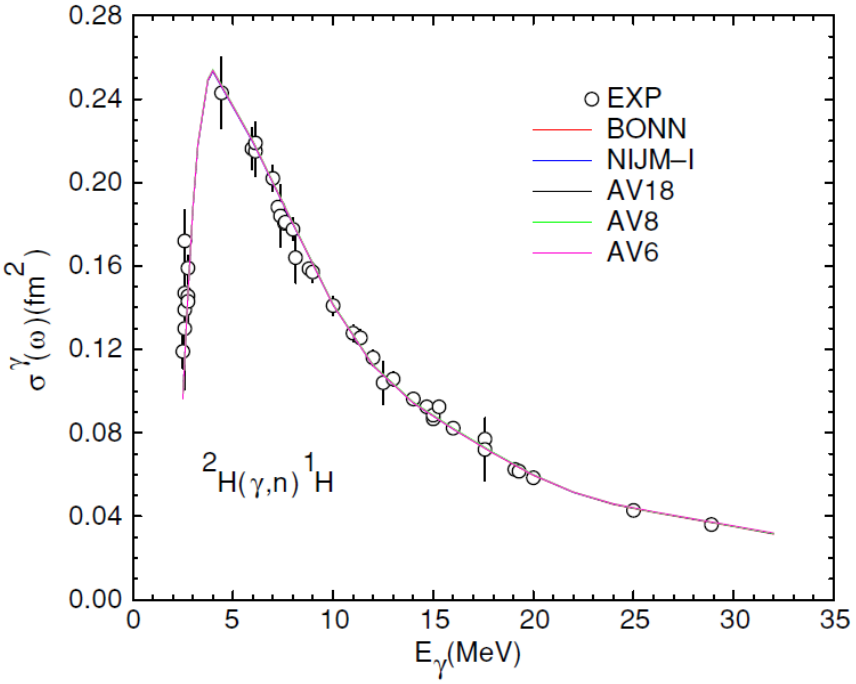

Figure 3.6: The well known $^2\mathrm{H}(\gamma, n)^1\mathrm{H}$ cross-section. Different NN-model calculations are indistinguishable. Image from Ref. [Sch05].

N_t is the number of target nuclei per cm^2 and $\sigma(E_\gamma)$ is the total cross section of the $^2\mathrm{H}(\gamma, n)^1\mathrm{H}$ reaction at E_γ [Sch05]. The author of Ref. [Sch05] calculated the $^2\mathrm{H}(\gamma, n)$ total cross sections with several widely-used N-N potential models, all of which were indistinguishable to within 1%, irrespective of the model used. In addition, this cross section agrees with the world data which report uncertainties between 3 and 6% [Bir85, Mor89, DG92, Har03].

It will be shown in detail in Sect. 4.6 that a thick target correction factor,

$$f = \frac{1 - e^{-\mu_w t}}{\mu_w t}, \tag{3.6}$$

is required to account for the effects of the loss of γ-rays from all interactions within the target. Here, I used NIST attenuation coefficients for water μ_w [Hub89] and the mass thickness t of the target. The γ-ray energy, E_γ, and neutron energy, E_n, are related by

$$E_n = \frac{E_\gamma - 2.225}{2.001} \tag{3.7}$$

where -2.225 is the Q-value for the reaction in MeV, and the factor of 2.001 comes from energy sharing between the outgoing proton and neutron.

A small amount of neutron contamination was observed in the data above 4.143 MeV corresponding to the $^{17}\mathrm{O}(\gamma, n)$ reaction. Therefore, only values for the $^2\mathrm{H}(\gamma, n)^1\mathrm{H}$ cross

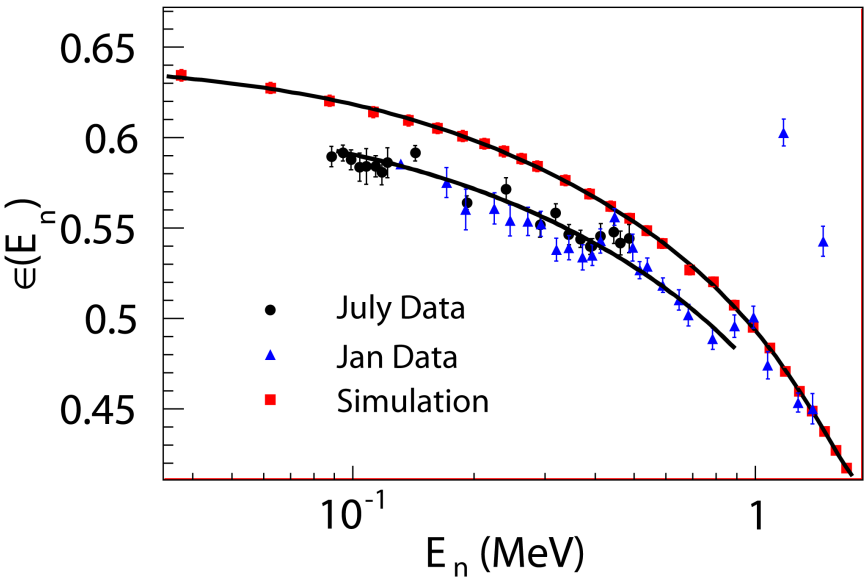

Figure 3.7: Black circles and blue triangles are experimentally determined neutron detection efficiencies using the cross-section from Ref. [Sch05]. Red squares are simulations. Fits to simulation are normalized to data between 2.48 MeV $\leq E_\gamma \leq$ 4.143 MeV corresponding to ~0.1 MeV $\leq E_n \leq$ ~0.9 MeV. The normalization amounts to 4%.

section corresponding to energies of 2.48 MeV $\leq E_\gamma \leq$ 4.143 MeV were used to determine detector efficiency.

3.3 Monte Carlo Simulations

The Monte-Carlo code MCNPX [MCN07] was used to simulate all particle interactions. For all simulations, material densities for the INVS were fixed, and standard cross section libraries [Cha06] were used. Variable parameters in each simulation were:

1. the arrangement of materials inside the cavity;

2. the location of the neutron emitting source;

3. the energy and spatial distribution of neutrons.

Absolute detection efficiencies were extracted from simulations for comparison with each experiment.

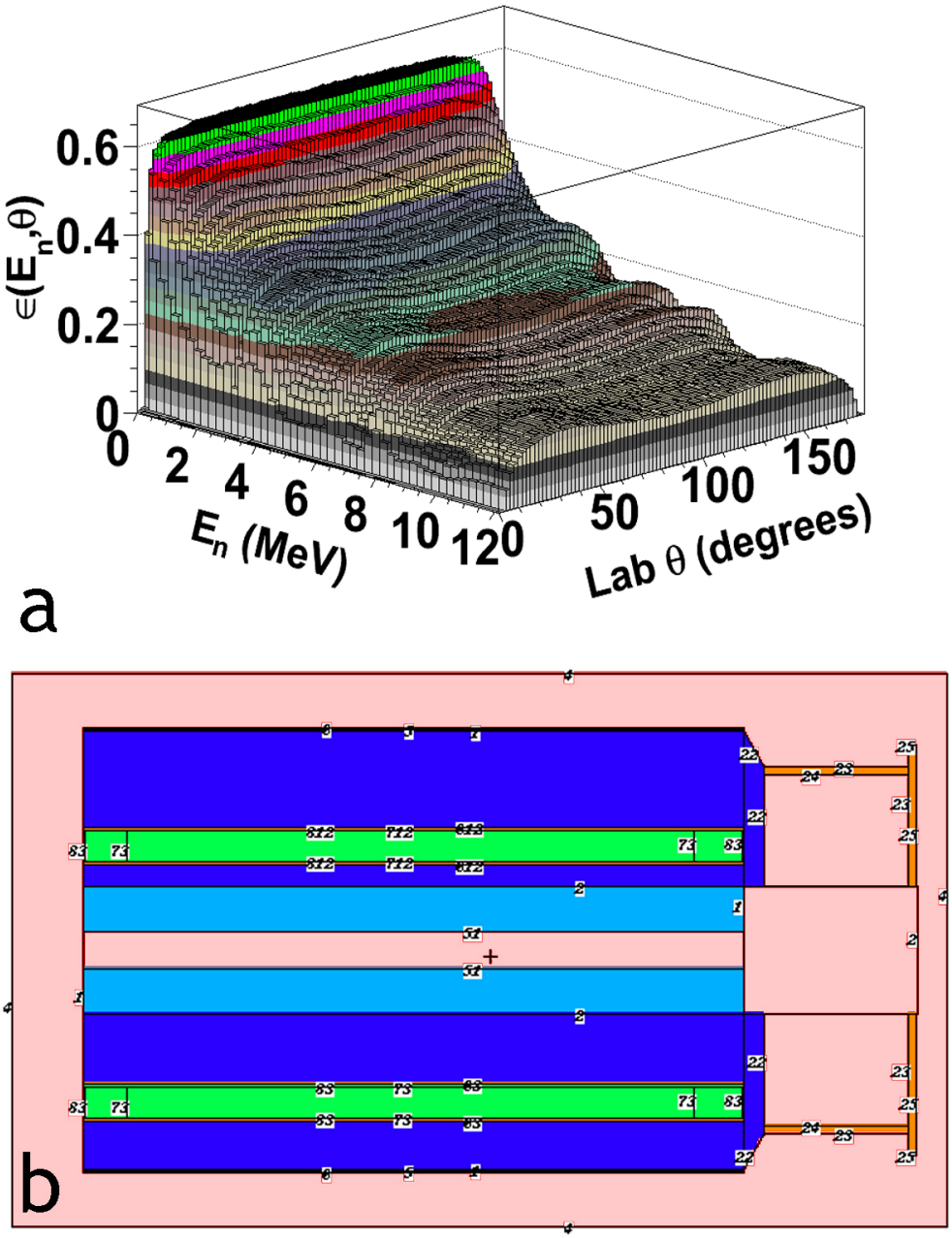

Figure 3.8: (a) 3-dimensional plot of efficiency vs. E_n and angle for the geometry shown in (b), which is a likely arrangement of graphite moderator within the INVS for use in (γ, n) experiments at HIγS. The target was placed at the center of the detector.
(b) A 2-dimensional slice through the center of the simulated geometry. The cavity was filled with graphite except for a 2.54 cm diameter hole for the γ-ray beam.

3.3.1 MCNPX

^{252}Cf

Efficiency measurements of ^{252}Cf were made during the course of the ^{2}H$(\gamma,n)^{1}$H experiment. Consequently, the arrangement of materials inside the INVS cavity was identical for both experiments. The energy distribution of neutrons produced by fissioning ^{252}Cf was modeled as a Watt-fission spectrum which has the form

$$p(E) = Cexp^{(-E/a)}sinh(bE)^{1/2}, \tag{3.8}$$

where a and b are parameters given for ^{252}Cf [MCN07]. The MCNPX-simulated efficiency of 40.5% agrees with the experimentaly determined efficiency of 41.4 ± 1.7 %. The simulated I/O ratio of 1.59 falls short of agreement with the experimentally determined 1.51 ± 0.01 because of a 6% larger efficiency for measurement in the outer ring (see Fig. 3.13). This reason for this discrepancy is not known.

^{2}H$(d,n)^{3}$He

For the ^{2}H$(d,n)^{3}$He reaction, a simulated beam of 2.26 MeV neutrons emitted from inside an evacuated volume, through an aluminum beam-pipe wall, and was directed toward the axial center of a set of polyethylene plugs that filled most of the detector cavity (see Fig. 3.2). Since the efficiency depends on the chosen coincidence timing-window, a time dependent model for the ^{2}H$(d,n)^{3}$He reaction was created to compare with experiment. In this model, only neutrons detected before a user-defined time counted toward efficiency. A plot of efficiency vs. time was simulated for times between t = 0 and t= 1000 μs (see Fig. 3.9). To produce a simulated TAC spectrum, a plot of the slope of ϵ(t) vs. time was generated for comparison with data (see Fig. 3.3).

The simulated total efficiency for neutrons collected between 0 and 22.5 μs is 11.9% in agreement with experiment. This is an 8% reduction from the total efficiency expected (13.0%) for neutrons collected between 0 and 25.5 μs- the full experimental range. This difference results from a relatively large slope in detection efficiency vs. time for early times. It is noteworthy that simulations predict a relatively long time (nearly 500 μs) before a maximum efficiency of 38.8% detection is realized for 2.26 MeV neutrons from the ^{2}H$(d,n)^{3}$He reaction.

^{7}Li$(p,n)^{7}$Be and ^{2}H$(\gamma,n)^{1}$H

Simulations for the ^{7}Li$(p,n)^{7}$Be and ^{2}H$(\gamma,n)^{1}$H reactions were carried out in the following way. First, the location of the source was set to match experimental conditions. For a single simulation the source emitted monoenergetic neutrons only between angles θ and $\theta + d\theta$ with

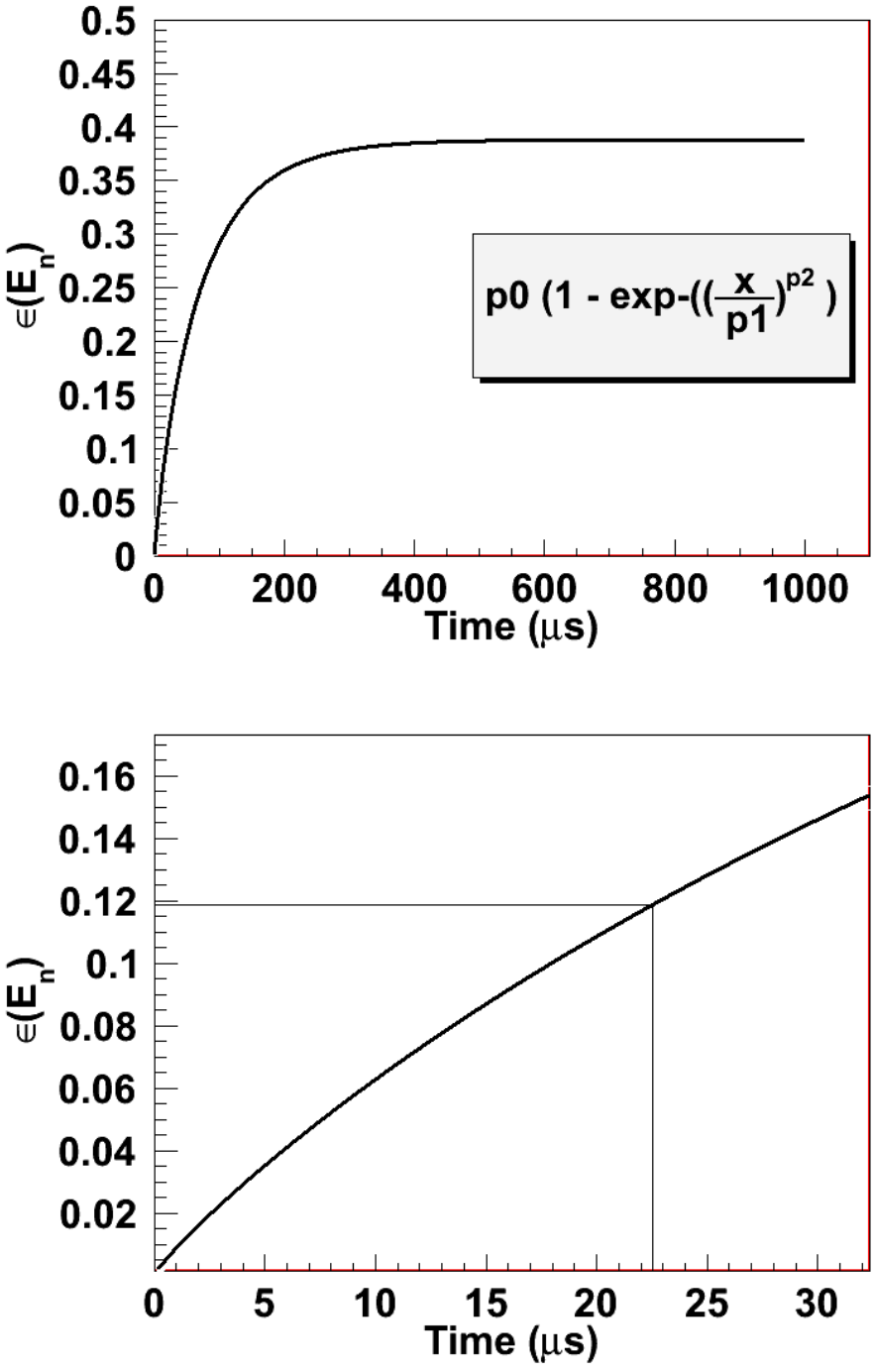

Figure 3.9: (Top) A three parameter fit (solid line) describes the simulated efficiency of neutron detection as a function of time in the ^{2}H$(d,n)^3$He experiment very well. (Bottom) The same plot expanded to show t < 35 μs. The vertical and horizontal lines identify the experimental window and expected efficiency.

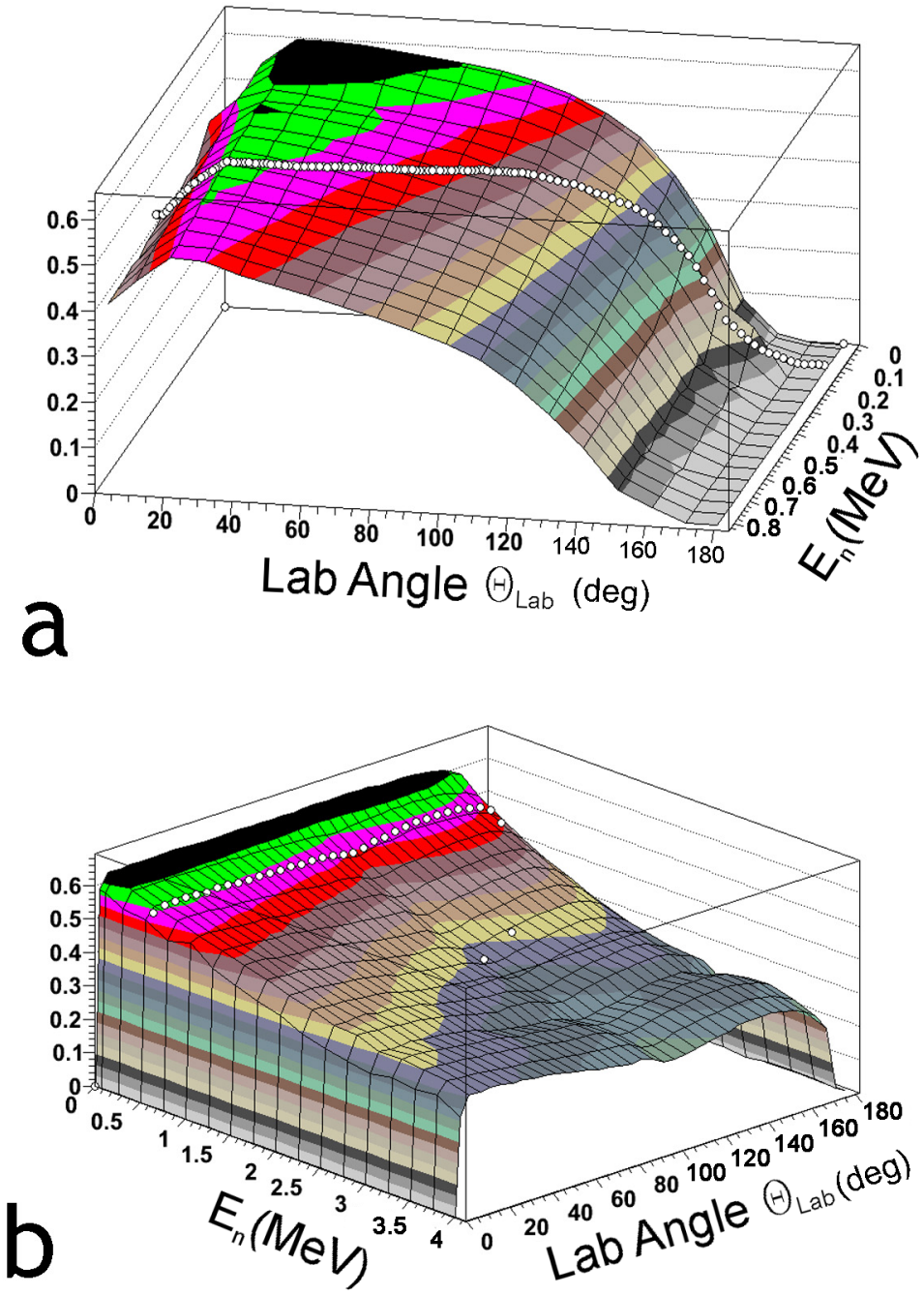

Figure 3.10: (a) 3-dimensional plot of efficiency vs. E_n and angle for the ^{7}Li$(p,n)^7$Be geometry. (b) 3-dimensional plot of efficiency vs. E_n and angle for the ^{2}H$(\gamma,n)^1$H geometry. The white dots in each plot correspond to efficiencies sampled by combining kinematics and angular distribution data ([Bur72, Bur74]) for 2.2 MeV protons incident on ^{7}Li in (a) and 3.2 MeV γ-rays incident on ^{2}H in (b).

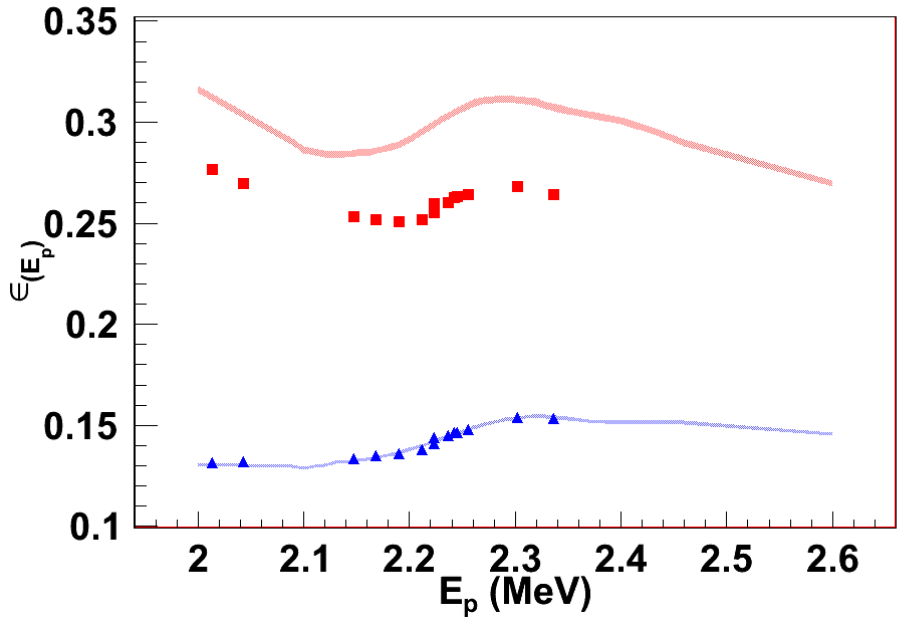

Figure 3.11: Absolute efficiency for the inner ring (squares) and outer ring (triangles) of the detector during the ^{7}Li$(p,n)^7$Be experiment. MCNPX models with uncertainty are shown as colored bands.

constant emission over ϕ. After stepping through all of θ space, the process was repeated for a new neutron energy.

Ultimately, a 3-dimensional plot was constructed with neutron energy on the x-axis, emission angle on the y-axis and detection efficiency on the z-axis. After choosing an incident particle energy, and inputing expected angular distributions for the neutrons in the center-of-mass (COM) frame [Bur72, Bur74], a second Monte Carlo process produced an average efficiency for the given source conditions. This process was repeated for several incident particle energies, and the result was a plot of simulated efficiency as a function of incident particle energy.

The efficiency map generated for the ^{7}Li$(p,n)^7$Be geometry (see Fig. 3.10) yields higher efficiencies for neutrons emitted at forward angles. This resulted from an asymmetric placement of moderator (see Fig. 3.4). The efficiency map generated for the ^{2}H$(\gamma,n)^1$H configuration (see Fig. 3.10) is much more symmetric about 90°. The shortest path for a neutron to escape the detector is at 90°, resulting in a relative minimum across lines of constant neutron energy.

For the ^{7}Li$(p,n)^7$Be reaction, simulations reproduce very well the shapes of $\epsilon(E_p)$ for both the inner and outer detector rings (see Fig. 3.11). Absolute detection efficiency for the outer ring of detectors is in good agreement with experiment. A 13% systematic offset in absolute efficiency is observed for the inner ring of detectors. The systematic effects discussed in

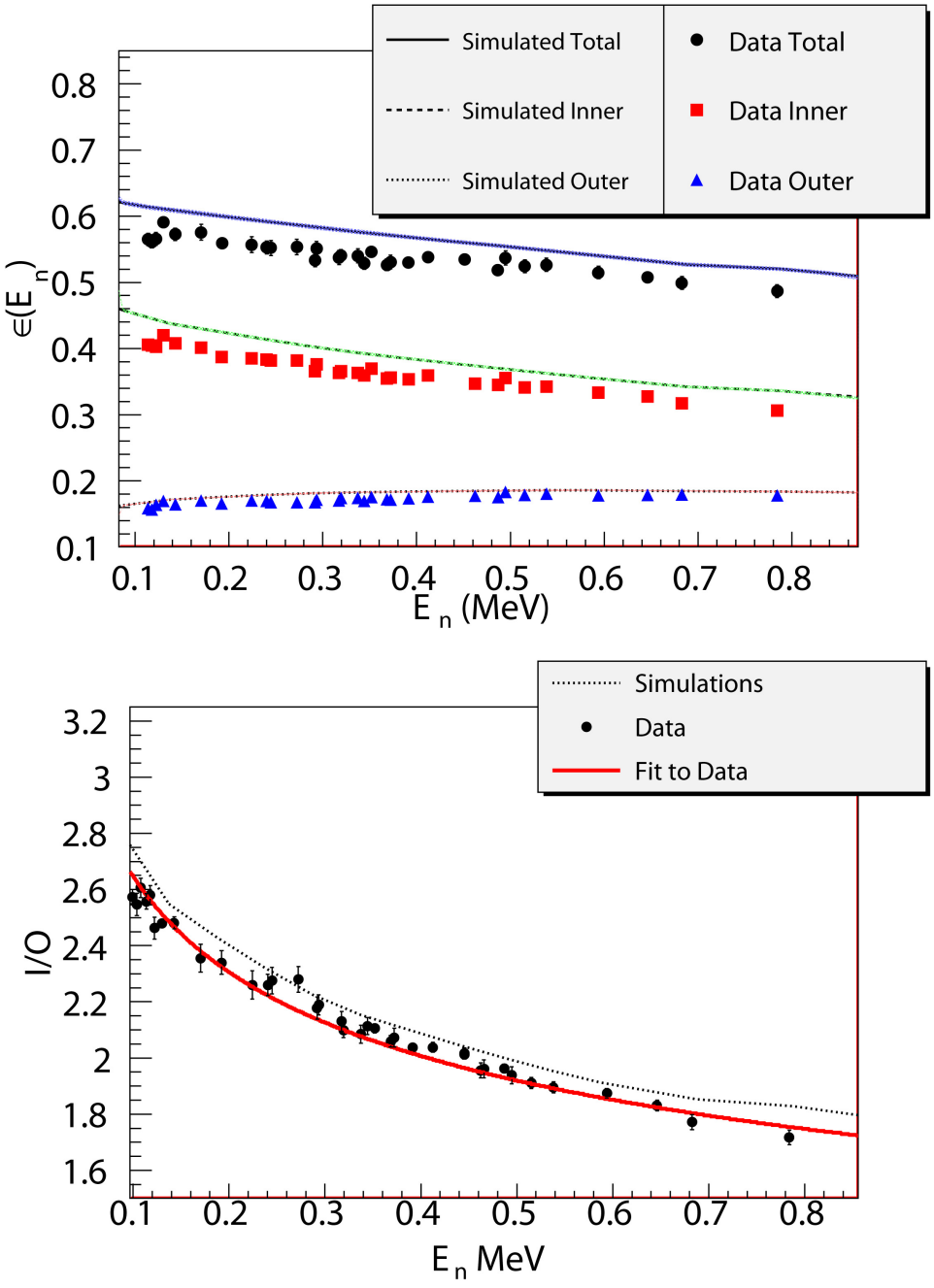

Figure 3.12: Simulations and data with statistical error bars are shown. The efficiency (a) and I/O ratio (b) for neutrons detected by the INVS depend strongly on the neutron energy. Colored bands indicate the expected uncertainty for simulations [MCN07].

Sect. 3.2.3 can account for a maximum difference of 6.6%. The difficulty with this discrepancy is that it appears to be of a systematic nature, while only affecting the inner ring of the INVS counter. A missing thermal neutron sink in the model may explain part of the difference. An underestimated amount of aluminum in the modeled beam pipe could have inadequately converted neutrons to γ-rays, leaving an excess of thermal neutrons in the region of the inner ring of the INVS counter.

For the ^{2}H$(\gamma, n)^1$H experiment plots of $\epsilon(\mathrm{E}_n)$ for the inner ring, the outer ring, and the total show the data trends in good agreement with trends predicted by the simulation. The data for total detection efficiency are systematically lower than simulation by 4% (see Fig. 3.12). Data for the inner and outer rings were systematically lower by 6.7% and 3.7% respectively. These data provide a benchmark calibration for this INVS counter with regards to its use in future (γ, n) experiments.

In the INVS counter a single detected neutron provides no information about the energy of the neutron. However, the average neutron energy from an ensemble of detected neutrons may be gleaned from the observed proportionality

$$I/O \propto E_n^{-\frac{1}{5}}, \tag{3.9}$$

which is easily inverted. The ability to distinguish the signature I/O ratio for E_n from the I/O ratio for E_n+ $\Delta\mathrm{E}_n$ becomes more difficult as E_n increases (see Fig. 3.12).

This method for evaluating detector efficiency is valid irrespective of the target used. A deuteron target was chosen because of the precision with which its (γ, n) cross section is known. Evaluating the efficiency this way establishes the energy-dependent response of the detector for future users under certain conditions. As long as (a) the target location is fixed; (b) the average neutron energy is known; and (c) the COM angular distributions are known, then the efficiencies determined here are valid for any (γ, n) reaction that satisfies the conditions above. If backgrounds are low, and the neutron energies are < 2.0 MeV, condition (b) may be relaxed, because the neutron energy information may be obtained from the I/O ratio. For neutron energies < 500 keV, condition (c) may also be relaxed because the response of the detector is nearly constant with respect to angle of emission.

3.3.2 Characterization Results

Figure 3.13 shows the ratio of experimentally determined efficiency to simulated efficiency vs. average neutron energy for each experiment. Ratios have been determined for the inner (I) and outer (O) rings separately, as well as for the total (T).

Neutrons from the ^{2}H$(\gamma, n)^1$H reaction were emitted from within ± 4 cm from the longitudinal center of the detector with a $\sin^2(\theta)$ distribution in the CoM frame which is hardly changed when converted to the lab frame because of the relatively small momentum of the

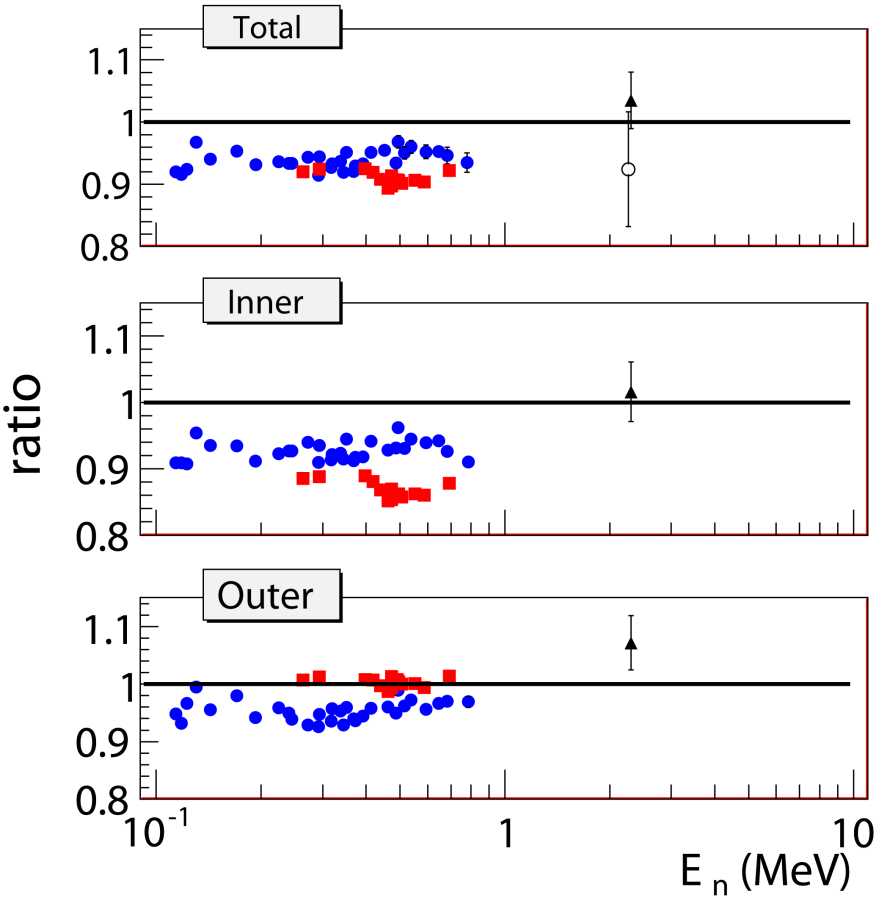

Figure 3.13: Plot of the ratio of data to simulation for all experiments. Results for Total ϵ_n, Inner Ring ϵ_n, and Outer Ring ϵ_n are shown. Filled circles are ^{2}H$(\gamma, n)^1$H data; Squares are ^{7}Li$(p, n)^7$Be data; Triangles are ^{252}Cf data; Open circles are ^{2}H$(d, n)^3$He data.

incident γ-ray. The arrangement of moderating materials was approximately symmetric. Under these conditions, simulations reproduce measurements to within a normalization of -6.7% (I), -3.7% (O), and -5.9% (T). These differences are likely the result of effective threshold settings on the signals from the detector tubes. This feature of the effective threshold settings was not included in the simulations.

Neutrons from the ^{7}Li$(p,n)^{7}$Be reaction were emitted far from the longitudinal center of the detector with a Legendre polynomial series distribution in the CoM frame which is significantly changed when converted to the lab frame because of the relatively large momentum of the incident proton. The arrangement of moderating materials was asymmetric - biased to achieve higher detection efficiency for neutrons emitted near θ_{lab} close to zero. Under these conditions, absolute detection in O is reproduced very well by simulations; however, absolute detection in I is systematically 13% smaller than predicted by simulations, resulting in a nearly 10% systematic difference in T.

The difference in the level of agreement between simulations and experiment for I and O for the ^{7}Li$(p,n)^{7}$Be reaction is intriguing. The most likely explanation is that the amount of aluminum in the intervening beam pipe was underestimated in the simulations which caused an excess of thermal neutrons in the vicinity of I.

The systematic differences between experiment and simulation for I, O and T for the ^{2}H$(\gamma,n)^{1}$H measurement confirmed the need for a well known, tunable, monoenergetic neutron source. Reliance on simulations alone would have introduced systematic errors in future (γ,n) measurements on the order of 6%. Using the cross-section of Ref. [Sch05] as a 1% standard provided tunable monoenergetic neutron sources with fluxes known to ± 3%. The method for simulating absolute detection efficiencies for the ^{2}H$(\gamma,n)^{1}$H reaction was not significantly influenced by the choice of target material. The same technique was used for the ^{9}Be$(\gamma,n)^{8}$Be cross sections ensuring a high degree of accuracy.

3.4 Large NaI Crystal Detector (*Molly*)

For collimated γ-rays of energy 1.5 MeV $\leq$ E$_\gamma$ $\leq$ 5.2 MeV incident on the face of *Molly*, calculations predict that almost 100% of the γ-rays will deposit energy inside the crystal. Simulations predict the same result. An associated particle experiment using the ^{19}F$(p,\alpha\gamma)$ reaction was performed to verify this prediction.

3.4.1 ^{19}F$(p,\alpha\gamma)$

The 340 keV resonance of the ^{19}F$(p,\alpha\gamma)$ reaction was accessed using the Mini-Tandem accelerator at TUNL. Gamma-rays emitted from this reaction are known to have an isotropic distribution [Hel72, Cro91]. Lead shielding was employed to collimate the emitted γ-rays into a 2.54 cm diameter distribution centered on the face of TUNL's large NaI detector known as

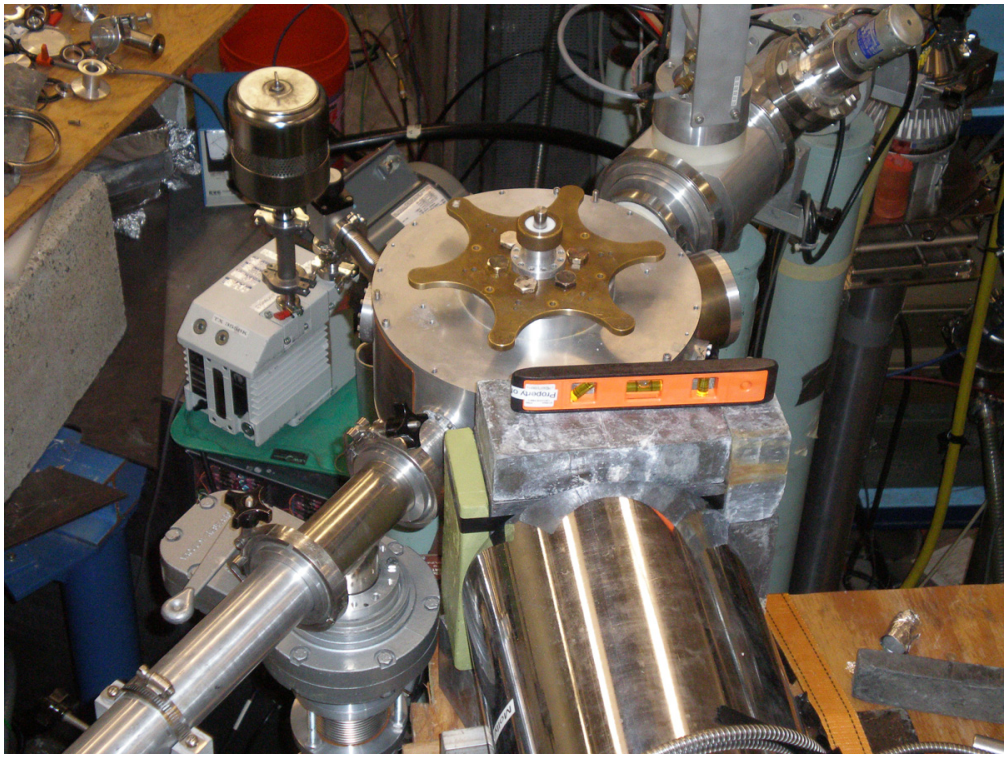

Figure 3.14: Photograph of the experimental setup. *Molly* (bottom) sits behind a collimating wall of lead. Additional lead shielding was placed inside the scattering chamber (center).

Molly. The total efficiency of *Molly* is consistent with ~100% for a beam of 6.130 MeV γ-rays. Any loss of efficiency from threshold settings may be accurately discerned from modeling in GEANT 4.

For many experiments performed at TUNL's HIγS facility, an absolute measure of the efficiency of the large NaI crystal detector known as *Molly* is needed to understand the limits of precision for experiments requiring knowledge of the incident γ-ray flux. Models predict that *Molly* has a total-efficiency of ~100% for γ-ray beams incident on its face with energies between 1.5 MeV to 7 MeV. This total efficiency may be affected by electronic threshold settings, light collection efficiency, and variables for which ascribing uncertainties may be difficult. The ^{19}F(p,$\alpha\gamma$) reaction was chosen to measure *Molly*'s absolute γ-ray efficiency experimentally because it provides a monoenergetic γ-ray source with an associated α-particle. The ^{19}F(p,α) reaction creates an excited state of ^{20}Ne, which then decays to one of four available excited states or the ground state of ^{16}O. Of the four excited states, three may decay to the ground state of ^{16}O via γ-ray emission. The three γ-ray-associated α-particles will have different energies corresponding to the different excited states in ^{16}O* to which the ^{20}Ne* decayed. Fig. 3.16 shows a typical silicon detector spectrum with clear definition of three α-particle peaks corresponding to the three lowest lying excited states in ^{16}O*. The resonance for 340

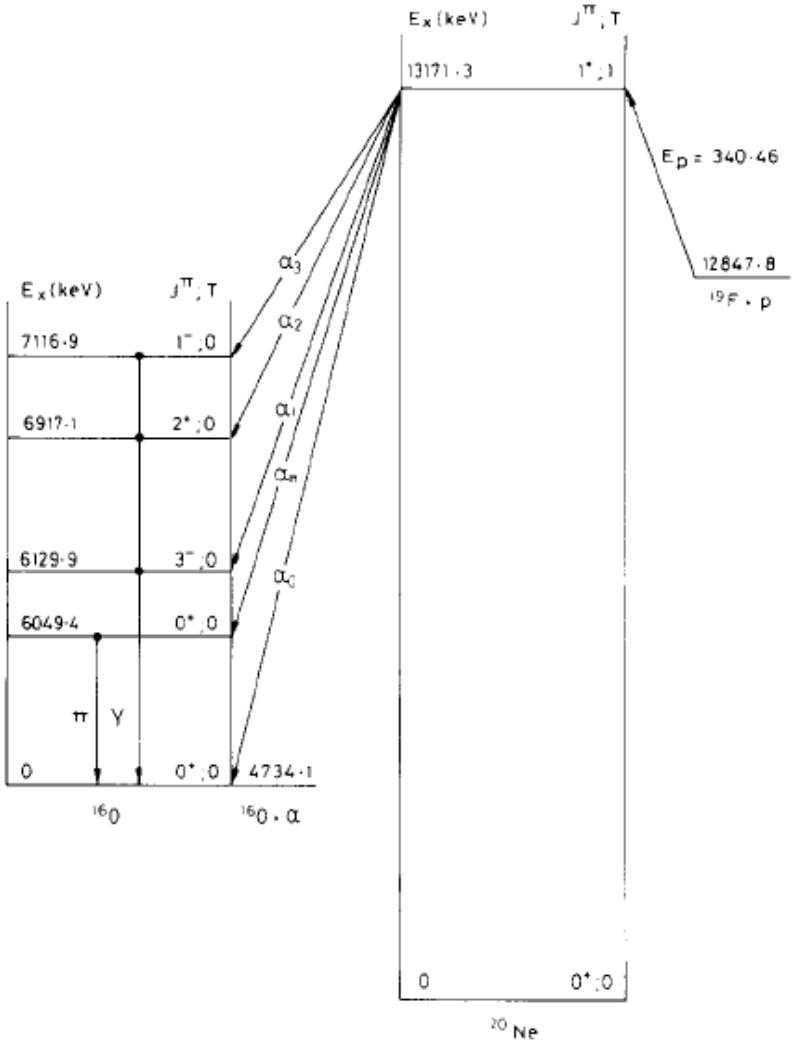

Figure 3.15: Level scheme for the decay of ^{20}Ne to ^{16}O. Image from Ref. [Cro91].

keV incident protons favors the 3^- state of $^{16}O^*$ which decays by emission of a 6.13 MeV γ-ray. These γ-rays are emitted isotropically [Hel72, Cro91]. To produce beam-like conditions, over 20 cm of lead shielding was arranged to collimate γ-rays down to a 2.54 cm diameter circle centered on the front face of *Molly*. The solid angle opening defined by this lead shielding determines the fraction of α-particle-associated γ-rays incident on the face of *Molly*.

Fig. 3.14 shows the experimental setup. A small scattering chamber designed with very thin windows was set on the beam line following TUNL's Mini-Tandem accelerator. Six silicon detectors were placed at backward angles to detect outgoing α-particles. Incident protons of $\geq$ 340 keV were collimated by a double slit located 6.35 cm away from the target. Targets were thin films of LiF, approximately 50 μg/cm^2 in thickness evaporated onto ~10 μg/cm^2 carbon backings.

The presence of a peak in a TAC spectrum confirmed α-γ coincidences. Software gates isolated events that were both in the resonant α-peak of each silicon detector and in the peak of the TAC spectrum, and generated a spectrum of coincident events in the NaI detector (Fig. 3.16). Coincident counts that fell within the full energy peak were ideal for the present analysis for two reasons. First, natural backgrounds at 6.13 MeV were low. Second, confusion between γ-rays that scattered before entering the detector, and those that Compton scatter within the detector is eliminated by choosing only γ-rays in the full energy peak.

The measured peak efficiency of *Molly* is

$$\epsilon_{peak} = \frac{N_\gamma^{peak}}{\frac{d\sigma}{d\Omega} \times N_\alpha} \tag{3.10}$$

where N_γ^{peak} is the number of detected γ-rays in the full energy peak, $d\Omega/4\pi$ is the fractional solid angle defined by the lead shielding, and N_α is the number of α-particles detected for the resonant reaction.

Over 6000 total α-γ coincidences resulted from 1.3×10^7 total α-particles counted over the course of 50 hours of data collection. The fractional solid angle defined by the lead shielding was calculated from the geometry to be $(4.87\pm0.12)\times10^{-4}$. Precision was limited by uncertainties in measurements of the distance between the target and the end of the collimator, and of the diameter of the collimator. Simulations of the solid angle were performed using the Monte Carlo code MCNPX to account for the effects of finite beam size and known geometrical constraints in the experiment. A corrected fractional solid angle of $(4.91\pm0.12)\times10^{-4}$ was adopted yielding a peak efficiency of 69.5 ± 1.9%. This peak efficiency is consistent with GEANT 4 models of *Molly* which predict a peak efficiency of 69.7% and a coresponding total efficiency of 98.9% for an incident beam of 6.13 MeV γ-rays. From these results I infer that experiment-dependent losses of efficiency caused by electronic threshold settings can be modeled very accurately.

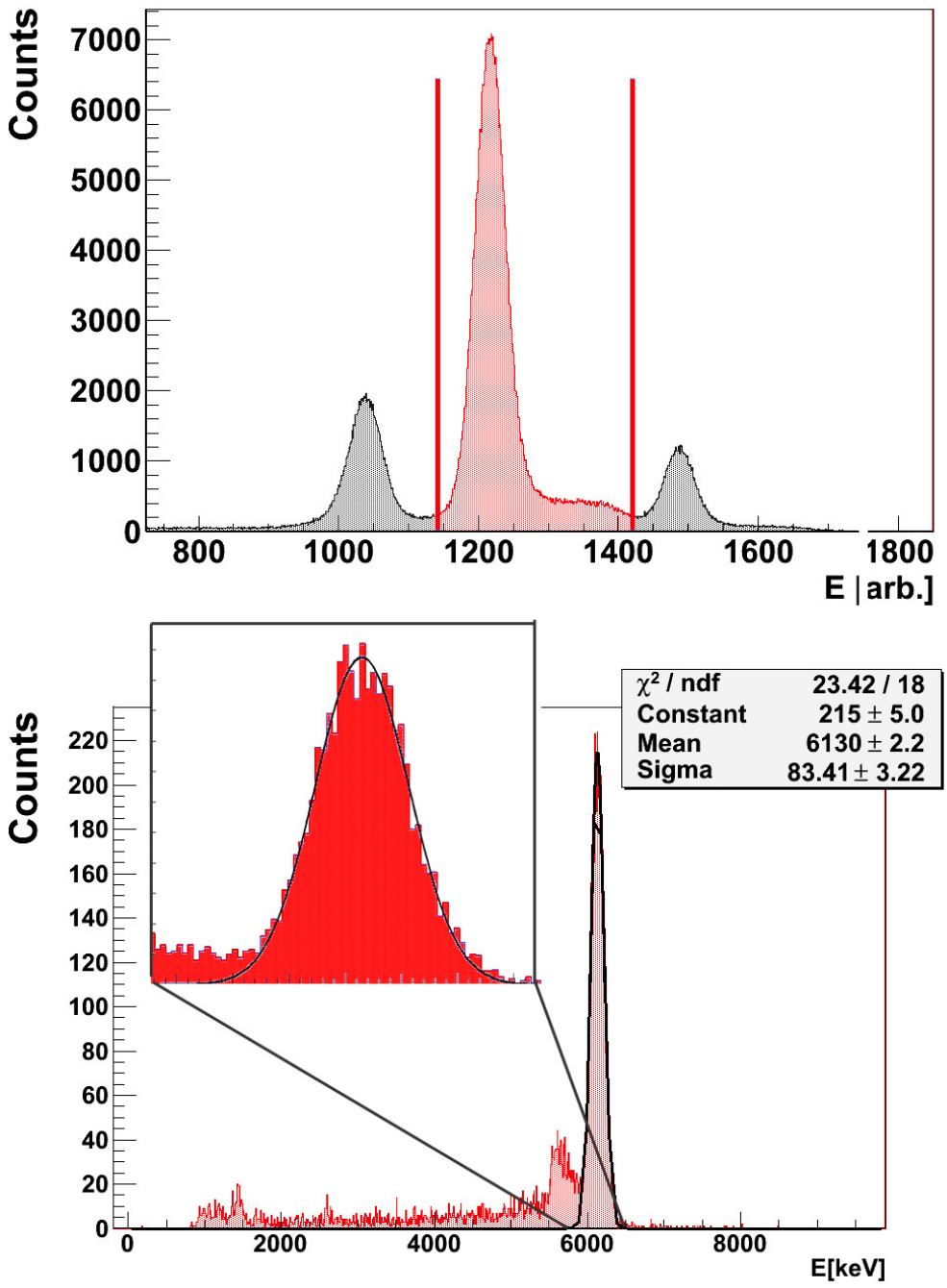

Figure 3.16: (Top) Three α-particle peaks from a typical silicon detector spectrum. Gates have been drawn around the resonant peak. (Bottom) The summed spectrum of all coincident γ-rays from all runs. A Gaussian fit to the full energy peak at 6.13 MeV (inset) determines N_{γ}^{peak}.

4 Data Collection and Reduction

4.1 Introduction

The data used in the present analysis combine the result from experiments that took place in January and July 2009. The $^{9}\mathrm{Be}(\gamma,n)^{8}\mathrm{Be}$ experiment was essentially a counting experiment. Both the INVS and *Molly* were setup to generate proportional scalar counts. Each count above background was recognized as a neutron or gamma-ray respectively, and each were weighted by a detector efficiency (see Chap. 3). Additionally, *Molly* and the HPGe were setup to generate γ-ray spectra. Descriptions of the methods of data collection, and the methods of data reduction follow.

4.2 Electronics

The electronic setup for the $^{9}\mathrm{Be}(\gamma,n)^{8}\mathrm{Be}$ experiment was very simple. All data were acquired and stored using TUNL's proprietary data acquisition (DAQ) software, CODA. The data stream consisted of several digital signals sent to scalars, and two analog signals which were stored using an Amplitude-to-Digital Converter (ADC). The scalars were read and recorded at regular intervals (usually every 10 seconds) during the course of a run, and also once at the end of the run. The analog signals came from the HPGe and *Molly*, and generated γ-ray spectra.

Each signal from the HPGe or *Molly* was split into two signals. One signal was processed by a discriminator to generate a scalar count, and also to trigger a DAQ gate in the ADC for the other signal. The second signal was delayed in order to arrive inside the generated gate for the ADC. Logic circuits called "pile-up rejection" circuits (PUR), were designed to veto multiple triggers within a single gate. The INVS counter has on-board electronics which generate +5 V TTL pulses when a tube discriminates a signal above a pre-set threshold.

The January run used γ-ray energies between 2.5 and 5.2 MeV, and the July run used

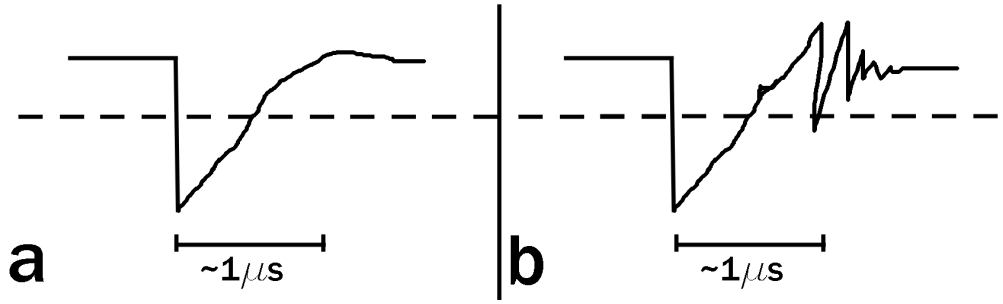

Figure 4.1: (a) Sketch of a normal signal from the NaI detector. (b) Sketch of a NaI signal with ringing. A discriminator may generate more than one scalar count for the ringing signal. NaI signals are on the order of 1 μs.

γ-ray energies between 1.5 and 3.2 MeV. At the end of the January run, it was observed that a mismatched impedance caused ringing, as depicted in Fig. 4.1, which sometimes generated multiple pulses for single events in *Molly*'s discriminator. The result of this wiring error was that the number of γ-ray counts generated by the discriminator was artificially high by an unknown amount. The problem of ringing and multiple-pulses was resolved in the July run, and consequently, the *Molly* scalar data from the January run are normalized to *Molly* scalar data from the July run using the overlapping region from the two runs. Figure 4.2 shows the yields for both data sets.

4.3 The Data

The data were analyzed in spreadsheets and with ROOT software. The manner in which the scalar data were stored allowed the user to display graphically the evolution of data collection. Figure 4.3 attempts to display some of the relevant data from a single run at E_γ = 2.5 MeV. The triangles (highlighted in green) represent the relative rate of neutron signals from the INVS over the course of the experiment. Notice the discontinuity in the rate of observed neutrons when the target changes from D_2O to graphite, graphite to ^{9}Be, and ^{9}Be to target out (T.O.). This happens because the γ-ray energy is above neutron threshold for deuterium and ^{9}Be, and nothing else.

Next, observe the monotonically decreasing filled white circles (highlighted in blue). These represent the rate of counts from the scintillating paddles throughout the experiment. In this case, flux was not constant, but decayed slowly during this run. However, now observe the black stars (highlighted in red). These represent the ratio of counts/time in the scintillating paddle to the counts/time observed in the NaI crystal. Notice that despite the decaying absolute flux, the paddle normalized flux is constant for each target. The discontinuities here are the result of different γ-ray attenuations through each target. However, notice that the attenuation through graphite and ^{9}Be are nearly identical. The ratio of this target-dependent

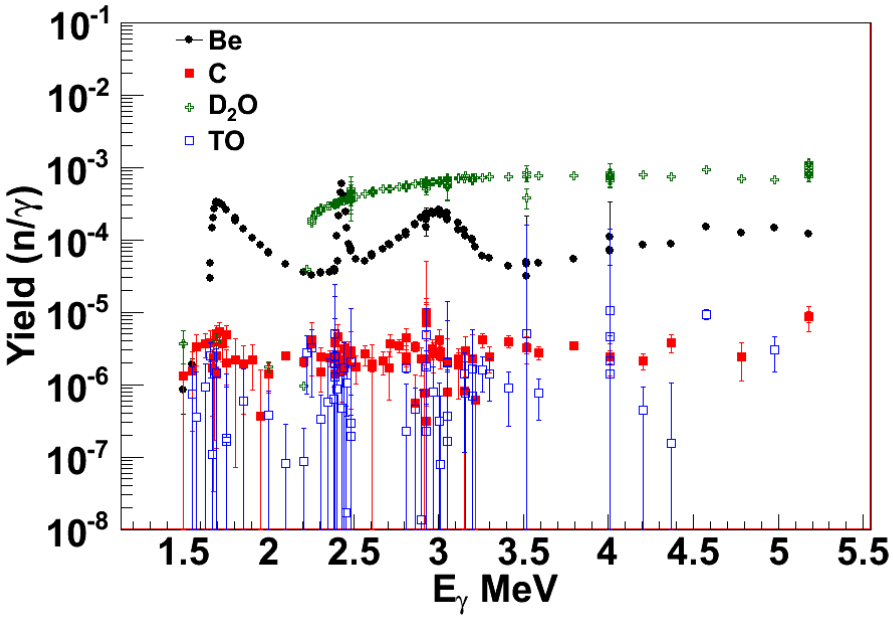

Figure 4.2: The measured yields for all targets on a log scale. The ^{9}Be and D_2O targets have yields which are 1-3 orders of magnitude larger than the yield from graphite. The yield from T.O. is mostly consistent with zero.

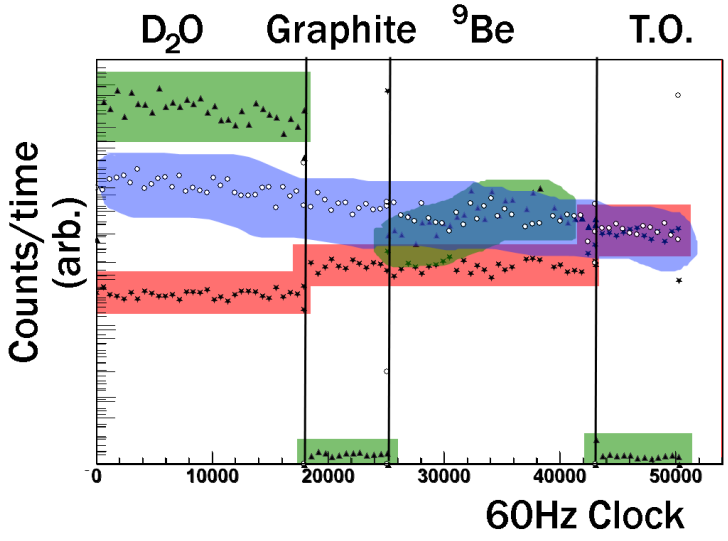

Figure 4.3: The evolution of a single run at 2.5 MeV. The meaning of each group of points is explained in the text.

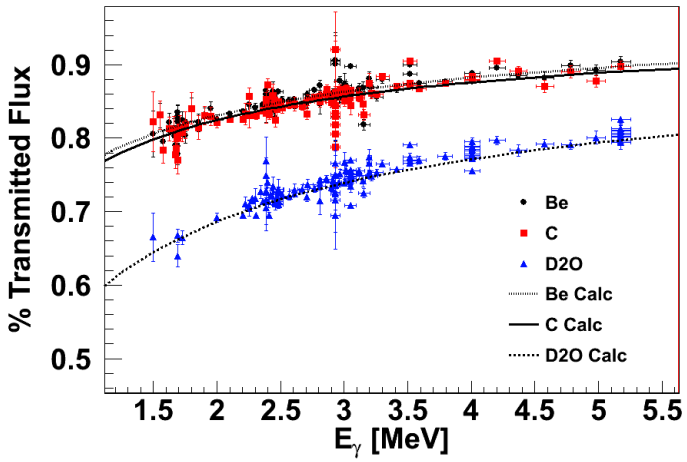

Figure 4.4: Measured attenuation through each target is in good agreement with calculations.

value to the value for T.O. is a direct measurement of the γ-ray attenuation through each target (see Fig. 4.4). Calculations for the attenuation of γ-rays through each material were performed using attenuation coefficients provided by the National Institute of Standards and Technology (NIST) [Hub89], and matched the observed attenuation very well (see Fig. 4.4).

4.4 Absolute γ-Ray Measurements

The total number of γ-rays bombarding a target is,

$$N_\gamma = \frac{N_{Molly}}{\chi_{Pb}(E_\gamma)\chi_{targ}(E_\gamma)\epsilon_\gamma}, \tag{4.1}$$

where N_{Molly} is the number of counts above background detected by *Molly*, χ_{Pb} and χ_{targ} are measurements of attenuation which are energy dependent and ϵ_γ is the efficiency of *Molly* which is γ-ray energy independent over the range of γ-ray energies considered here. The methods used to ascertain *Molly*'s detection efficiency were described in Chap. 3. In this section, I will describe the methods used for determining the attenuation resulting from the Pb attenuators and the targets.

Attenuation Measurements

The attenuation may be visualized in the following way. A plot of the ratio of N_{Molly} to N_{PADDLE} is shown in Fig. 4.5. On a log scale, regularly spaced bands emerge corresponding to the proportionality

$$\log R \propto (T) \tag{4.2}$$

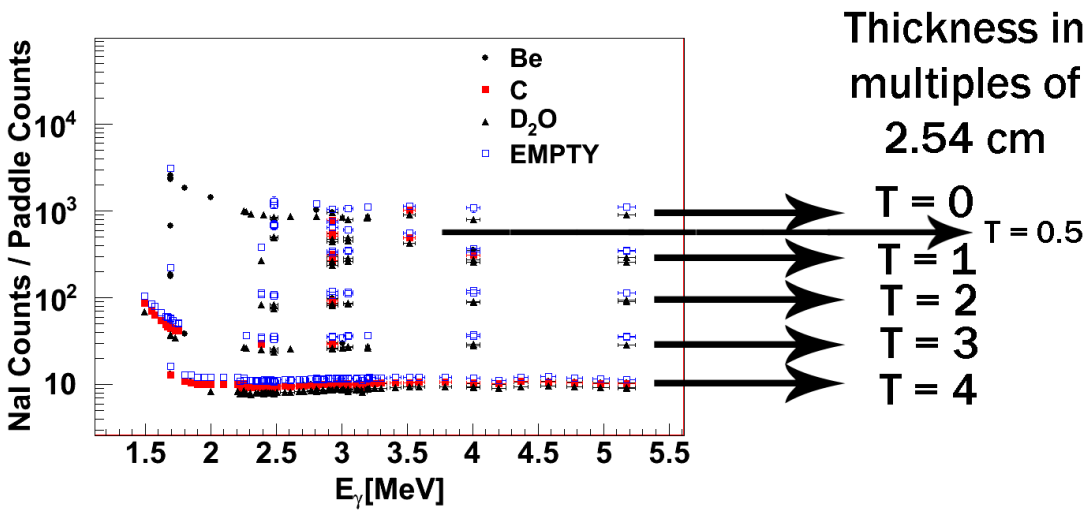

Figure 4.5: Plot of the ratio of raw counts in NaI detector to scintillating paddle counts.

where R is the aforementioned ratio, and T are the thicknesses of the Pb attenuators.

Measurements of the attenuation of γ-rays through each target and through Pb-attenuators were obtained so that, as much as possible, a statistical rather than systematic approach could be taken for deriving the absolute gamma flux. Attenuation of the gamma-ray beam downstream from the targets, but upstream from the gamma-ray beam monitor, was determined to be necessary to make this experiment viable. Keeping the absolute flux below 5×10^3 γ/s on the NaI or HPGe yields spectra that have negligible signal pile-up and well understood computer dead-time. However, maintaining 10^5 to 10^6 γ/s on target was essential for keeping signal counts well above the background in our neutron detector. Therefore, an instrument was designed to insert different thicknesses of Pb downstream from the target but upstream from the NaI and HPGe detectors. A thickness of Pb of 10.16 cm (7.62 cm) gave approximately a factor of 100 (30) reduction in intensity for most of the γ-ray energies in the experimental range (1.5 MeV $\leq$ E_γ $\leq$ 5.2 MeV). These attenuators were the primary attenuators used for measurements. Thicknesses of 5.08 cm, 2.54 cm, and 1.27 cm were also available for use during the experiment, in addition to unattenuated γ-ray beam.

To measure the actual loss of flux through our Pb-attenuators, the following approach was used. A γ-ray sensitive detector upstream of the Pb-attenuator behaves as a relative flux monitor (RFM). Downstream from the Pb-attenuator an absolute measurement of the γ-ray flux is made with the NaI detector. To make a measurement of the attenuation of a given thickness of Pb, two measurements are made in succession using the same incident γ-ray energy. A measurement is performed with the Pb attenuator in place, and a subsequent measurement is performed with the original Pb attenuator removed. For run i the intensity on the face of lead attenuator ($N_{\gamma 0}$) is related to the intensity on the face of the detector

(N_{Molly}) by

$$N_{\gamma 0} = \frac{N_{Molly}}{\exp\left(-\mu_{Pb} T\right) \epsilon(E_\gamma)}, \tag{4.3}$$

where μ is a Pb-attenuation coefficient, and T is the proportional to the thickness of the Pb attenuator. Now, consider the scintillating paddles which are upstream from the lead attenuator. The paddles generate scaler counts proportional to the γ-ray flux. The total number of γ-rays which are available to interact with the paddles is $N_{\gamma 0}$, so

$$N_{\gamma 0} = N_{\text{PADDLE}} / \epsilon_{\text{PAD}}. \tag{4.4}$$

Equation 4.4 is equivalent to Eq. 4.3. Consider that run i uses no attenuator and run j uses an attenuator of thickness T. Taking a ratio of run i to run j for the same E_γ removes all energy dependence, and yields

$$\frac{N^i_{Molly}\, N^j_{\text{PADDLE}}}{N^j_{Molly}\, N^i_{\text{PADDLE}}} = \exp(-\mu T) \equiv \chi_{Pb}, \tag{4.5}$$

which is the definition of attenuation.

A consequence of defining attenuation this way is that the INVS detector may be used in the same manner as the paddles so that

$$\frac{N^i_{Molly}\, N^j_{\text{INVS}}}{N^j_{Molly}\, N^i_{\text{INVS}}} = \exp(-\mu T) \equiv \chi_{Pb}. \tag{4.6}$$

The values for T are tabulated in Tables 4.3 and 4.4. Both RFMs yield values for T which are approximately 6% less than the measured value of T.

Differences observed between the measurements of attenuation and the attenuation predicted using NIST attenuation coefficients were initially believed to be the result of small-angle Compton scattering as illustrated in Fig. 4.6. This explanation, however, turns out to be inadequate. A first order approximation determines small angle Compton scattering to have a 1% effect on the observed attenuation coefficients. Simulations using MCNPX confirmed that the effect of small angle scattering was expected to be on the order of 1%.

The cause of the remaining discrepancy was not determined. The discrepancy is observed when using either the paddles or the INVS detector (in concert with the ^{9}Be or D_2O targets). It follows that if two independent RFMs (the paddles and the INVS), which use two independent physical processes (scintillation, and thermal neutron capture) to establish the relative flux, yield similar measures of attenuation, then it is unlikely that the discrepancy was the result of a systematic effect from either RFM. Furthermore, the intensity of the γ-ray beam was controlled so that *Molly* only experienced fluxes $<10^4$ γ/s. This rules out any possibility that the observed systematic effect is detector-induced. Because the measurement satisfies

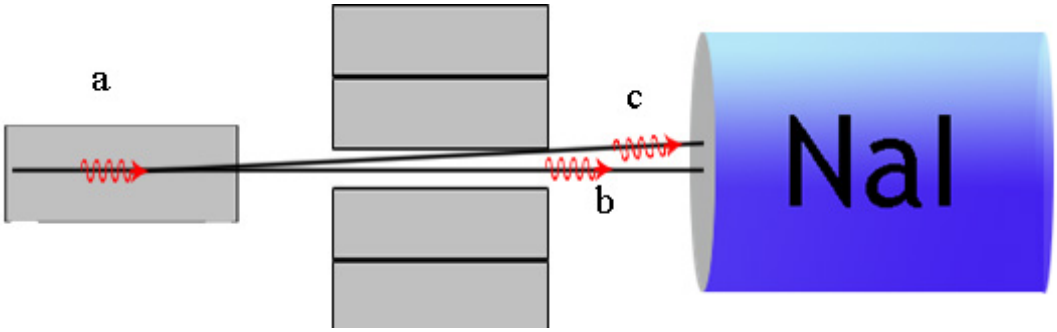

Figure 4.6: : (a) A γ-ray inside the Pb attenuator may scatter, pair-produce, photoabsorb, or exit without interaction. (b) Photons that do not interact with the Pb can be observed in the NaI detector. (c) γ-rays scattered at small angles will also be observed in the NaI detector, although these γ-rays are treated as removed when the NIST coefficients are used.

the conditions necessary to establish an accurate absolute measure of γ-ray flux, explaining the remaining discrepancy, while gratifying, is not necessary.

Measuring the attenuation that comes from the targets uses a similar approach. Flux is measured with a target in-beam (targ) and with that target out-of-beam (T.O.), and is normalized to the paddles. This has the form

$$\frac{N_{Molly}^{targ}}{N_{\mathrm{PADDLE}}^{targ}} \times \frac{N_{\mathrm{PADDLE}}^{\mathrm{T.O.}}}{N_{Molly}^{\mathrm{T.O.}}} \equiv \chi_{targ}. \tag{4.7}$$

The attenuation data for Pb and the targets are fit with an order-six polynomial (*pol6*). January and July data sets are treated separately due to the observation of small differences which are likely the result of slight geometrical differences between the two runs. Further discussion of data fitting and uncertainty are reserved for Sect. 4.8.

4.5 Absolute Neutron Measurement

The methods for obtaining an absolute measure of the number of neutrons was mostly described in Chap. 3. The measurement is bound to the absolute measure of γ-ray flux, the $^2\mathrm{H}(\gamma,n)^1\mathrm{H}$ cross-section of Ref. [Sch05], and the number of target nuclei. The result is

$$N_n = \frac{N_{\mathrm{INVS}} - N_{\mathrm{BIFC}}}{\epsilon_n(E_n)}, \tag{4.8}$$

where $\mathrm{N_{INVS}}$ is the number of counts above room-background detected by the INVS counter, $\mathrm{N_{BIFC}}$ are the number of beam-induced false counts (BIFC) and $\epsilon_n(E_n)$ is the efficiency of the INVS which depends on the energy of the neutrons being detected.

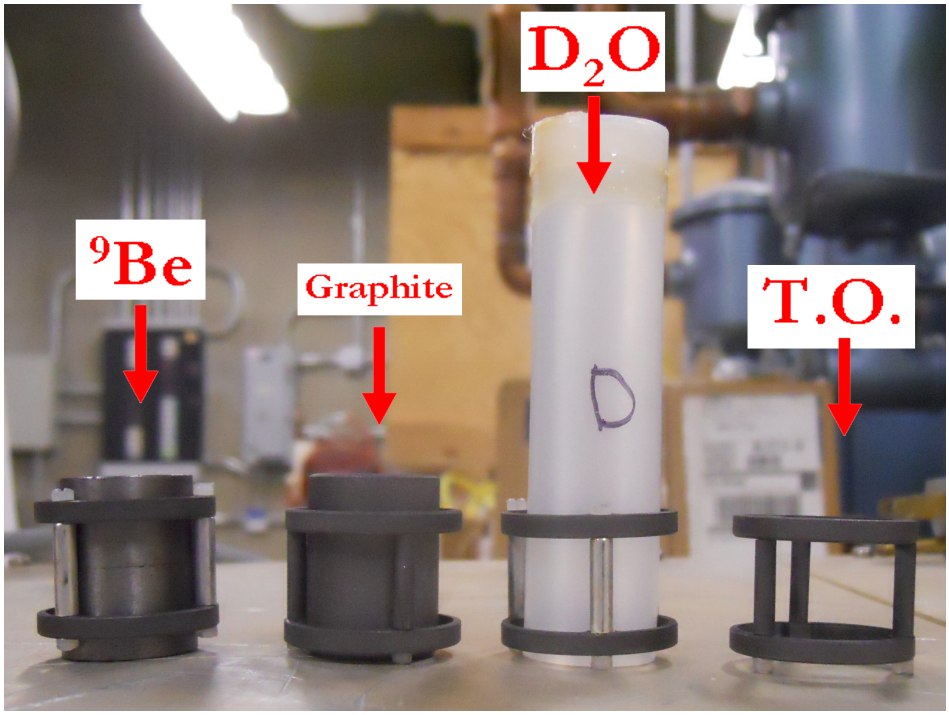

Figure 4.7: Photograph of the targets used in this experiment. Shown with the targets is the small graphite frame used to position the targets inside the revolving target chamber.

4.6 Absolute Target Thickness Measurement

The number of target nuclei available for interaction is an essential component of the cross section equation. In these experiments, the γ-ray beam was of smaller diameter than the target. Targets were cylindrical, with the cylinder faces normal to the γ-ray beam. Under these conditions, the total number of target nuclei per unit area,

$$N_t/A = (\rho)\left(\frac{1}{m_{mol}}\right)(N_A)(\beta_{targ}) \times \ell \times f, \tag{4.9}$$

where ρ is the density of the target material with units g/cm^3, m$_{mol}$ is the molar mass of the target with units of g/mol, N$_A$ is Avogadro's number with units of atoms/mol (or molecules/mol), β_{target} is the number of target nuclei per molecule, ℓ is the length of the target in cm, and f is a thick target correction factor to be described.

As γ-rays penetrate a thick target, a significant fraction will interact in ways other than photodisintegration (Compton scattering, photoabsorbtion etc.). These interactions remove γ-rays from the beam, continuously changing the number of γ-ray-target-nucleus pairs available for photodisintegration. The number of γ-rays removed from the beam is a function of the target thickness and the attenuation coefficient for the target.

The thick target correction mentioned in Sect. 3.2.4 (Eq. 3.6) will be derived here. Con-

Target Material	Nominal ℓ (cm) Jan.	Nominal ℓ (cm) July	ℓ (cm) from Attenuation Measurement Jan.	ℓ (cm) from Attenuation Measurement July
^{9}Be	2.54	2.54	2.55 ± 0.02	2.60 ± 0.02
graphite	2.54	2.54	2.56 ± 0.02	2.49 ± 0.02
D_2O	7.59	7.59	7.28 ± 0.03	7.50 ± 0.03

Table 4.1: A comparison of nominal target length and target length determined from attenuation data. Uncertainties shown are the uncertainties from fits of a constant value to plots of target length, (ℓ), vs. E_γ for each data set. Reduced χ^2 for each fit was 0.3 (Jan) and 1.4 (July).

sider the luminosity, L, of photons within a material with number density ρ and thickness dx. The change in luminosity as the beam passes through a distance dx in a target may be defined as

$$dL = I(x)\rho dx \ . \tag{4.10}$$

For a thick target, the intensity of photons decreases exponentially in x so that the intensity of photons at any point within the target obeys

$$I(x) = I_0 \exp\left(-\mu x\right), \tag{4.11}$$

where μ is an attenuation coefficient with units of inverse length. The change dL through the target will obey

$$dL = I_0 \exp(-\mu x)\rho dx \ . \tag{4.12}$$

Integrating dL from zero to the total thickness, T, gives the luminosity after the target,

$$L' = -I_0\rho \frac{\exp\left(-\mu x\right)}{\mu}\Bigg|_{x=0}^{x=T} = I_0\rho\frac{1-\exp\left(-\mu T\right)}{\mu} \ . \tag{4.13}$$

Now writing

$$L' = f \ I_0\rho T \ , \tag{4.14}$$

one can see that

$$f = \frac{1-\exp\left(-\mu T\right)}{\mu T} \tag{4.15}$$

The initial number of photons, $N_{\gamma 0}$, is proportional to initial intensity, I_0, so $N_{\gamma 0}$ may be substituted for I_0 in Eq. 4.14 which yields the thick target correction factor f mentioned in Sect. 3.2.4.

Because data were taken with and without the target attenuating the γ-ray beam, ratios

of γ-ray scalers for target-in to target-out provide a measure of target length, and thus a measure of the total number of target nuclei. Precision is limited to 5% (systematic) in accordance with the uncertainty reported for the attenuation coefficients for γ-ray energies > 1 MeV [Hub89]. Table 4.1 shows target thickness derived from the measure of attenuation in comparison to target thickness measured directly. Both measurements agree with nominal target thickness within 5%.

4.7 Total Cross Section

When assuming that the INVS detector covers a solid angle of 4π the general equation for calculating a photoneutron cross section is

$$\sigma = \frac{N_n}{N_\gamma N_t / A}. \tag{4.16}$$

The result, related by the measured quantities, is

$$\sigma_{\gamma,n} = \frac{(N_{\text{INVS}} - N_{\text{BIFC}})\chi_{Pb}\chi_{targ}\epsilon_\gamma}{N_{Molly}(\rho)\left(\frac{1}{m_{mol}}\right)(N_A)(\beta_{targ})\ell f\ \epsilon_n(E_n)}. \tag{4.17}$$

For energies above 2.225 MeV, an alternate reckoning of the ^{9}Be$(\gamma,n)^8$Be cross section may be found by directly normalizing with the ^{2}H$(\gamma,n)^1$H cross section. This formula is generated by taking a ratio of Eq. 4.17 for ^{9}Be and ^{2}H. Many terms cancel out from the equation which means that absolute detection efficiencies and terms for attenuation through Pb need not be known. This formula is written as

$$\sigma_{^9Be(\gamma,n)} = \sigma_{^2H(\gamma,n)}\left(\frac{(N_{\text{INVS}} - N_{\text{BIFC}})^{9Be}}{(N_{\text{INVS}} - N_{\text{BIFC}})^{2H}}\right)\left(\frac{N^{^2H}_{Molly}}{N^{^9Be}_{Molly}}\right)\left(\frac{\chi_{^9Be}}{\chi_{^2H}}\right)\left(\frac{N^{^2H}_T/A}{N^{^9Be}_T/A}\right)\left(\frac{\epsilon^{^2H}_n}{\epsilon^{^9Be}_n}\right). \tag{4.18}$$

A Table with both absolute and normalized cross section measurements may be found in Sect. 7.2.

4.8 Error Analysis

A key feature of this work was to make measurements with reference to known standards in order to reduce or remove, where possible, systematic uncertainties. The uncertainties of the components of the cross-section, and the methods used to determine the uncertainty in the measurement of $\sigma_{\gamma,n}$ will be discussed next.

Scaler	average background (c/s) JANUARY	average background (c/s) JULY	typical relative unc. (approx)
Molly	932.57	1023.6	0.1%
INVS Inner	1.92	1.78	0.5-5%
INVS Outer	1.86	1.80	0.5-5%
INVS Total	3.76	3.58	0.5-5%
Paddles	0.204	0.194	1%

Table 4.2: Table of the time-averaged background rates.

4.8.1 Uncertainty

I will begin by addressing the uncertainty of each scaler data set collected during experiments. The scalers to which this will apply will be the following: *Molly*, the INVS (Inner, Outer, Total) and the scintillating paddles. What is shown below is generally valid for all scaler data.

Let N_{SCALER} represent N_{INVS}, N_{Molly} or N_{PADDLE} and be calculated as

$$N_{\text{SCALER}} = N_{raw} - N_{background}, \tag{4.19}$$

with

$$N_{background} = \frac{N_{overnight}}{t_{overnight}} \times t_{run}, \tag{4.20}$$

where N_{raw} is the total number of scalar counts obtained in SCALER for a given target during a given run and $N_{background}$ is primarily a time averaged background rate scaled by the time of the run being analyzed. The rate of the background is established by averaging runs which collected data overnight.

Thus, the absolute uncertainty of N_{SCALER} is

$$U_{N_{\text{SCALER}}} = \sqrt{N_{\text{SCALER}} + N_{background}} = \sqrt{N_{raw}}, \tag{4.21}$$

making the relative uncertainty

$$\frac{U_{N_{\text{SCALER}}}}{N_{\text{SCALER}}} = \frac{\sqrt{N_{raw}}}{N_{\text{SCALER}}}. \tag{4.22}$$

In a typical run I find that for *Molly*, $N_{raw} = 1.45\times10^6$ counts over the course of 600.0 seconds. The rate of background in *Molly* is 1023.6 Hz, meaning $N_{background} = 614160$ counts and thus $N_{Molly} = 835840$ counts. In this case, $U_{N_{Molly}}$ is ≈ 1204 counts and so the relative uncertainty in N_{Molly} is $\approx 0.15\%$. Table 4.2 gives the values for time-averaged backgrounds used in the $^9\text{Be}(\gamma, n)^8\text{Be}$ experiment.

Having established the methods for determining uncertainties associated with scalers, I

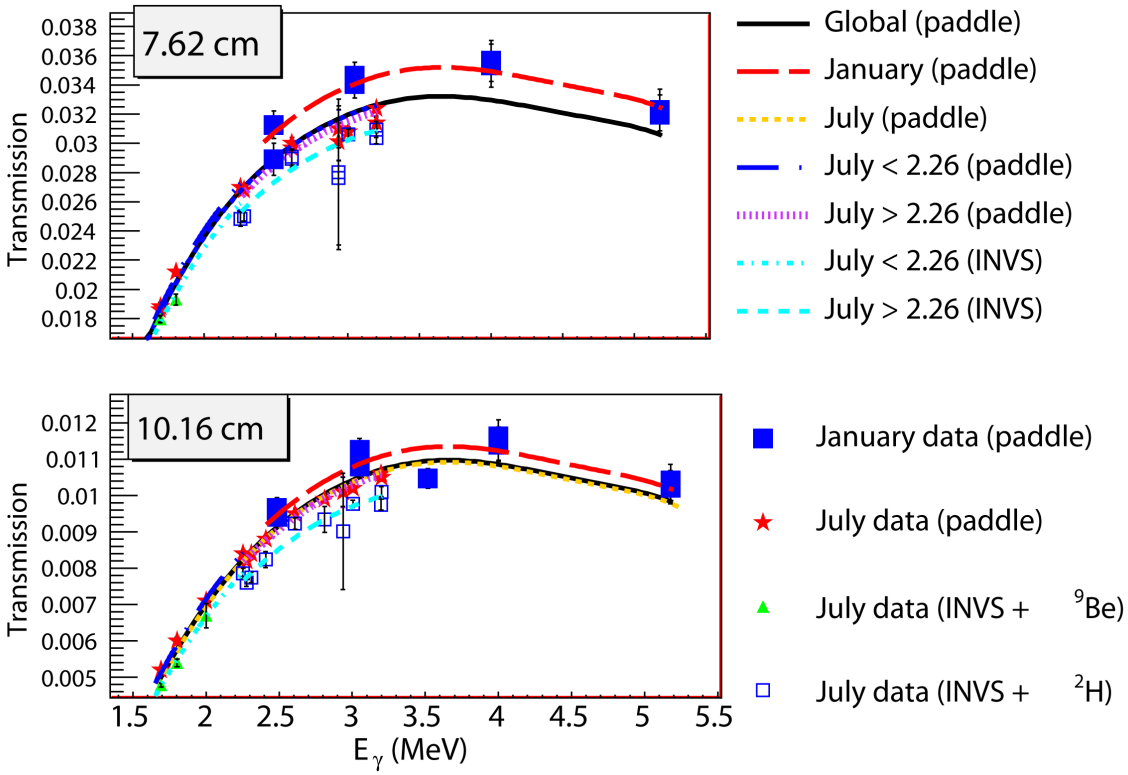

Figure 4.8: Attenuation data and fits for 10.16 cm and 7.62 cm Pb attenuators.

will focus now on the other components of Eq. 4.1.

The measurement for the attenuation caused by Pb of thickness T has the form of Eqs. 4.5 and 4.6. The paddles and the INVS are upstream of the Pb attenuators and independently provide flux normalization to *Molly*. The uncertainty of χ_{Pb} at a point is just the uncertainty of a product:

$$U_{\chi_{Pb}} = \chi_{Pb}\sqrt{\left(\frac{U_{N^T_{Molly}}}{N^T_{Molly}}\right)^2 + \left(\frac{U_{N^0_{Molly}}}{N^0_{Molly}}\right)^2 + \left(\frac{U_{N^T_{RFM}}}{N^T_{RFM}}\right)^2 + \left(\frac{U_{N^0_{RFM}}}{N^0_{RFM}}\right)^2}, \tag{4.23}$$

For runs where where Pb attenuation was being determined, the limiting factor was counts in the RFM. Relative uncertainties of 1% were attained for most runs. This ensured that the relative uncertainty in χ_{Pb} was 1.5%. For the 10.16 cm (7.62 cm) attenuator, the attenuation was measured at 5 (4) different γ-ray energies in January and 12 (8) different γ-ray energies in July. The precision of the measurements taken in January (July) were about 3.5% (1.5%) for each measurement. It is observed that the measure of attenuation is sensitive to the close geometry of the attenuators with *Molly*; therefore, the January and July data are treated separately. Slight differences in the distance between the Pb-attenuator and *Molly* rendered systematically different measures of attenuation (see Fig. 4.9). The following model was

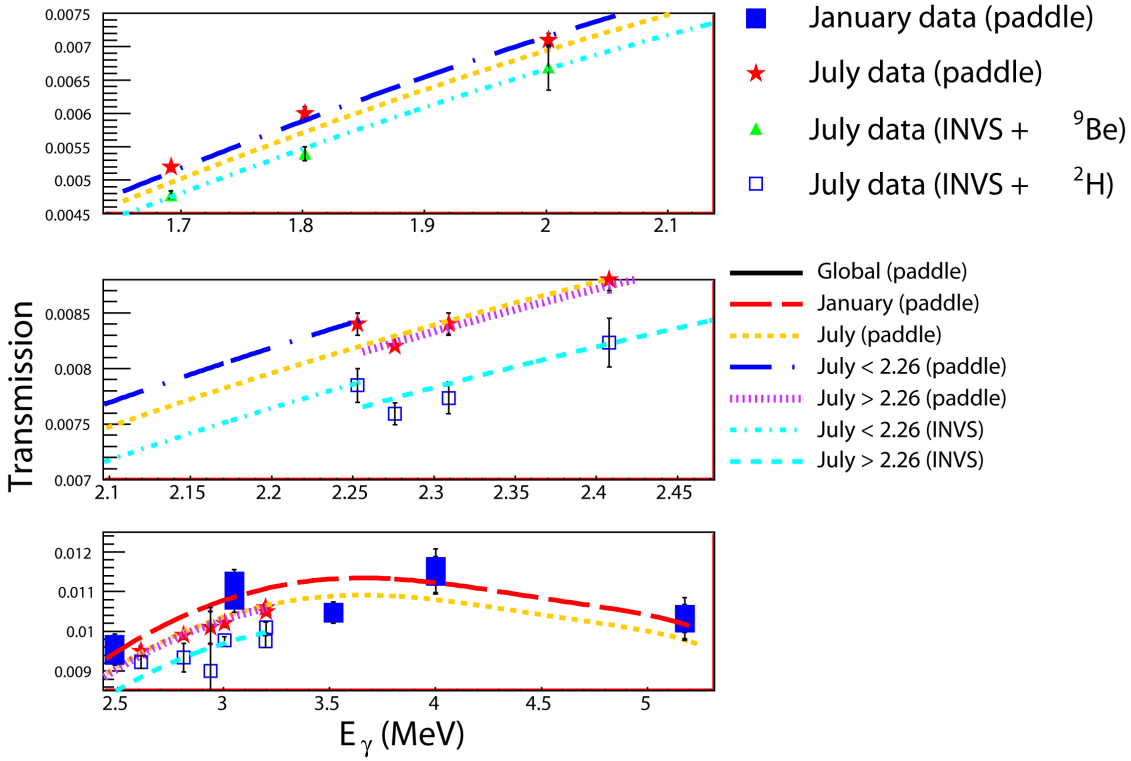

Figure 4.9: A zoomed in look at different regions of attenuation data and fits for the 10.16 cm Pb attenuator. Notice that the "kink" in the second plot affects both RFMs in nearly the same way.

chosen to attempt to fit the data. A table of attenuation coeficients for Pb is generated from a NIST tool. These attenuation coefficients (μ) are assigned a systematic uncertainty of ± 5% by NIST. For the purpose of fitting, an uncertainty of 0.1% was assigned to these coefficients and they were fit using an order-6 polynomial (*pol6*) with an overall χ^2 per number of degrees of freedom (NDF) (or reduced χ^2) of 0.75. This means that the model of $\mu(E_\gamma)$ as a *pol6* and the 0.1% uncertainty assignment were well matched over the range of 1.5 MeV $\leq$ E_γ $\leq$ 5.2 MeV. Now armed with a function for $\mu(E_\gamma)$ over the desired energy range, the new model was used to fit the attenuation data. The attenuation data collected with the 10.16 (7.62) cm attenuator were fit with

$$\frac{I}{I_0} = \exp -\mu(E)T \tag{4.24}$$

where T is the single free parameter which is expected to have a value close to 10.16 (7.62) cm. It it worth noting here that the present attenuation measurements exist without reference to the attenuation coefficients being used. By referencing the attenuation coefficients provided by NIST, the attenuation was modeled with something better than a linear interpolation between the data points. Plots of the fitted attenuation data are shown in Fig. 4.8. Notice that T for January and July are systematically different.

Tables 4.3 and 4.4 contain the values of T obtained in the fit along with reduced χ^2 values. A surprising result was that the the different RFMs give slightly different measures of attenuation (about 5%), which generally do not agree with each other given their error bars. This implies that an unknown systematic uncertainty is affecting at least one of the RFMs. Since the systematic effect is unknown and neither RFM may be prefered,the models were assigned equal weights and averaged. A systematic uncertainty assigmnet of ± 2.5% was deemed appropriate.

One final nuance was observed within the July data set. It appears that if the energy range is split at E_γ= 2.26 MeV, and the attenuation data < 2.26 MeV are fit separately from data > 2.26 MeV, the reduced χ^2 value over that range is significantly improved (See Fig. 4.9 and Table 4.3). It is likely that the Pb-attenuators were moved and relocated during the July runs which caused a small systematic change in what *Molly* observed. With all of the reduced χ^2 values being close to 1, I infer that the model is good and that the attenuation of the γ-ray beam through Pb has been measured with a statistical precision of 3.5% (1.5)% in January (July).

For the present model, the fit values of T have an uncertainty associated with the fit, U_T. Using the method of partial derivatives to assess the uncertainty of the model, one finds that the relative uncertainty is

$$U_{\chi_{Pb}} = U_T \times \frac{\partial \chi_{Pb}}{\partial T} = -\mu U_T \exp(-\mu T), \tag{4.25}$$

	T = 10.16	χ^2 per NDF	ratio to 10.16	T = 7.62	χ^2 per NDF	ratio to 7.62
Global	9.504 ± 0.005	3.94	93.5	7.171 ± 0.006	3.817	94.1
Jan	9.433 ± 0.020	1.25	92.8	7.049 ± 0.025	0.547	92.5
July	9.515 ± 0.007	2.04	93.6	7.173 ± 0.006	4.36	94.1
July < 2.26	9.460 ± 0.015	.726	93.1	7.136± 0.009	1.85	93.6
July > 2.26	9.529 ± 0.008	.452	93.7	7.201± 0.008	2.08	94.5

Table 4.3: Table of fit parameters and χ^2 per number of degrees of freedom (NDF) for measurements of attenuation through Pb using the scintillating paddles as a RFM.

	T = 10.16	χ^2 per NDF	ratio to 10.16	T = 7.62	χ^2 per NDF	ratio to 7.62
July < 2.26	9.595 ± 0.017	0.311	94.4	7.235± 0.014	1.85	95.0
July > 2.26	9.653 ± 0.011	1.54	95.0	7.286± 0.012	2.08	95.6

Table 4.4: Table of fit parameters and χ^2 per number of degrees of freedom (NDF) for measurements of attenuation through Pb using the INVS detector as a RFM.

making the relative uncertainty

$$\frac{U_{\chi_{Pb}}}{\chi_{Pb}} = -\mu U_T. \tag{4.26}$$

Though the uncertainty in attenuation at a point is 1.5%, this evaluation uses each measurement to establish a value for T. The uncertainty in the model values of T is about 0.6% for the 10.16 cm and 7.62 cm attenuators, and yields the same relative uncertainty for χ_{Pb}. The measurements of attenuation through the targets (χ_{targ}) are generally performed in the same way. However, these measurements were performed at nearly every energy and with better statistical precision.

The final component of Eq. 4.1 is ϵ_γ which is the γ-ray detection efficiency of *Molly*. This was determined experimentally using the ^{19}F$(p,\alpha\gamma)$ experiment. Recall that the measured peak efficiency of *Molly* is

$$\epsilon_{peak} = \frac{N_\gamma^{peak}}{\frac{d\Omega}{4\pi} \times N_\alpha} \tag{4.27}$$

where N_γ^{peak} is the number of detected γ-rays in the full energy peak, $\frac{d\Omega}{4\pi}$ is the fractional solid angle defined by the lead shielding, and N_α is the number of α-particles detected for the resonant reaction. The uncertainties of N_α and N_γ are determined in a manner similar to the methods described above.

The uncertainty of $\frac{d\Omega}{4\pi}$ cannot be rid of systematic uncertainties because a model for γ-ray-attenuation must be used to obtain the correct solid angle, and observed attenuation is

	T = 10.16	Range of χ_{Pb}	Approx. Rel. Unc. $U_{\chi_{Pb}}/\chi_{Pb}$	Systematic Unc.
January	9.433 ± 0.020	0.5 - 1.2%	1%	2.5%
July < 2.26	9.528 ± 0.011	0.5 - 1.2%	0.6%	2.5%
July > 2.26	9.591 ± 0.011	0.5 - 1.2%	0.6%	2.5%
	T = 7.62	Range of χ_{Pb}	Approx. Rel. Unc. $U_{\chi_{Pb}}/\chi_{Pb}$	Systematic Unc.
January	7.185± 0.008	1.8 - 3.6%	1%	2.5%
July < 2.26	7.185± 0.008	1.8 - 3.6%	0.6%	2.5%
July > 2.26	7.244± 0.007	1.8 - 3.6%	0.6%	2.5%

Table 4.5: Table of averaged parameters and uncertainties T and χ_{Pb}.

Parameter	value (N)	relative unc. $(1/\sqrt{N})$
N_α	1.3×10^7	0.02%
N_γ	4487	1.5%

Table 4.6: Statistical parameters for determining the solid angle in the $^{19}F(p,\alpha\gamma)$ experiment.

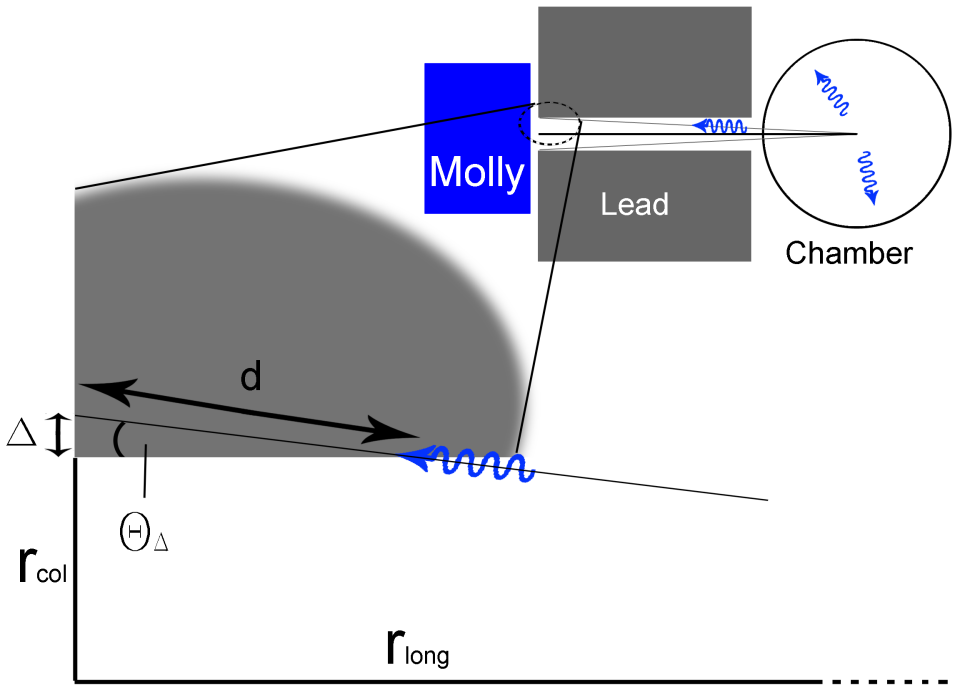

Figure 4.10: Geometry of $^{19}F(p,\alpha\gamma)$. Gamma-rays along the flight path shown experience attenuation corresponding to a distance d of Pb.

Parameter	value	relative unc.
r_{long}	31.05 ± 0.03 cm	~0.1%
r_{col}	1.27 ± 0.01 cm	~0.8%
θ_1	2.342 ± 0.019 deg	~0.8%
$\frac{d\Omega}{4\pi}$ (uncorrected)	(4.18 ± 0.07)×10^{-4}	~1.6%

Table 4.7: Parameters for determining the solid angle in the $^{19}F(p,\alpha\gamma)$ experiment.

geometry dependent as was shown in the calculations for χ_{Pb}. However, an analytic form establishes the solid angle which includes effects of attenuation though lead. Recall that several cm of Pb collimated the γ-rays to a 2.54 cm diameter spot on the center of the face of *Molly*. This configuration replicated beam-like conditions. At the end of the lead collimator, which has radius r_{col}, and is a distance r_{long} from the target, some γ-rays must penetrate a small amount of lead before reaching *Molly*. Thus, these γ-rays experience attenuation commensurate with the hypotenuse of a right triangle which may be calculated. For an incremental displacement in the radial direction, Δ, a γ-ray emitted at $\theta_\Delta = \tan^{-1}\left[(r_{col}+\Delta)/r_{long}\right]$ must travel a distance, d, through Pb where

$$d = \frac{\Delta}{\sin\left[\tan^{-1}\left(\frac{r_{col}+\Delta}{r_{long}}\right)\right]}, \tag{4.28}$$

meaning the effect of attenuation may be calculated at a given radius beyond the collimator edge as

$$\frac{I}{I_0} = \exp -\mu d. \tag{4.29}$$

The unobstructed angular opening lies between 0 and $\theta_1 = \tan^{-1}(r_{col}/r_{long})$, the calculation for unattenuated fractional solid angle is

$$\frac{d\Omega}{4\pi} = \frac{1}{4\pi}\int_0^{2\pi} d\phi \int_0^{\theta_1} \sin(\theta) d\theta = \frac{1}{2}\left(1-\cos(\theta_1)\right). \tag{4.30}$$

Figure 4.11 compares the calculated fractional solid angle with the fractional solid angle found through simulations in MCNPX. The photo-atomic cross sections used in the simulation ultimately come from the Evaluated Photon Data Library (EPDL97) [Cha06] which claims uncertainties of 1-2% for 1.5 MeV $\leq E_\gamma \leq$ 5.2 MeV. The uncertainties of each component of N_γ are listed in table 4.9.

I now move to address the uncertainty of N_t/A. The only real contributions to its uncertainty in Eq. 4.9 come from the ℓ and f. The length of the target ℓ is measured directly with calipers to high precision. The D_2O target is a liquid contained within a thin walled cylinder. The walls of the cylinder were designed to be 10 mil. (0.254 mm) thick. The parameter f

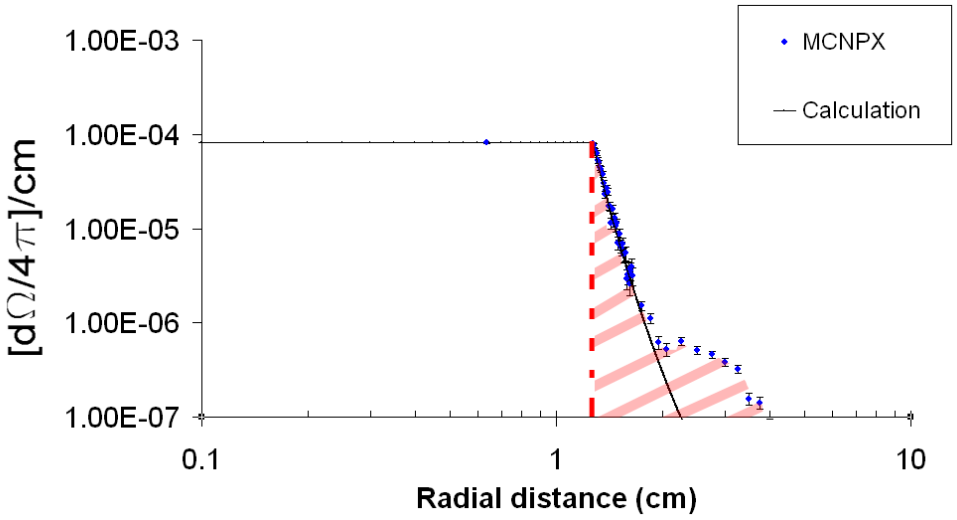

Figure 4.11: A calculation of $\frac{d\Omega}{4\pi}$/cm which includes the effects of attenuation from the Pb collimator is very close to MCNPX simulations of the flux of 6.13 MeV γ-rays vs. radius given the experimental geometry. The value for $\frac{d\Omega}{4\pi}$/cm is constant until the edge of the collimator is reached at r = 1.27 cm. The corrections to the solid angle (shaded area) for attenuation in the collimator, scattering in the thin window of the chamber and finite geometry amounts to an effect of approximately 16.8%.

Region	$\frac{d\Omega}{4\pi}$	contribution to $\frac{d\Omega}{4\pi}$	relative systm. unc.
r < 1.27 cm	4.09×10^{-4}	~83.2%	1.6%
r > 1.27 cm	0.82×10^{-4}	~16.8%	2%
all r	4.92×10^{-4}	100%	1.7%

Table 4.8: MCNPX-simulated parameters for solid angle in the ^{19}F$(p,\alpha\gamma)$ experiment. The 0.2% difference between the value for solid angle for r < 1.27 and the value in line 4 of Table 4.7 comes from scattering on the thin window of the chamber which was not calculated.

Parameter	relative stat. unc.	relative syst. unc.
N_{Molly}	0.1%	0.0%
χ_{Pb}	0.6 - 1.0%	2.5%
χ_{targ}	0.2%	0.0%
ϵ_γ	1.5%	1.7%
N_γ	2.1%	3.0%

Table 4.9: Table of statistical and systematic uncertainties for measurements of N_γ.

Target	thickness and unc.	relative syst. unc.
^{9}Be	2.54 ± 0.01	0.4%
graphite	2.54 ± 0.01	0.4%
D_2O	7.59 ± 0.05	0.7%

Table 4.10: Table of parameters for N_t/A.

parameter	Relative stat. unc.	Relative syst. unc.
ℓ	0%	< 1%
f	0.2%	0%
N_t/A	0.2%	< 1%

Table 4.11: Table of parameters for N_t/A.

may be interpreted directly from measurements. Recall Eq. 4.15,

$$f = \frac{1 - \exp(-\mu T)}{\mu T}, \tag{4.31}$$

which may be rewritten in terms of measured parameters as

$$f = \frac{1 - \chi_{targ}}{-\ln[\chi_{targ}]}. \tag{4.32}$$

Typical values for f range from 0.84 to 0.95. The uncertainty of f, given a 1% uncertainty in χ_{targ}, is found by

$$U_f = U_{\chi_{targ}} \times \frac{\partial f}{\partial \chi_{targ}} = U_{\chi_{targ}} \times \left[\frac{1 - \chi_{targ}}{\chi_{targ} (\ln[\chi_{targ}])^2} + \frac{1}{\ln[\chi_{targ}]} \right], \tag{4.33}$$

which amounts to approximately the same relative uncertainty as for χ_{targ}.

Next, I will address the uncertainty of N_n. The uncertainty for ϵ_n comes from the measurement of $^{2}H(\gamma, n)^{1}H$,

$$\epsilon_n = \frac{N_{\text{INVS}} - N_{\text{BIFC}}}{(N_\gamma)(N_t/A)\left(\sigma_{[^{2}H(\gamma,n)^{1}H]}\right)}. \tag{4.34}$$

The parameter N_{BIFC} comes from γ-rays which have scattered from the target and ionized the gas in the tubes of the INVS enough to trigger a signal. The graphite target was used to measure this effect. When the graphite target was in place, the INVS displayed a higher background than when no γ-ray beam was in the room. The fraction of γ-rays which are not transmitted through the target is (1-χ_{targ}). The number of these non-transmitted γ-

rays which scatter into the detector volume is related to the fractional contribution of incoherent scattering, κ_{scat}, to total attenuation χ_{targ}. In words, the number of beam-induced false counts expected for a given target A is

$$N_{\mathrm{BIFC}} = N_{\mathrm{INVS}}^{graphite} \times \frac{\text{Number of } \gamma\text{-rays scattered inside the detector body for target A}}{\text{Number of } \gamma\text{-rays scattered inside the detector body for graphite}} . \tag{4.35}$$

If I define N'_{γ} as the number of γ-rays scattered inside the detector volume, then N'_{γ} is

$$N_{\gamma}^{targ\prime} = N_{\gamma}^{targ} \times (1 - \chi_{targ}) \times \kappa_{targ}^{scat}. \tag{4.36}$$

Thus, the final expression for calculating $\mathrm{N}_{\mathrm{BIFC}}$ is

$$N_{\mathrm{BIFC}} = N_{\mathrm{INVS}}^{graphite} \times \frac{N_{\gamma}^{targ}}{N_{\gamma}^{graphite}} \times \frac{(1 - \chi_{targ})}{(1 - \chi_{graphite})} \times \frac{\kappa_{targ}^{scat}}{\kappa_{graphite}^{scat}}. \tag{4.37}$$

Figure 4.2 shows that $\mathrm{N}_{\mathrm{INVS}}/\mathrm{N}_{\gamma}$ for graphite is generally constant over the range 1.5 MeV $\leq \mathrm{E}_{\gamma} \leq$ 5.2 MeV. It will be shown that $\mathrm{N}_{\mathrm{BIFC}}$ may be approximated

$$N_{\mathrm{BIFC}} \approx 2.1 \times 10^{-6} \times N_{\gamma}^{targ} \times \frac{(1 - \chi_{targ})}{(1 - \chi_{graphite})}, \tag{4.38}$$

where the value $2.1{\times}10^{-6}$ is the value of $\mathrm{N}_{\mathrm{INVS}}/\mathrm{N}_{\gamma}$ for graphite, and the other terms in Eq. 4.37 are small corrections to Eq. 4.38.

The parameter $\mathrm{N}_{\mathrm{BIFC}}$ is most often $\leq 1\%$ of $\mathrm{N}_{\mathrm{INVS}}$ for a given run, and so even relatively large uncertainties in $\mathrm{N}_{\mathrm{BIFC}}$ contribute little to the total uncertainty. The $\kappa_{scat}^{targ}/\kappa_{scat}^{graphite}$ term is at most a 1% (4%) correction to $\mathrm{N}_{\mathrm{BIFC}}$ for ^{9}Be ($\mathrm{D_2O}$) for 1.5 MeV $\leq \mathrm{E}_{\gamma} \leq$ 5.2 MeV [Hub89], and so it is disregarded.

Consider the situation where $\mathrm{N}_{\mathrm{INVS}}$ is 10,000 counts, $\mathrm{N}_{\mathrm{BIFC}}$ is 500 counts (5%), and the relative uncertainty of $\mathrm{N}_{\mathrm{BIFC}}$ is 20% or 100 counts. If N'$_n$ is defined as $\mathrm{N}_{\mathrm{INVS}}$ - $\mathrm{N}_{\mathrm{BIFC}}$, then

$$N'_n = 9500, \tag{4.39}$$

and

$$U_{N'_n} = \sqrt{U^2_{N_{\mathrm{INVS}}} + U^2_{N_{\mathrm{BIFC}}}} \approx 141, \tag{4.40}$$

making the relative uncertainty in N'_n of 1.5% compared to the relative uncertainty of $\mathrm{N}_{\mathrm{INVS}}$ of 1%. This scenario represents the largest contribution to $\mathrm{N}_{\mathrm{BIFC}}$ expected given the present data. The assignment of uncertainty for $\sigma_{[^{2}\mathrm{H}(\gamma,n)^{1}\mathrm{H}]}$ is 1% in accordance with the findings of Ref. [Sch05], and the uncertainties of $\mathrm{N}_{\mathrm{INVS}}$, N_{γ}, and N_t/A have already been discussed. The uncertainties for ϵ_n, and N_n are summed up in Table 4.12.

Finally, all uncertainties mentioned here are put into one final table and combined to give

parameter	Relative stat. unc.	Relative syst. unc.
N_{INVS}	1.0%	0%
N_{BIFC}	~20%	0%
$N'_n = N_{INVS}$ - N_{BIFC}	≤1.5%	0%
N_γ	2.1%	3.0%
N_t/A	0.2%	< 1.0%
$\sigma_{[^2H(\gamma,n)^1H]}$	0.0%	1.0%
ϵ_n	2.4%	3.3%
N_n	2.4%	3.3%

Table 4.12: Table of parameters for N_n.

parameter	Relative stat. unc.	Relative syst. unc.
N_n	2.4%	3.3%
N_γ	2.1%	3.0%
N_t/A	0.2%	< 1.0%
σ	3.2%	4.6%

Table 4.13: Table uncertainties associated with σ.

the uncertainty for total cross section measurements, $\sigma_{\gamma,n}$.

5 Data Analysis

5.1 Introduction

To interpret an accurate $\langle\alpha\alpha n\rangle$ rate, one must understand both the forward ($^9\mathrm{Be} + \gamma \rightarrow {}^8\mathrm{Be} + n$) and reverse ($^8\mathrm{Be} + n \rightarrow {}^9\mathrm{Be} + \gamma$) directions for the reaction studied, as well as the influence of nearby channels. Our laboratory measurement is primarily the $^9\mathrm{Be} + \gamma \rightarrow {}^8\mathrm{Be} + n$ reaction. Two observations point to this as the primary channel. Measurements of the $^9\mathrm{Be}(\gamma, n\alpha)\alpha$ three-body reaction in the energy range 1.573 MeV < E_γ < 1.6654 MeV have yielded an upper limit to the total cross-section of 93 nb [Alb04]. Just above the two-body threshold at 1.6654 MeV, the cross section rapidly rises to over 1 mb. This rapid rise corresponds to the broad $1/2^+$ resonance whose peak is < 100 keV above the two-body threshold. A ^{9}Be nucleus excited to the $1/2^+$ level at threshold decays essentially entirely to ^{8}Be in the ground state plus a neutron. Thus, the $1/2^+$ threshold resonance is *the* largest contributor to the $\langle\alpha\alpha n\rangle$ rate.

5.2 History of $\langle\alpha\alpha n\rangle$ Rate Calculations

For several years prior to 1999, the $\langle\alpha\alpha n\rangle$ rate used in reaction network codes was the product of Ref. [Cau88], which considered resonant-only decays of $^9\mathrm{Be} + \gamma \rightarrow {}^8\mathrm{Be} + n$. In other words, when considering the $^8\mathrm{Be} + n \rightarrow {}^9\mathrm{Be} + \gamma$ direction for the reaction, consideration of the width of the ground state of ^{8}Be was neglected as a first approximation. The rate published by Ref. [Ang99] (known as NACRE), was the first publication to include an off-resonant contribution to the $\langle\alpha\alpha n\rangle$ rate. Other works [Sum02, Bur10] have since been carried out and have all followed the formalism used by NACRE. The authors of Ref. [Sum02] and [Bur10] point out that the off-resonant contribution, observed at the lowest temperatures, comes largely from the tails of broad, higher-lying resonances in ^{9}Be ($5/2^+$ and $1/2^-$). It will be shown here that contributions from higher resonances are inflated because of an improper

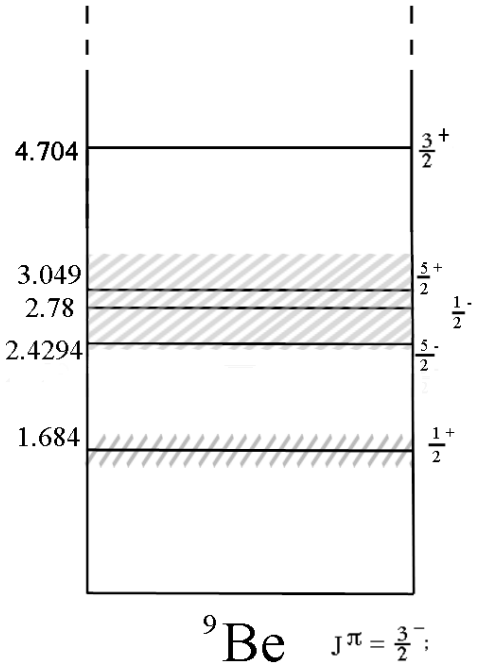

Figure 5.1: Energy levels of ^{9}Be. Image adapted from [Til04].

treatment near threshold.

5.3 Behavior near Threshold

Measurements of the $^9\mathrm{Be}(\gamma, n)^8\mathrm{Be}$ cross-section demonstrate the energy-dependence of the neutron partial width for the resonance at threshold. Any resonance close to threshold experiences a distortion of the normal Breit-Wigner (BW) shape. The neutron partial width, Γ_n, is generally written [Bla52]

$$\Gamma_n = 2\gamma^2 P_\ell \tag{5.1}$$

where γ^2 is a reduced width, and P_ℓ is the penetration factor or penetrability. The reduced width incorporates all of the unknown parts of the nuclear interior, while the penetrability is completely determined by the conditions outside of the nucleus [Ili07]. The penetrability may be generally written

$$P_\ell = \mathrm{R}\left(\frac{k}{\mathrm{F}_\ell^2 + \mathrm{G}_\ell^2}\right) \tag{5.2}$$

where R is the channel radius, k is the wave number and ℓ is the angular momentum of the incoming neutron. For neutrons, the factors F_ℓ and G_ℓ are spherical Bessel (j_ℓ) and Neumann (n_ℓ) functions which are

$$F_\ell = (kr) j_\ell(kr) \tag{5.3}$$

and

$$G_\ell = (kr)n_\ell(kr), \tag{5.4}$$

which depend on angular momentum. These expressions can be written analytically for zero and non-zero values of ℓ in the following way:

$$P_0 = \quad kR \quad = \sqrt{\xi E_n}, \tag{5.5}$$

$$P_1 = \quad \frac{(\xi E_n)^{3/2}}{1+\xi E_n}, \tag{5.6}$$

$$P_2 = \quad \frac{(\xi E_n)^{5/2}}{9+3\xi E_n+(\xi E_n)^2}, \tag{5.7}$$

$$P_3 = \frac{(\xi E_n)^{7/2}}{225+45\xi E_n+6(\xi E_n)^2+(\xi E_n)^3}, \tag{5.8}$$

where ξ is defined as

$$\xi \equiv \frac{2\mu R^2}{\hbar^2} = \frac{(kR)^2}{E_n}. \tag{5.9}$$

Channel radius is often defined [Ili07] as

$$R = r_0(A_t^{1/3} + A_p^{1/3}), \tag{5.10}$$

with $A_{t,p}$ being the nucleon numbers of the target and projectile, and r_0 being on the order of 1.0 to 1.5 fm. References [Ang99, Sum02], whose works I am following closely here, chose $r_0 = 1.4$ fm and 1.44 fm respectively.

Looking back at Eqs. 5.5 to 5.8, observe that the neutron partial width for a (γ, n) reaction generally obeys

$$\Gamma_n \propto E_n^{\ell+1/2}. \tag{5.11}$$

For the reverse, or (n, γ) reaction, the neutron partial width obeys

$$\Gamma_n \propto E_n^{\ell-1/2}, \tag{5.12}$$

as a result of the application of the reciprocity theorem (see Sect. 5.6). For s-wave neutrons, ℓ=0 and the observed neutron partial widths for (γ, n) and (n, γ) reactions are proportional to $E_n^{1/2}$, and $E_n^{-1/2}$ respectively, which is the so-called 1/v law for neutron capture.

It is obvious that one must attribute this energy-dependence to the $1/2^+$ threshold resonance to obtain a good fit to ^{9}Be$(\gamma, n)^8$Be cross-section data. However, previous works have not applied this energy-dependence to the tails from the broad, higher-lying states in ^{9}Be.

Possible Values L_{photon}	$^9Be_{g.s}$ $\vec{j}_{g.s}$	J^π	Possible χ_λ	$^8Be_{g.s}$+n $\vec{j}_{g.s}+\vec{s}_n$	Allowed $\ell_{neutron}$
1,2	$3/2^-$	$1/2^+$	E1, M2	$1/2^+$	0, ~~1~~
1,2,3,4	$3/2^-$	$5/2^-$	M1, E2, M3, E4	$1/2^+$	~~2~~, 3
1,2	$3/2^-$	$1/2^-$	M1, E2	$1/2^+$	~~0~~, 1
1,2,3,4	$3/2^-$	$5/2^+$	E1, M2, E3, M4	$1/2^+$	2, ~~3~~
1,2,3	$3/2^-$	$3/2^+$	E1, M2, E3	$1/2^+$	~~1~~, 2

Table 5.1: The possible couplings of excited states in ^{9}Be with ^{8}Be in the ground state plus a neutron are shown. When measuring the $^9Be + \gamma \rightarrow {}^8Be + n$ reaction in the laboratory, the photon angular momentum, L_{photon}, ≡ 1. However, when considering the $^8Be + n \rightarrow {}^9Be + \gamma$ reaction, L_{photon} is not restricted. Parity considerations prohibit certain values of $\ell_{neutron}$ which have been crossed out.

The result of this incomplete treatment has been to inflate the off-resonance contribution by as much as a factor of four. Table 5.1 shows all of the possible L_{photon} and $\ell_{neutron}$ combinations for coupling an excited state of ^{9}Be with ^{8}Be in the ground state plus a neutron. When the parity of each excited state in ^{9}Be is considered, certain values of $\ell_{neutron}$ are excluded. The value of ℓ determines the form of the penetrability, P_ℓ (Eqs. 5.5 to 5.8) which determines the form for the neutron partial width (Eq. 5.1) of the excited state in ^{9}Be, and ultimately the behavior of the tail of the partial width near the threshold. Table 5.2 is a similar table which considers couplings between excited states of ^{9}Be and the first excited state in ^{8}Be plus a neutron.

When a level of spin J is isolated from other levels with the same spin and parity, a one-level R-matrix approximation may be used to describe the contribution of the level to the (γ, n) cross-section. This takes the form of the Breit-Wigner equation (BWE) for an isolated resonance [Ili07]:

$$\sigma_{BW}(E) = \frac{\pi}{k^2}\frac{(2J+1)(1+\delta_{01})}{(2j_0+1)(2j_1+1)}\frac{\Gamma_a\Gamma_b}{(E-E_R)^2+\frac{1}{4}\Gamma^2}, \tag{5.13}$$

where k is the wave number of the projectile, j_0, j_1 and J are the spins of the target, projectile and resonance respectively, E_R is the resonance energy, $\Gamma_{a,b}$ is the partial width for entrance or exit channel a, b, and Γ is the total width. The $(1+\delta_{01})$ term accounts for identical particle interactions such as $\alpha + \alpha$ scattering. For a (γ, n) reaction the BWE takes the form

$$\sigma_{\gamma,n}(E_\gamma) = \frac{\pi}{k_\gamma^2}\frac{2J+1}{2(2I+1)}\frac{\Gamma_\gamma\Gamma_n}{(E_\gamma-E_R)^2+\frac{1}{4}\Gamma^2}. \tag{5.14}$$

In the present analysis, energy dependence is introduced for all but the $5/2^-$ resonance. Justifications for excluding energy dependence for the $5/2^-$ state are discussed in the next section.

Possible Values L_{photon}	$^9Be_{g.s}$ $\vec{j}_{g.s}$	J^π	Possible χ_λ	$^8Be^*_{2+}$+n $\vec{j}_{2+}+\vec{s}_n$	Allowed $\ell_{neutron}$
1,2	$3/2^-$	$1/2^+$	E1, M2	$3/2^+$, $5/2^+$	~~1~~, 2, ~~3~~
1,2,3,4	$3/2^-$	$5/2^-$	M1, E2, M3, E4	$3/2^+$, $5/2^+$	~~0~~, 1, ~~2~~, 3, ~~4~~, 5
1,2	$3/2^-$	$1/2^-$	M1, E2	$3/2^+$, $5/2^+$	1, ~~2~~, 3
1,2,3,4	$3/2^-$	$5/2^+$	E1, M2, E3, M4	$3/2^+$, $5/2^+$	0, ~~1~~, 2, ~~3~~, 4, ~~5~~
1,2,3	$3/2^-$	$3/2^+$	E1, M2, E3	$3/2^+$, $5/2^+$	0, ~~1~~, 2, ~~3~~, 4

Table 5.2: Same as the Table (5.1) above, but now I consider decay to the first excited state in ^{8}Be. All states in ^{8}Be, including the ground state, have an associated width, and therefore, decays to excited states should be considered. Lowest values of $\ell_{neutron}$ are assumed to be the most probable.

For the case of the $1/2^+$ state where $\ell = 0$, Eq. 5.1 and Eq. 5.5 may be combined so that the neutron partial width may be written

$$\Gamma_n = 2\sqrt{\epsilon(E_\gamma - S_n)} = 2\sqrt{\epsilon E_n}, \tag{5.15}$$

where S_n is the neutron separation energy of 1.6654 MeV deduced from the mass difference between ^{9}Be and ^{8}Be plus a neutron, and ϵ contains the reduced partial width for the $1/2^+$ state. Epsilon is defined as

$$\epsilon = \frac{2\mu R^2 \gamma^4}{\hbar^2}, \tag{5.16}$$

where μ is the reduced mass of ^{8}Be plus a neutron, R is the channel radius, and γ^2 is the reduced width. Defining ϵ, which has units of energy, in this way provides a convenient fitting parameter.

The energy-dependent γ-ray partial widths may be cast in terms of reduced transition probabilities [Bla52] for E1 and M1 transitions as

$$\Gamma_\gamma(E1) = \frac{16\pi}{9}\alpha(\hbar c)^{-2}E_\gamma^3 B(E1)\downarrow, \tag{5.17}$$

and

$$\Gamma_\gamma(M1) = \frac{16\pi}{9}\alpha(2M_p c^2)^{-2}E_\gamma^3 B(M1)\downarrow, \tag{5.18}$$

where α is the fine structure constant. Note that the strength of transitions from the ground state to an excited state (B$\uparrow$) is related to the strength of transitions from that excited state to the ground state (B$\downarrow$) by,

$$B\uparrow = \frac{2J_x + 1}{2J_0 + 1} B\downarrow . \tag{5.19}$$

Transitions from the ground state of ^{9}Be ($3/2^-$), to an excited 1/2 or 5/2 state yields factors

of 0.5 and 1.5 in Eq. 5.19 respectively. Since $B\downarrow$ are the transitions used in the calculation of $\langle\alpha\alpha n\rangle$, they will be used exclusively for the rest of this thesis. For each resonance, the reduced width, γ^2, (or ϵ where applicable), the B(E1)$\downarrow$ or B(M1)$\downarrow$ transition strength, and the resonance energy (E_R) are determined by fitting the data. Table 5.3 displays the parameters determined for each resonance.

The available resolution of the γ-ray beams at HIγS made a determination of Γ_n for the narrow 5/2- state impossible. I adopt the width of Ref. [Til04] for the rate calculation. Because Γ_n is orders of magnitude larger than Γ_γ, the approximation that the total width, Γ, is equal to the neutron partial width may be made. The $1/2^+$ resonance then has the form

$$\sigma(\gamma,n)_{1/2^+} = \frac{8\pi^2}{9}\alpha\frac{E_\gamma B(E1)_{1/2^+}\sqrt{\epsilon_{1/2^+}E_n}}{(E_\gamma - E_R^{1/2^+})^2 + \epsilon_{1/2^+}E_n}. \tag{5.20}$$

In general, each resonance has the form,

$$\sigma(\gamma,n)_j = (2j+1)\frac{2\pi^2}{9}\alpha\frac{E_\gamma B(E1,M1)^j\Gamma_n^j}{(E_\gamma - E_R^j)^2 + \frac{1}{4}{\Gamma_n^j}^2}. \tag{5.21}$$

5.4 Fitting Techniques

The data are divided into four groups:

1. January Absolute Data (2.5 MeV $\leq$ E_γ $\leq$ 5.2 MeV),
2. January Normalized Data (2.5 MeV $\leq$ E_γ $\leq$ 5.2 MeV),
3. July Absolute Data (1.5 MeV $\leq$ E_γ $\leq$ 3.2 MeV),
4. July Normalized Data (2.4 MeV $\leq$ E_γ $\leq$ 3.2 MeV).

The absolute data are determined using Eq. 4.17 and the normalized data are determined using Eq. 4.18. The normalized data are only valid for E_γ >2.225 MeV. Equation 4.18 was only used for data with E_γ >2.4 MeV where the calculations of the $^2H(\gamma,n)^1H$ cross-section are nearly model independent. The general approach for fitting the data is as follows:

- Exclude cross-section data within 2.387 MeV $\leq$ E_γ $\leq$ 2.559 MeV,
- Fit the data with an equation which is a sum of five B.W.E.s, each having correct energy dependence.

The data over the $5/2^-$ narrow resonance at 2.431 MeV are excluded in this discussion of fitting because the resonance is known to have narrower structure than the experiment could resolve. (The treatment of the narrow $5/2^-$ resonance is described in the next section.) Of

the five resonances being fit ($1/2^+$, $1/2^-$, $5/2^+$, $3/2^+$, $3/2^-$) the lowest three ($1/2^+$, $1/2^-$, $5/2^+$) may contribute to the $\langle\alpha\alpha n\rangle$ rate while the two highest ($3/2^+$, $3/2^-$) will not likely contribute. However, the low energy tails of these resonances should be included in the fit to account for any strength that they contribute to the cross-section at low energies.

I used two approaches to interpret the data. The first approach was to attempt a fit to all of the absolute data from January and July together. My second approach was to attempt to fit each of the four data groups listed above separately. It was expected that the resulting fits would be very similar.

Notice that the January data sets (1 and 2) cover the range 2.5 MeV $\leq$ E_γ $\leq$ 5.2 MeV and thus the include the $1/2^-$, $5/2^+$, $3/2^+$ and $3/2^-$ resonances. Data set 3 (July Absolute) covers 1.5 MeV $\leq$ E_γ $\leq$ 3.2 MeV and thus includes the $1/2^+$, $1/2^-$ and $5/2^+$ states, while set 4 (July Normalized) covers only 2.4 MeV $\leq$ E_γ $\leq$ 3.2 MeV and so only includes the $1/2^-$ and $5/2^+$ states. Since data set 3 was the only set to cover the range E_γ < 2.4 MeV, it was the only data set to which parameters of the $1/2^+$ state could be fit. The values obtained from data set 3 became fixed parameters when fitting data sets 1, 2 and 4. Likewise, data sets 1 and 2 are the only sets to cover E_γ > 3.2 MeV, and thus are the only sets able to determine parameters for the $3/2^+$ and $3/2^-$ resonances. In this case, the parameters obtained for the $3/2^+$ and $3/2^-$ resonances from data sets 1 and 2 were averaged, and these average values became fixed parameters in data sets 3 and 4. Averaged parameters very closely resemble global parameters. However, by fitting each set separately, I may more accurately establish uncertainty in the fit.

Linear and log-scale plots of the fits to data are shown in Figs. 5.2, 5.3, 5.4, 5.5, 5.6 and 5.7. It was observed that in the region of overlap (2.5 MeV $\leq$ E_γ $\leq$ 3.2 MeV) between the January and July data sets that the data begin to diverge at $E_\gamma = 2.9$ MeV. Investigations into the cause of this divergence were thorough. Recall the following facts:

1. *Molly* detector efficiency was verified with simulations;

2. The INVS detector efficiency was verified with simulations to within a normalization of a few percent;

3. Gamma-ray beam attenuation was measured through the targets giving agreement with actual target thickness to within 5%;

4. Attenuation though Pb was measured with two independent instruments giving similar results;

5. Both absolute and normalized cross-section data are nearly identical where they exist;

6. Agreement between January and July data is strong for E_γ< 2.9 MeV

Table 5.3: Resonance parameters from the present work. Branching ratios (BR) taken from Ref. [Til04].

J^π	χ_λ	E_R [MeV]	$B(\chi_\lambda)$ E1→[e^2fm^2], M1 → $[(\frac{e\hbar}{2Mc})^2]$	Γ_γ [eV]	Γ_n [keV]	BR (%)
$1/2^+$	E1	1.7387 ± 0.0008	0.1355 ± 0.0014	0.745 ± 0.008	226 ± 3	100
$5/2^-$	M1	2.431 ± 0.004	0.587 ± 0.027	0.098 ± 0.004	– †	7
$1/2^-$	M1	2.84 ± 0.03	4.6 ± 0.8	1.23 ± 0.16	386 ± 35	100
$5/2^+$	E1	3.00 ± 0.01	0.020 ± 0.003	0.58 ± 0.05	212 ± 15	87
$3/2^+$	E1	4.704[a]	0.0605 ± 0.0035	6.6 ± 0.4	1680 ± 50	0
$3/2^-$	M1	5.59[a]	6.8 ± 0.5	13.7 ± 1.3	360 ± 40	0

† This value could not be obtained using the present data.

[a] This value was fixed in accordance with Ref. [Til04].

It is known that the distribution of γ-ray energies was significantly different between January and July. However, estimates of the effect of this difference to the cross-section were not found to be a sufficient explanation. The location of this divergence in the data has the largest effect on the $5/2^+$ state. The uncertainty of the parameters for this state and the $1/2^-$ state are adjusted to reflect these findings. It will be shown that the effect of these resonances on the $\langle\alpha\alpha n\rangle$ rate is nearly negligible. The equation used to fit the data, and a table of the parameters derived are recorded in Sect. 7.3.

5.5 Narrow Resonance Treatment

The $5/2^-$ resonance is a special case, because the resonance is too narrow to deduce the BW parameters with a fit to the data. In the case of narrow resonances, however, a "trick" may be employed to deduce Γ_γ by integrating the cross section. For this to work, (1) the resonance must be sufficiently isolated from other resonances, (2) the neutron and gamma partial widths must be small enough to be considered energy independent, and (3) the neutron partial width must be larger than the gamma partial width, such $\Gamma_n \approx \Gamma$. With these three conditions satisfied, Eq. 5.14 may be integrated for the resonance in question over all energies as follows:

$$\int_0^\infty \sigma_{\gamma,n}(E_\gamma)dE_\gamma = \frac{\pi}{k_\gamma^2}\frac{2J+1}{2(2I+1)}\frac{\Gamma_\gamma\Gamma_n}{\Gamma}2\int_0^\infty \frac{\Gamma/2\ dE_\gamma}{(E_\gamma - E_R)^2 + \frac{1}{4}\Gamma^2}, \tag{5.22}$$

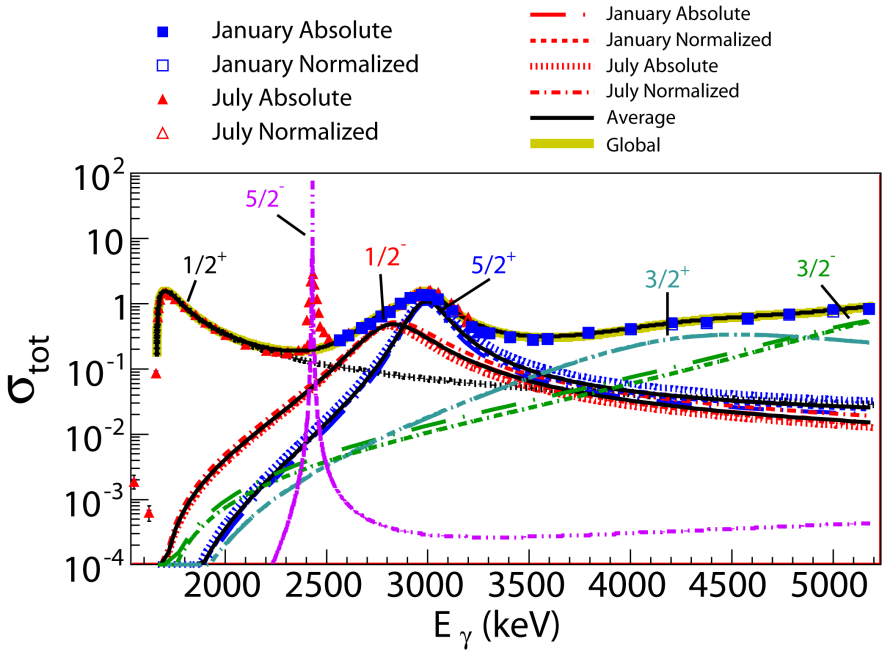

Figure 5.2: The present data with BW fits shown. A different line style is used for each data set (see legend) while different states in ^{9}Be are color-coded and labeled. The vertical log scale displays the proper energy dependence of each resonance at the threshold (1.6654 MeV). A neutron width from Ref. [Til04] was used for the $5/2^-$ state. The approximation of energy-independence for the $5/2^-$ state is observed to be justified.

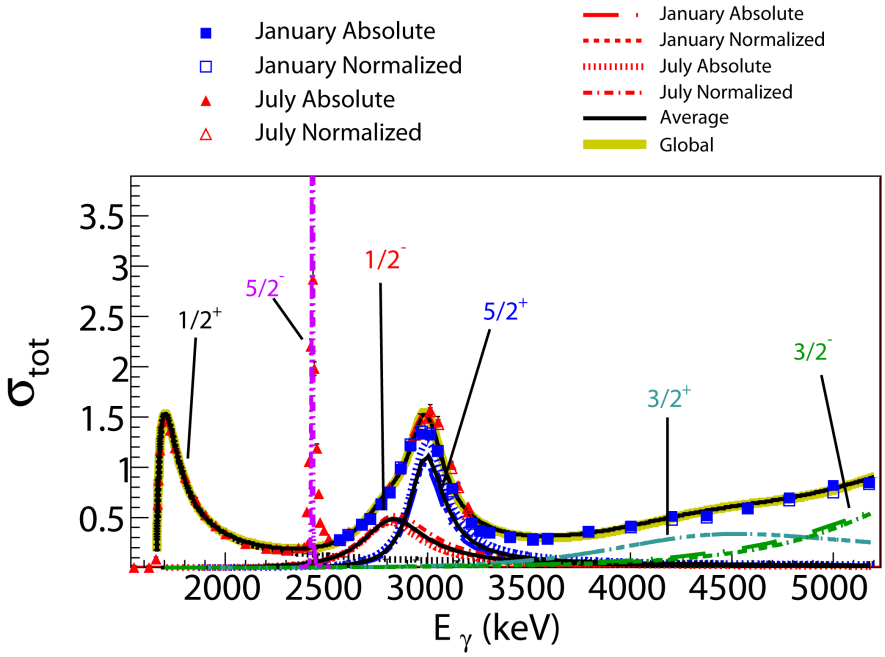

Figure 5.3: The present data on a linear scale. The explanation of the various curves is the same as in Fig. 5.2.

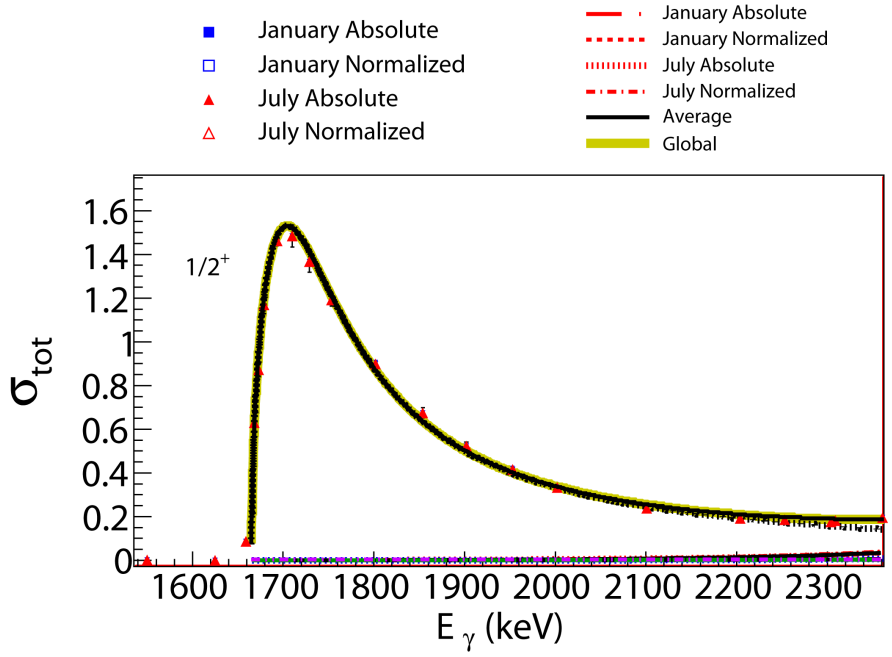

Figure 5.4: The fitted data near the threshold. Only the July Absolute data can be used for this fit. The explanation of the various curves is the same as in Fig. 5.2.

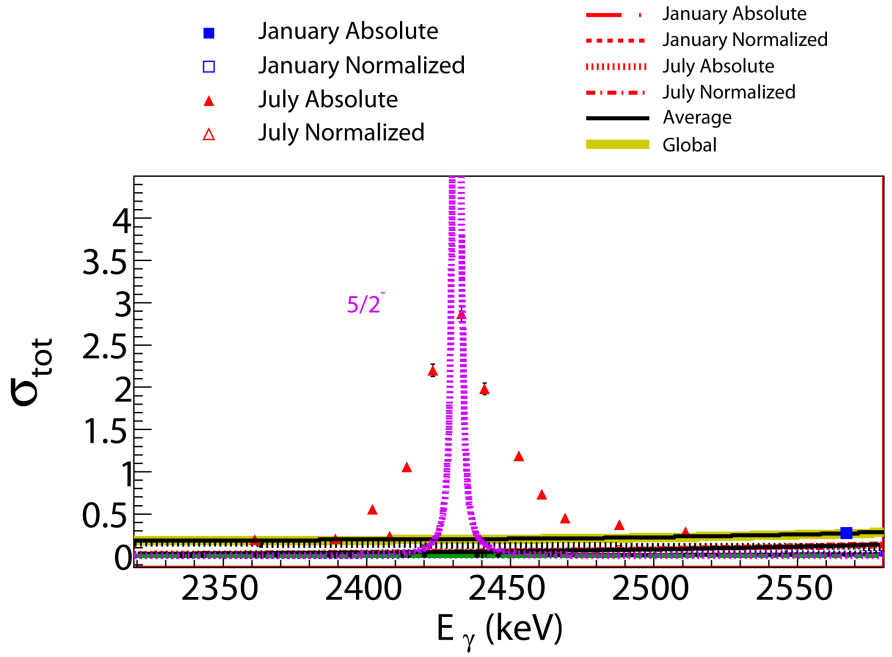

Figure 5.5: Data over the narrow $5/2^-$ resonance. A neutron width from Ref. [Til04] was used here. The explanation of the various curves is the same as in Fig. 5.2.

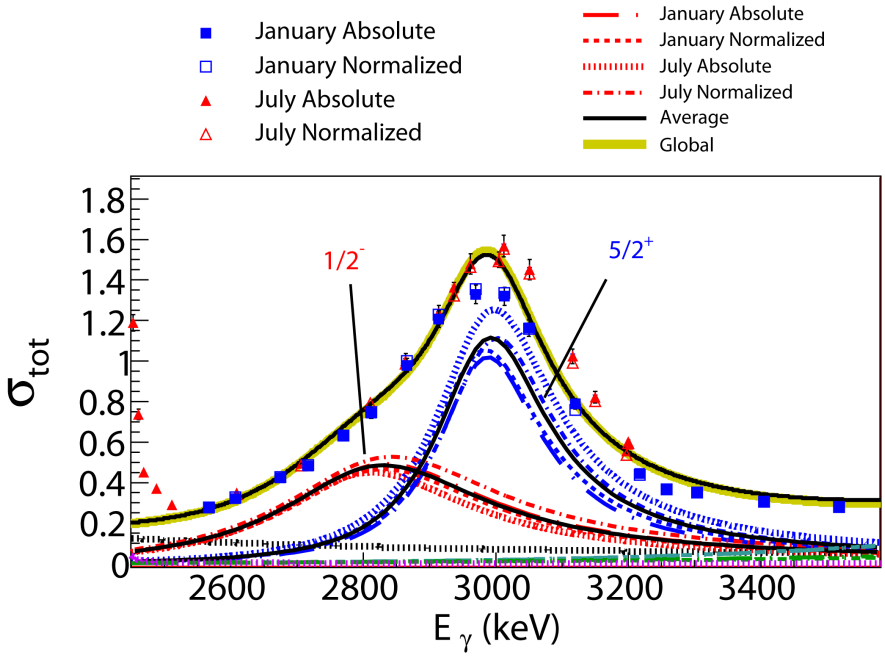

Figure 5.6: The fitted data over the 3 MeV hump. All data sets can be used for these fits. Notice that the averaged fit is very close to the global fit. The explanation of the various curves is the same as in Fig. 5.2.

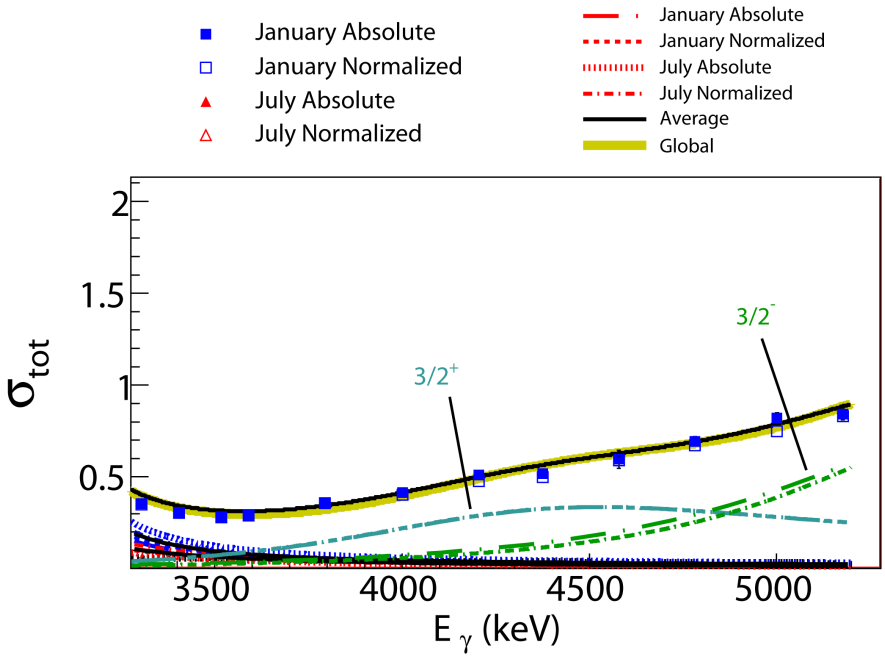

Figure 5.7: The fitted data beyond the 3 MeV hump. Only January data can be used for these fits. The explanation of the various curves is the same as in Fig. 5.2.

where I have taken advantage of condition (2) to pull out and rearrange widths from the integral. The integral on the right hand side may be shown to be equivalent to

$$\int_0^\infty \frac{a\ dx}{a^2+(x-E_R)^2} = \tan^{-1}\left[\frac{x-E_R}{a}\right]\Bigg|_0^\infty \approx \pi. \tag{5.23}$$

Based on assumption (2), -2E$_R$/Γ will be a number large enough to be approximately $-\infty$ when E = zero, but negligible when E = ∞. Thus Eq. 5.22 simplifies to

$$\int_0^\infty \sigma_{\gamma,n}(E_\gamma)dE_\gamma = \frac{\pi}{k_\gamma^2}\frac{2J+1}{2(2I+1)}\frac{\Gamma_\gamma\Gamma_n}{\Gamma}2\pi. \tag{5.24}$$

Now taking advantage of condition (3), inserting the resonance spin J = 5/2 and target spin I = 3/2, and the γ-ray wave number at E$_R$, one arrives at

$$\int_0^\infty \sigma_{\gamma,n}(E_\gamma)dE_\gamma = \frac{3}{2}\left(\frac{\hbar c\pi}{E_R}\right)^2\Gamma_\gamma. \tag{5.25}$$

5.6 Reciprocity Theorem

I now turn to the reciprocity theorem to transform the ^{9}Be$(\gamma,n)^8$Be cross-section into the ^{8}Be$(n,\gamma)^9$Be cross-section. The reciprocity theorem [Ili07] relates the cross section of a reaction to its inverse reaction based on the notion of invariance under time-reversal. The reciprocity theorem for deriving ^{8}Be + n $\rightarrow$ ^{9}Be + γ from ^{9}Be + γ $\rightarrow$ ^{8}Be + n is

$$\sigma_{^8Be+n\ \rightarrow\ ^9Be+\gamma} = \frac{2(2j_{^9Be}+1)}{(2j_{^8Be}+1)(2j_n+1)}\frac{k_\gamma^2}{k_n^2}\sigma_{^9Be+\gamma\ \rightarrow\ ^8Be+n}, \tag{5.26}$$

where

$$k_\gamma^2 = \left(\frac{E_\gamma}{\hbar c}\right)^2 \tag{5.27}$$

and

$$k_n^2 = \frac{2\mu E_n}{\hbar^2}. \tag{5.28}$$

The ground state spins for ^{9}Be, ^{8}Be and a neutron are 3/2, 0, and 1/2, respectively. I will designate the spin weighting factor for the forward reaction as g and note that g = 4. The γ-ray energy is related to the neutron energy by S$_n$ via

$$E_n = E_\gamma - S_n. \tag{5.29}$$

And finally, the ratio of wave numbers is

$$\frac{k_\gamma^2}{k_n^2} = \frac{E_\gamma^2}{2\mu c^2 E_n}. \tag{5.30}$$

For the special case of the $1/2^+$ resonance, where $\ell = 0$, this makes

$$\sigma_{8Be+n} = \frac{16\pi^2}{9\mu c^2}\alpha\frac{E_\gamma^3 B_j(E1,M1)\,(\epsilon_j/E_n)^{1/2}}{(E_\gamma - E_R^j)^2 + \epsilon_j E_n} \tag{5.31}$$

or, put in a form which uses Γ_n and Γ_γ,

$$\sigma_{8Be+n} = \frac{\pi(\hbar c)^2}{2\mu E_n}\sqrt{\frac{E_n}{E_R^{1/2^+} - S_n}}\left(\frac{E_\gamma}{E_R^{1/2^+}}\right)^3 \frac{\Gamma_\gamma^{1/2^+}\Gamma_n^{1/2^+}}{\left(E_\gamma - E_R^{1/2^+}\right)^2 + \Gamma_n^{1/2^+2}} \tag{5.32}$$

where the terms

$$\sqrt{\frac{E_n}{E_R^{1/2^+} - S_n}}, \tag{5.33}$$

and

$$\left(\frac{E_\gamma}{E_R^{1/2^+}}\right)^3 \tag{5.34}$$

give explicit energy dependence to Γ_n and Γ_γ, respectively. The calculations for higher lying resonances are more complicated, and have different energy dependence at the threshold. However, the methods for calculating the partial widths are mostly similar.

5.7 General Rate Calculation

Having derived the cross-section for the reverse reaction, I proceed to calculate the astrophysical reaction rate. The derivation of astrophysical reaction rates has been described in detail in Ref. [Ili07], so I will provide a brief summary here. A reaction rate is generally the frequency with which a reaction will occur given a known number of constituent nuclei to react, and a known velocity distribution of the nuclei. The probability of reaction is, of course, the cross-section, and the velocity distribution for stellar environments may be modeled as a Maxwell-Boltzmann distribution at some temperature. The probability that a two particles with reduced mass, μ, have relative velocity between v and $v + dv$ for a given temperature, T, is

$$P(v)dv = \left(\frac{\mu}{2\pi k_b T}\right)^{\frac{3}{2}} \exp\left[\frac{-\mu v^2}{2k_b T}\right] 4\pi v^2 dv, \tag{5.35}$$

where k_b is Boltzmann's constant. Assuming non-relativistic particle behavior, $E = \mu v^2/2$, and $dE/dv = \mu v$. Making this substitution yields

$$P(E)dE = 2\left(\frac{E}{\pi}\right)^{\frac{1}{2}}\left(\frac{1}{k_b T}\right)^{\frac{3}{2}} \exp\left[\frac{-E}{k_b T}\right] dE, \tag{5.36}$$

which has a maximum at E = $k_bT/2$. The rate, $\langle\sigma v\rangle$, is then the sum over all particle velocities weighted by the energy dependent cross-section and velocity distribution, or

$$\langle\sigma v\rangle = \left(\frac{8}{\pi\mu}\right)^{\frac{1}{2}}\left(\frac{1}{k_bT}\right)^{\frac{3}{2}}\int_0^\infty \sigma(E)\exp\left[\frac{-E}{k_bT}\right]EdE. \tag{5.37}$$

Equation 5.37 is the correct form for a two-body reaction. However, in the present work I need to compute the rate for two sequential reactions, and thus need to expand our ideas. A more correct form for calculating the rate of formation of ^{9}Be comes from constructing a double integral which first calculates the rate of formation of ^{8}Be from the $\alpha + \alpha$ scattering cross-sections. The formalism of Ref. [Nom85] was developed for calculating the on and off-resonant formation of ^{12}C via the triple-α reaction, and was first modified to calculate the rate of formation of ^{9}Be for the NACRE compilation. A brief summary for the calculation of the formation of ^{8}Be follows.

Consider the case of astrophysical reactions at relatively low temperatures (e.g., < 0.025 GK). As discussed previously, the most probable energy for a system of particles at a given temperature, T, is $E_{most\ likely} = k_bT/2$. In the case of $\alpha + \alpha$ scattering, the resonance energy, E_R, for formation of ^{8}Be is 92.12 keV. Equating E_R with $E_{most\ likely}$ suggests that the optimal temperature for forming ^{8}Be is approximately 2.1 GK, which is ~100 times larger than the temperatures under consideration. At 0.025 GK and below, the low-energy tail of the ^{8}Be ground state resonance will be the primary mechanism for forming ^{8}Be and, ultimately, ^{9}Be.

The cross-section for $\alpha + \alpha$ may be constructed using the astrophysical S-factor, defined as [Ili07]

$$\sigma_{\alpha\alpha}(E) = S_{\alpha\alpha}(E)\frac{1}{E}\exp\left[-(2\pi\eta)\right], \tag{5.38}$$

where η is the Sommerfeld parameter, defined as

$$2\pi\eta = \left(\frac{E_G}{E}\right)^{1/2} = \sqrt{\frac{(\pi\alpha Z_A Z_B)^2 2\mu_{AB}c^2}{E}}, \tag{5.39}$$

where E_G is the Gamow energy which depends on the fine structure constant, α, the proton number, Z, of nuclei A and B, and the reduced mass of the A + B system, μ_{AB}. For $\alpha + \alpha$ I find,

$$E_G = (4\pi\alpha)^2 m_\alpha c^2 \approx 31.4\ MeV. \tag{5.40}$$

Recalling Eq. 5.13, $S_{\alpha\alpha}$(E) takes the form

$$S_{\alpha\alpha}(E) = E\frac{\pi}{k_\alpha^2}\frac{(2J+1)(1+\delta_{01})}{(2j_0+1)(2j_1+1)}\frac{\Gamma_{\alpha1}(E)\Gamma_{\alpha2}(E)}{(E-E_R)+\frac{1}{4}\Gamma^2}\exp\left[\left(\frac{E_G}{E}\right)^{1/2}\right], \tag{5.41}$$

with wave number

$$k_\alpha^2 = \frac{2\mu_{\alpha\alpha}E}{\hbar^2}, \tag{5.42}$$

All spins (J, j_0 and j_1) are zero and δ_{01} is 1 rendering

$$S_{\alpha\alpha}(E) = \frac{\pi\hbar^2}{\mu_{\alpha\alpha}} \frac{\Gamma_{\alpha 1}(E)\Gamma_{\alpha 2}(E)}{(E-E_R)+\frac{1}{4}\Gamma^2} \exp\left[\left(\frac{E_G}{E}\right)^{1/2}\right]. \tag{5.43}$$

Furthermore,

$$\Gamma_{\alpha 1}(E) = \Gamma_{\alpha 1}(E_R)\frac{P_\ell(E)}{P_\ell(E_R)}, \tag{5.44}$$

and

$$\Gamma_{\alpha 2}(E) = \Gamma_{\alpha 2}(E_R)\frac{P_\ell(Q+E)}{P_\ell(Q+E_R)}. \tag{5.45}$$

The authors of Ref. [Nom85] indicate that the effect of the Q value in Eq. 5.45 often acts to lessen the energy dependence from the penetrabilities for the exit channel, rendering $\Gamma_{\alpha 2}(E)=\Gamma_{\alpha 2}(E_R)$. I have adopted the methods of Ref. [Nom85], in which Eq. 5.45 cancels out of the formula for the $\langle\alpha\alpha n\rangle$ calculation.

5.8 $\langle\alpha\alpha n\rangle$ Rate Calculation

I assumed a two-step process following the work of Ref. [Ang99]. First, two α-particles interact with center-of-mass (CoM) energy, E, to form ^{8}Be. Subsequently, the ^{8}Be nucleus interacts with a neutron with new CoM energy E' which is relative to E. The differential rate of formation of ^{8}Be is computed to be [Nom85]

$$\frac{d\langle\alpha\alpha\rangle}{dE} = \frac{\langle\alpha\alpha\rangle}{\Gamma_\alpha(^8Be,E)}. \tag{5.46}$$

As previously indicated, the denominator of $\partial\langle\alpha\alpha\rangle$ will cancel with $\Gamma_{\alpha 2}$(E).

In essence, $\langle\alpha\alpha n\rangle$ is computed for on-resonance and off-resonance contributions by evaluating $\langle n^8Be\rangle$ at every step of a sum over $\partial\langle\alpha\alpha\rangle\times\langle n^8Be\rangle$. The full equation has the form

$$N_A^2\langle\sigma v\rangle^{\alpha\alpha n} = N_A\left(\frac{8\pi\hbar}{\mu_{\alpha\alpha}^2}\right)\left(\frac{\mu_{\alpha\alpha}}{2\pi k_bT}\right)^{3/2}$$
$$\times\int_0^\infty \frac{\sigma_{\alpha\alpha}(E)}{\Gamma_\alpha(^8Be,E)}\exp(-E/k_bT)N_A\langle\sigma v\rangle^{n^8Be}EdE \tag{5.47}$$

with

$$N_A\langle\sigma v\rangle^{n^8Be} = N_A\left(\frac{8\pi\hbar}{\mu_{n^8Be}^2}\right)\left(\frac{\mu_{n^8Be}}{2\pi k_bT}\right)^{3/2}$$

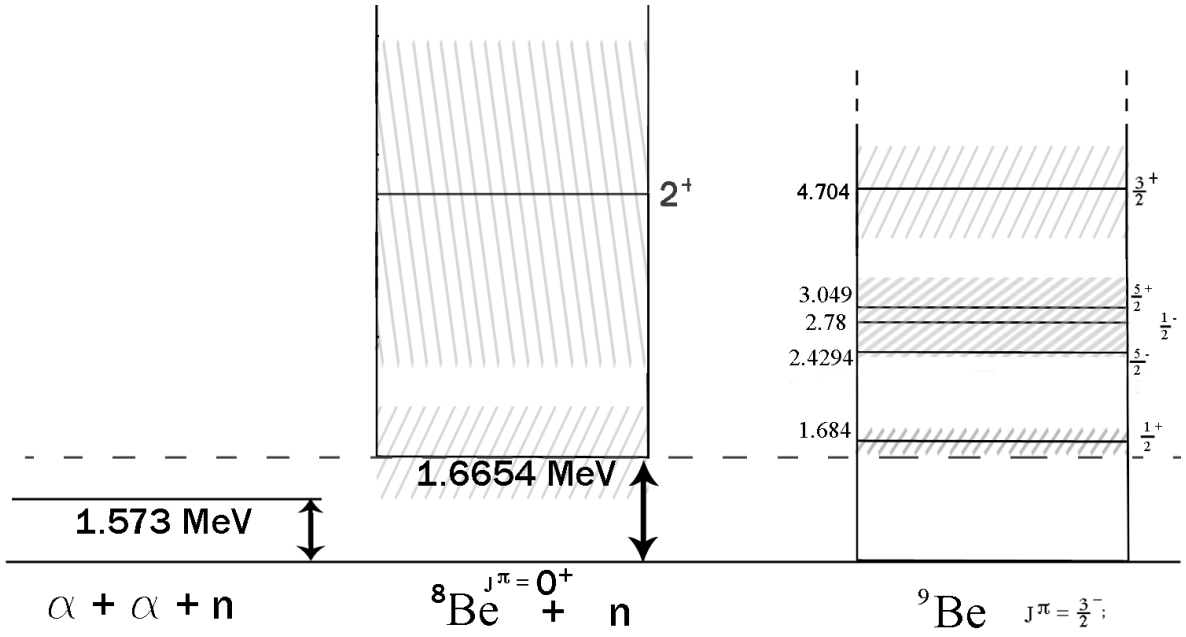

Figure 5.8: A level scheme relating ^{9}Be, ^{8}Be +n, and α + α + n. The neutron separation energy (S_n) for ^{9}Be is shown as a dashed line. In the rate calculation, E is the energy of the two α-particles. The parameter E' is the energy of the ^{8}Be nucleus and the neutron with respect to E. In this scheme, formation of ^{9}Be at $E = E' = 0$ is very unlikely, but not prohibited because of the fact that the ground state of ^{8}Be has finite width.

Table 5.4: A table comparing the present parameters from the first 4 resonances in ^{9}Be with the parameters of other works. Energy-dependent (✓) and energy-independent (⊗) parameters are distinguished.

Param. (Units)	State	Present		NACRE [Ang99]		Sumiyoshi *et al.* [Sum02]		Burda *et al.* [Bur10]	
	$(1/2)^+$	1.7387(8)		1.731		1.735(3)		1.748(6)	
E_R	$(5/2)^-$	2.431(4)		–		2.43		2.4294(13)	
(MeV)	$(1/2)^-$	2.84(3)		2.784(12)		–		2.78(12)	
	$(5/2)^+$	3.00(1)		3.049(9)		3.077(9)		3.049(9)	
	$(1/2)^+$	226(3)	✓	227(15)	✓	225(12)	✓	274(8)	✓
Γ_n	$(5/2)^-$	0.77[a]	⊗	–		0.77[a]	⊗	0.77[a]	⊗
(keV)	$(1/2)^-$	386(35)	✓	1080(110)	⊗	–		1080(110)	⊗
	$(5/2)^+$	212(15)	✓	282(11)	⊗	549(12)	⊗	282(11)	⊗
	$(1/2)^+$	0.745(8)	✓	0.51(10)	✓	0.568(11)	✓	0.302(45)	✓
Γ_γ	$(5/2)^-$	0.098(4)	✓	–		0.049(12)	⊗	0.089(10)	⊗
(eV)	$(1/2)^-$	1.23(16)	✓	0.45(36)	⊗	–		0.45(36)	⊗
	$(5/2)^+$	0.58(5)	✓	0.90(45)	⊗	1.24(2)	⊗	0.90(45)	⊗
B(E1)↓/	$(1/2)^+$	0.135(1)	✓	0.094(20)	✓	0.104(2)	✓	0.054(4)	✓
B(M1)↓	$(5/2)^-$	0.59(3)	✓	–		0.295(72)	⊗	–	
(e^2fm^2)/	$(1/2)^-$	4.6(8)	✓	–		–		–	
(μ_N^2)	$(5/2)^+$	0.020(3)	✓	–		0.0406(7)	⊗	–	

[a] This value was taken from Ref. [Til04].

$$\times \int_0^\infty \sigma_{n^8Be}(E';E)\exp(-E'/k_bT)E'dE' \tag{5.48}$$

following the normal rate formulation given by Eq. 5.37.

Interactions between α-particles do not need to be on-resonance to be followed by a neutron capture event. Off-resonant contributions are difficult to distinguish from 3-body interactions. However, they are treated as sequential two-body reactions and thus access the two-body cross-sections.

Eq. 5.47 is evaluated using the parameters from Table 5.3 and temperatures in the range $0.001 \leq T_9 \leq 10$. Present results are compared with previous works. Other calculations were made to try to reproduce the rates published by three previous works [Ang99, Sum02, Bur10] which revealed differences in how each rate was interpreted. Table 5.4 compares the parameters from each evaluation. Table 5.5 is a table of rates vs. temperature. The computer code used to determine these rates is recorded in Sect. 7.4. The present work is the only one that generated energy-dependent resonance parameters (where possible) for all of the evaluated resonances.

Fig. 5.9 and 5.10 display log and linear-scale representations of the four rates being com-

Table 5.5: A Table of rates vs. T_9 ($\equiv 10^9$ K) from the present parameters.

T_9	$N_A\langle\alpha\alpha n\rangle$	T_9	$N_A\langle\alpha\alpha n\rangle$	T_9	$N_A\langle\alpha\alpha n\rangle$
0.001	1.08E-59	0.04	1.55E-15	0.5	9.61E-07
0.002	9.11E-48	0.05	2.26E-13	0.6	9.52E-07
0.003	5.67E-42	0.06	5.95E-12	0.7	8.96E-07
0.004	2.60E-38	0.07	5.91E-11	0.8	8.21E-07
0.005	1.06E-35	0.08	3.22E-10	0.9	7.42E-07
0.006	1.05E-33	0.09	1.17E-09	1	6.67E-07
0.007	4.13E-32	0.1	3.24E-09	1.25	5.07E-07
0.008	8.64E-31	0.11	7.32E-09	1.5	3.89E-07
0.009	1.14E-29	0.12	1.43E-08	1.75	3.04E-07
0.01	1.05E-28	0.13	2.48E-08	2	2.43E-07
0.011	7.39E-28	0.14	3.94E-08	2.5	1.64E-07
0.012	4.18E-27	0.15	5.84E-08	3	1.18E-07
0.013	1.98E-26	0.16	8.17E-08	3.5	9.02E-08
0.014	8.06E-26	0.18	1.40E-07	4	7.16E-08
0.015	2.90E-25	0.2	2.12E-07	5	4.96E-08
0.016	9.42E-25	0.25	4.17E-07	6	3.69E-08
0.018	7.65E-24	0.3	6.11E-07	7	2.87E-08
0.02	4.72E-23	0.35	7.64E-07	8	2.31E-08
0.025	2.28E-21	0.4	8.69E-07	9	1.92E-08
0.03	3.69E-19	0.45	9.31E-07	10	1.58E-08

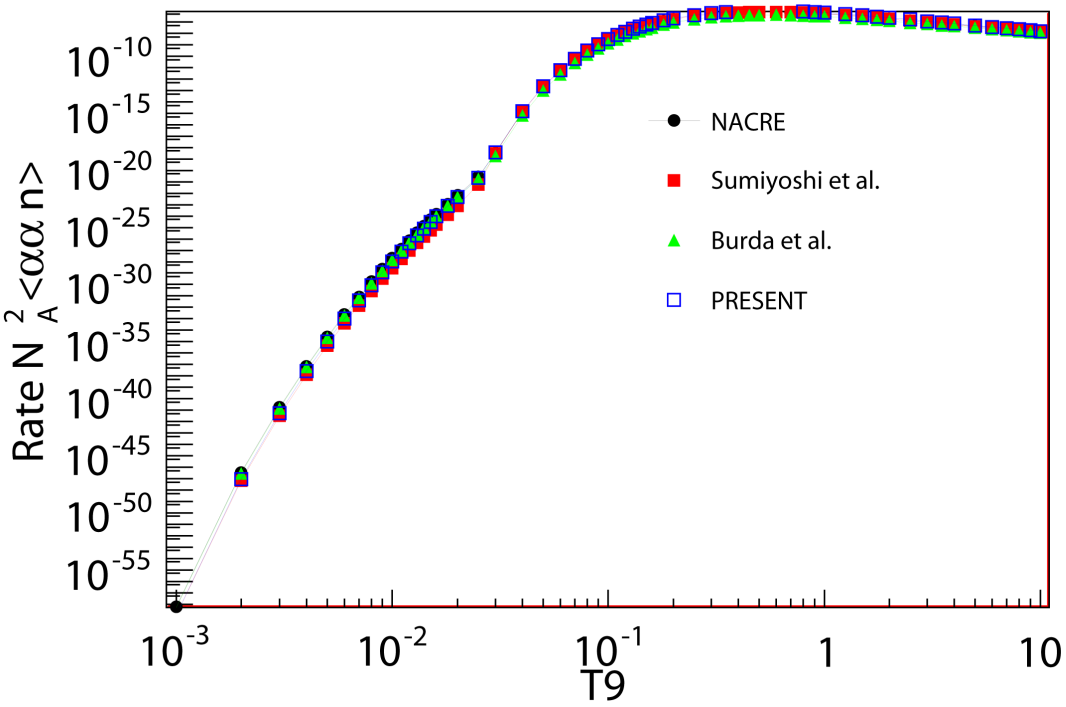

Figure 5.9: A log-log plot of $\langle \alpha\alpha n \rangle$ vs. T_9 does not reveal any obvious differences between the four rates being compared because of the large range covered. Temperatures most important for the r-process are $1 < T_9 < 5$.

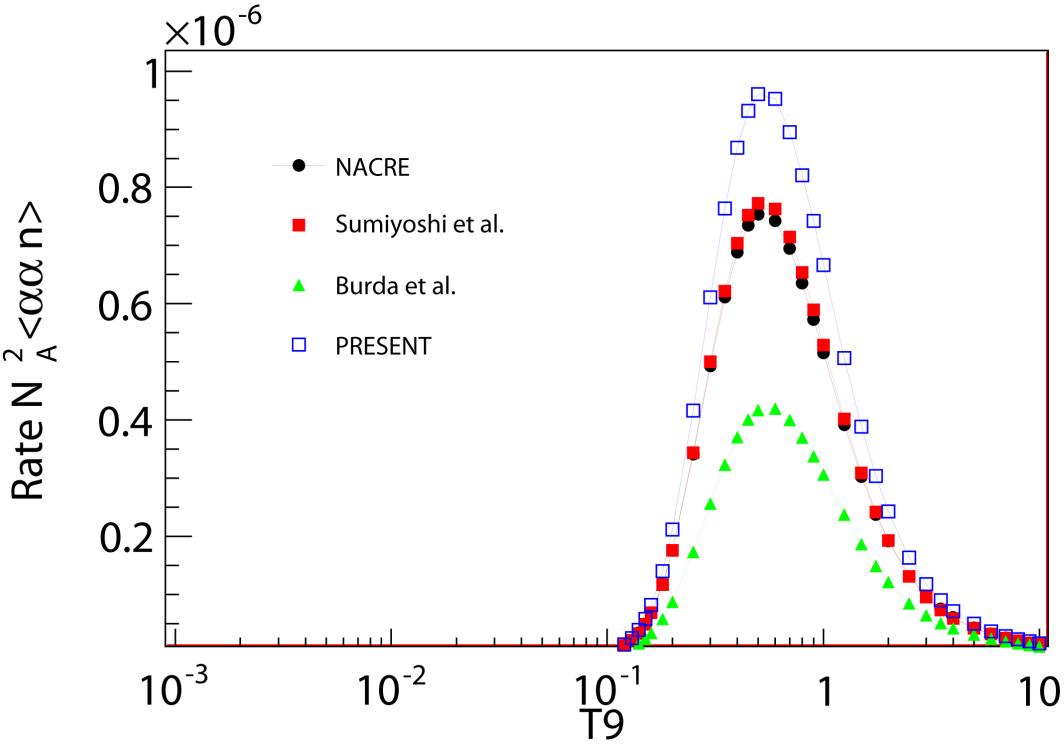

Figure 5.10: A semi-log plot shows the present rate to be larger than the rates of [Ang99] and [Sum02] at the peak near $T_9 = 0.5$ by 30%. Temperatures most important for the r-process are $1 < T_9 < 5$.

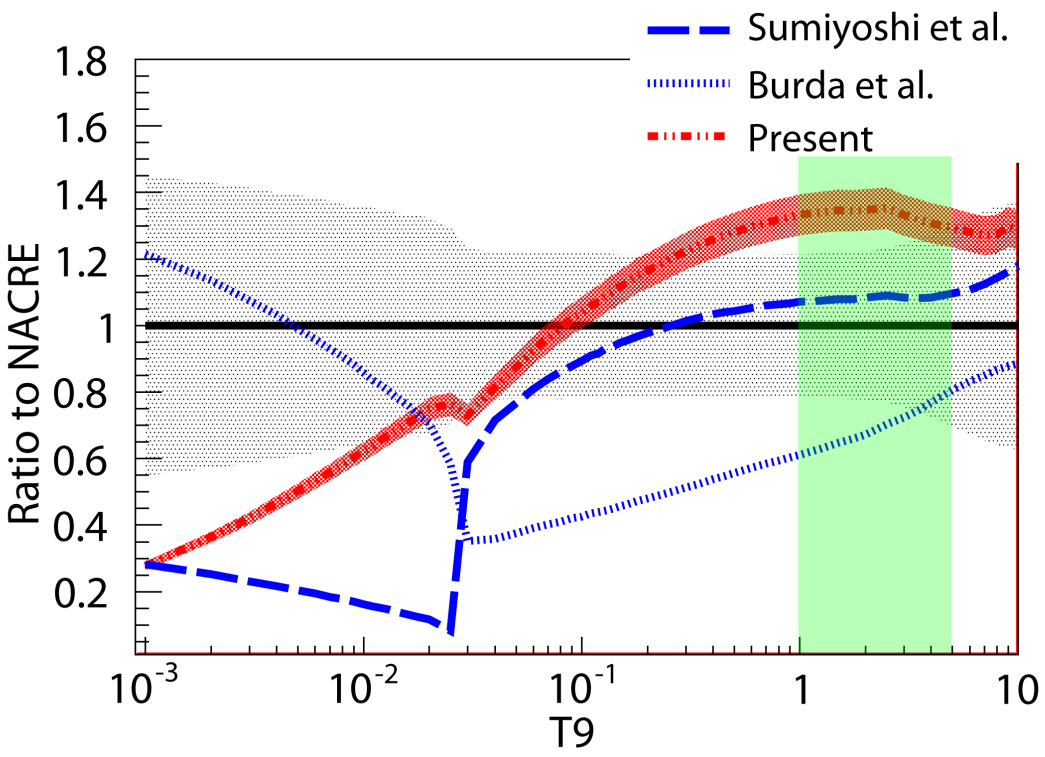

Figure 5.11: The differences between rates are much more easily seen when a ratio of the rates to the NACRE rate is generated. The astrophysically important region of $1 < T_9 < 5$ is shaded. Uncertainty bands are displayed for the NACRE rate and the present rate.

pared. The present rate is 35% larger than the NACRE rate when $T_9 = 2$, which is in the region most important for the nucleosynthesis models in question. The largest difference between rates exits in the off-resonant region. There, the present rate is smaller than NACRE by a factor of four. This happens primarily because the present rate calculation has used energy-dependent partial widths and the other rates did not.

In the present analysis, I attempted to reproduce the rates of each publication, using the published parameters and my code in order to establish confidence in the present comparison. Inconsistencies between the methods of the published works were evident. While NACRE and Burda *et al.* appear to follow the definition for E_n established by NACRE, Sumiyoshi *et al.* apparently used the resonant-capture-only definition of E_n for the resonance at threshold, that is,

$$E_n = E + E' - E_{^8Be} \tag{5.49}$$

which is consistent with the γ-ray energy definition of

$$E_\gamma = E + E' - E_{^8Be} + S_n \tag{5.50}$$

and Eq. 5.29; However, the authors of Ref. [Sum02] used the on-and-off resonant definition of E_n, or,

$$E_n = E' \tag{5.51}$$

for the $5/2^+$ resonance near 3 MeV. This was deduced after having reproduced the published rates of Ref. [Sum02] at all temperatures but one to within 1%. This difference in definition explains the order of magnitude difference and seeming discontinuity when taking the ratio of the Ref. [Sum02] to NACRE. The present rate was compiled following the energy definition used by Ref. [Ang99] as shown in Eq. 5.51.

The rate code presently used was also able to reproduce the NACRE rate reasonably well at nearly every temperature to within ~10% except for temperatures at the transition from the rate being predominantly off-resonance to predominantly on-resonance. This is achieved by assuming an energy-dependent neutron partial width for the $1/2^-$ state. This was not explicity stated in Ref. [Ang99]. The reproduction deviates by a maximum of 30% before quickly returning to agreement within a few percent (see Fig. 5.12). The rate of Ref. [Bur10] was reproduced to within 10% at all temperatures. Figure 5.12 shows the ratio of each rate computed using the published parameters and the present code, to the rate published by each respective work. If the present code were identical to the code of each published work, the expectation for all points should equal 1 for each plot of Fig. 5.12.

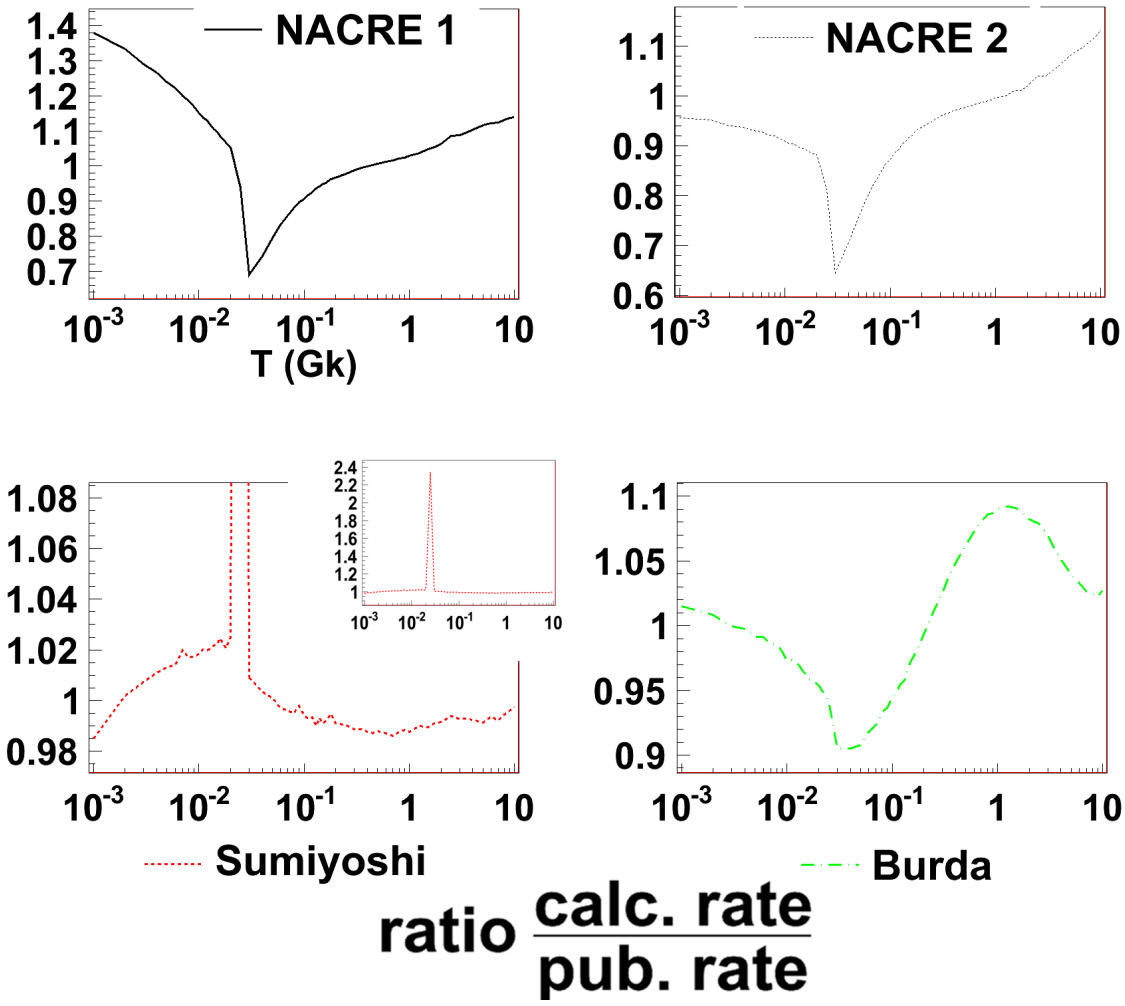

Figure 5.12: The ideal result for each plot is for all points = 1. The rate of Ref. [Sum02] was reproduced the best except at one point (inset) which was a factor of 2.2 larger than the reported value.

6 Discussion and Conclusions

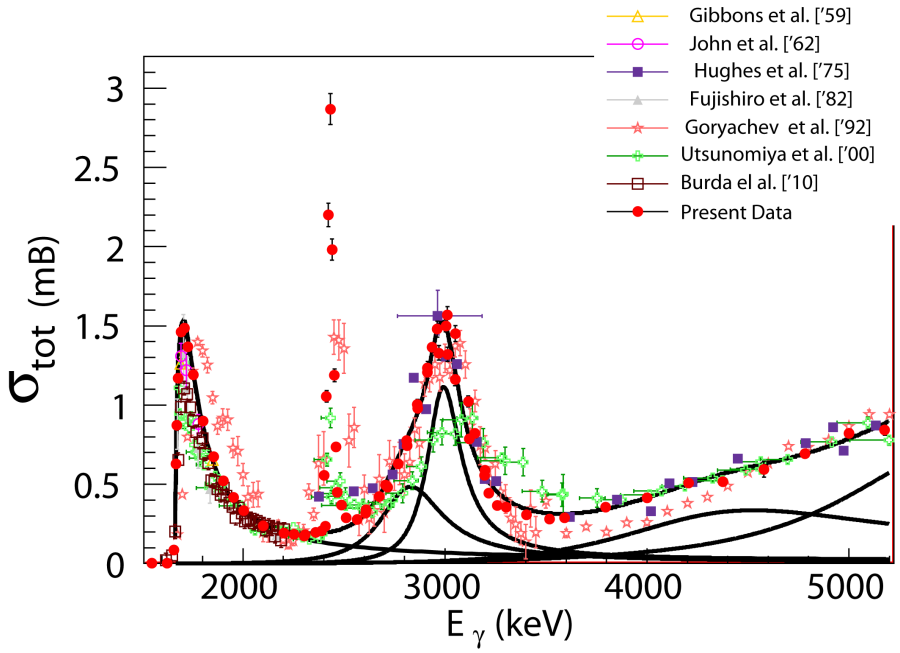

Figure 6.1: Collection of World data for the ^{9}Be$(\gamma, n)^{8}$Be reaction cross section. Fits derived from the present work are shown as solid black lines and display individual states in ^{9}Be as well as the their sum.

6.1 Discussion

6.1.1 The ^{9}Be$(\gamma, n)^{8}$Be Cross Section

The ^{9}Be$(\gamma, n)^{8}$Be reaction cross-section has been measured absolutely to ± 4.6%. The capabilities of HIγS and the high detection efficiencies of *Molly* and the INVS made possible

the unprecedented accuracy for this measurement.

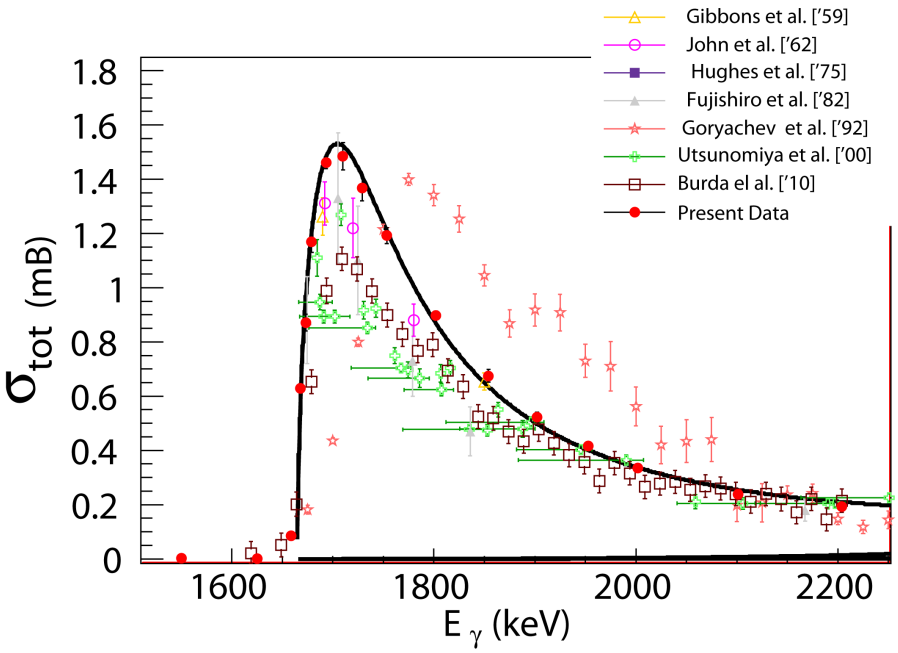

Figure 6.2: World data for the ^{9}Be$(\gamma, n)^{8}$Be reaction cross section near threshold. The solid line is a fit to the $1/2^{+}$ state.

Near the threshold, agreement between the present total cross-section data and existing data is mixed. The resonance location determined in the present analysis is in good agreement with that of Refs. [Sum02, Uts00, Fuj82] and in fair agreement with [Bur10]. The magnitude of the cross-section is is fair agreement with the cross-sections of [Gor92, Fuj82, Gib59b]. The resonance near threshold has, by far, the largest influence on the $\langle \alpha\alpha n \rangle$ rate.

The narrow $5/2^{-}$ state at 2.431 MeV has been more nearly resolved than ever before using γ-rays. The yield from the present data exhibit a peak which is more than a factor of 3 larger than the peak measured by Ref. [Uts00] and nearly a factor of 2 larger than the peak yield of Ref. [Gor92]. The current estimate of the width of this state would require a factor of 30 better resolution to begin to resolve the width experimentally.

The data over the broad $1/2^{-}$ and $5/2^{+}$ resonances, which lie near about 3 MeV, are in fair agreement with the data of Refs. [Hug75] and [Gor92] but not in good agreement with [Uts00]. It is presumed that the saw-tooth energy distribution of the γ-ray beam used by Utsunomiya *et al.* played a part in the ~ 75 keV difference in resonance location.

The present data beyond the broad hump at 3 MeV agree with [Uts00, Hug75], but not very well with [Gor92]. A $3/2^{+}$ at state at 4.7 MeV and a $3/2^{-}$ at state at 5.6 MeV are the next listed states on the energy level diagram for ^{9}Be [Til04]. These are known to be broad states [Dix91], but are largely neglected for consideration in rate calculations, since they are

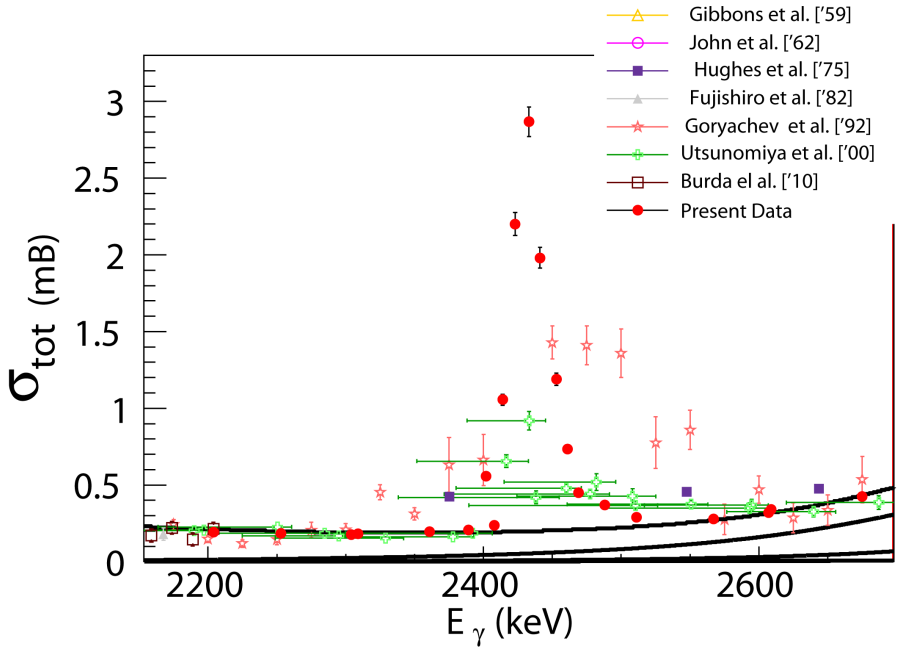

Figure 6.3: World data for the ^{9}Be$(\gamma, n)^{8}$Be reaction cross section over the narrow state at 2.431 MeV. This state could not be fit with the present data. The solid lines shown are the tails of other resonances.

located so far from threshold. Additionally, these states likely have stronger channels for decay to the 2^+ excited state in ^{8}Be.

Resonance parameters for the 6 lowest excited states of ^{9}Be, were deduced (with the exception of Γ_n for $5/2^-$, and E_R for $3/2^+$ and $3/2^-$). For the first time, explicit energy dependence for the neutron and γ-ray partial widths for each state was taken into account in the calculation of the ^{8}Be$(n, \gamma)^{9}$Be cross-section, and the astrophysical $\langle \alpha\alpha n \rangle$ rate.

The detectors used, in combination with the HIγS facility, provided an excellent means for making accurate absolute cross-section measurements quickly. The ^{9}Be nucleus may turn out to be a special case, however. First, since ^{9}Be has the lowest neutron separation energy (S_n) among light nuclei (1.6654 MeV), with the deuteron having the second lowest (2.225 MeV), the ^{9}Be$(\gamma, n)^{8}$Be reaction cross section may be measured up to about 5 MeV before the effects of (γ, n) reactions from other nuclei introduce significant contamination. Second, a γ-ray beam with 1% energy resolution near 2 MeV has a FWHM of 20 keV, while a 1% γ-ray beam of 20 MeV has 200 keV resolution. This means that narrow structures in nuclei may be harder to resolve with increasing S_n. Third, as E_γ increases, a detector like *Molly* will no longer be ~100% efficient, and may no longer be suitable for making absolute flux measurements. Additionally, techniques like the use of Pb attenuators (S_n = 7.367 MeV) will likely produce unwanted reaction products which would affect both the INVS and a γ-ray detector (*Molly* or

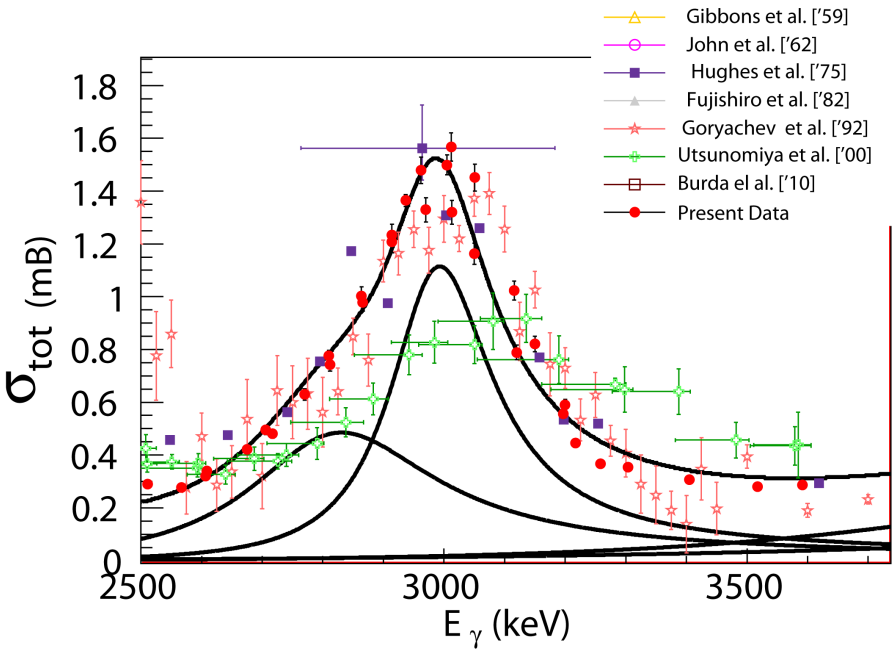

Figure 6.4: World data for the ^{9}Be$(\gamma,n)^{8}$Be reaction cross section over the broad peak at 3 MeV. The lower solid lines are the $1/2^{-}$ and $5/2^{+}$ states (left to right) in ^{9}Be. The upper solid line is the sum of all fitted states.

any other).

It should be noted, that ^{17}O (S_n = 4.143 MeV), and ^{13}C (S_n = 4.946 MeV) could be good candidates for (γ,n) cross-section measurements using the techniques described in this thesis.

6.1.2 Resonance Parameters

Table 6.1 contains resonance parameters for the $1/2^{+}$ state from several works. Notice that all but one of the evaluated (e,e') data produced reduced transition strengths, and γ-ray partial widths that are about 1/2 of the value of their (γ,n) counterparts. Perhaps interestingly, the anomalous parameters from the (e,e') subset of data, come from the authors of Ref. [Bar00] who merely analyzed the cross-section data of Ref. [Kue87]. Indeed, an inspection of the data from all the works of Table 6.1 reveal that the reported cross-sections of each work are mostly similar. None appear to be different by a factor of two. The authors of Ref. [Cle68] report a maximum cross section "of 1.55 mb at about 6 keV above threshold". Refs. [Kue87] and [Bur10] display plots of their data with maxima of about 1.25 mb each. It would appear as though there is an inconsistency in the method for the deduction of resonance parameters between groups who use (e,e') vs. (γ,n). The main difference between the analysis of üs. [Kue87, Bur10] and the analysis of (γ,n) data here and elsewhere, involves

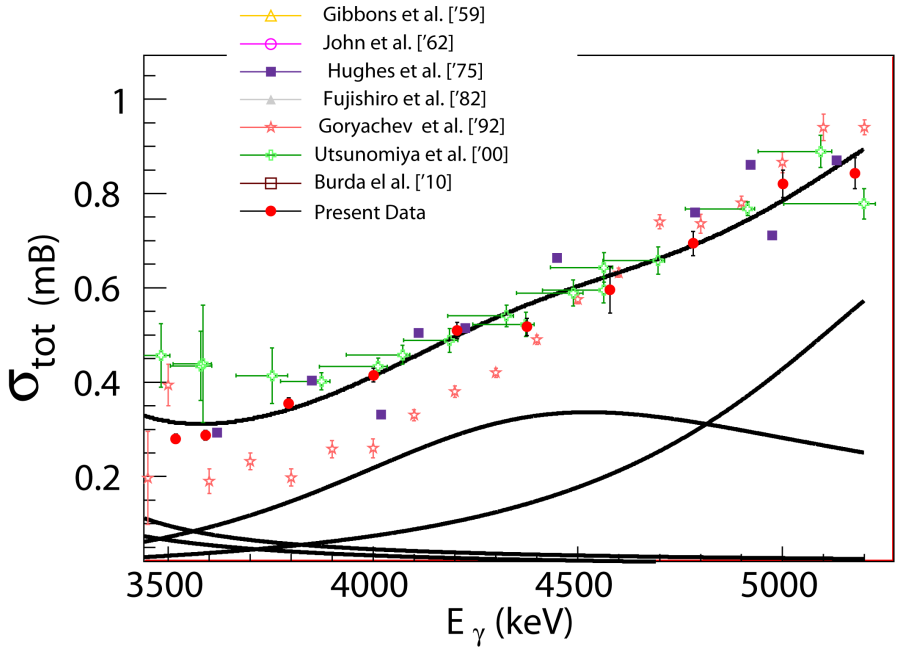

Figure 6.5: World data for the ^{9}Be$(\gamma, n)^{8}$Be reaction cross section beyond the broad peak at 3 MeV. The lower solid lines are the $3/2^{+}$ and $3/2^{-}$ states (left to right) in ^{9}Be. The upper line is the sum of all fitted states.

the use of Siegert's theorem for extracting the B(E1)↓. Ref. [Bur10] elaborates: "In first order perturbation theory, inclusive electron scattering cross-sections factorize in a longitudinal (C) and a transverse (E) part, reflecting the respective polarization of the exchanged virtual photon. The kinematics...favor longitudinal excitation, and thus, B(C1,q) rather than B(E1,q) is determined. Both quantities can be related by Siegert's theorem B(E1,q) = $(k/q)^2$B(C1,q); that is, they should be equal at the photon point q=k." The authors go on to discuss the models used to extract the parameters including plane-wave Born approximation, and no-core shell model calculations.

Since the data are all similar, and the reanalysis of the data of Ref. [Kue87] by Ref. [Bar00] gave closer results to the parameters extracted from (γ, n) data, all indications point to a violation of Siegert's theorem on the order of a factor of 2. In a present independent analysis of the data of Ref. [Bur10], I deduce γ-ray partial widths, and B(E1)↓ reduced transition strengths that are larger than what is published by a factor of two. It is my expectation, therefore, that if a B(E1)↓ for the $1/2^{+}$ state in ^{9}Be is extracted by fitting the absolute cross-section data from any of the works in Table 6.1 using the methods described in Chap. 4, that the result will be of the order of 0.1 e^2fm^2, rather than of the order of 0.05 e^2fm^2.

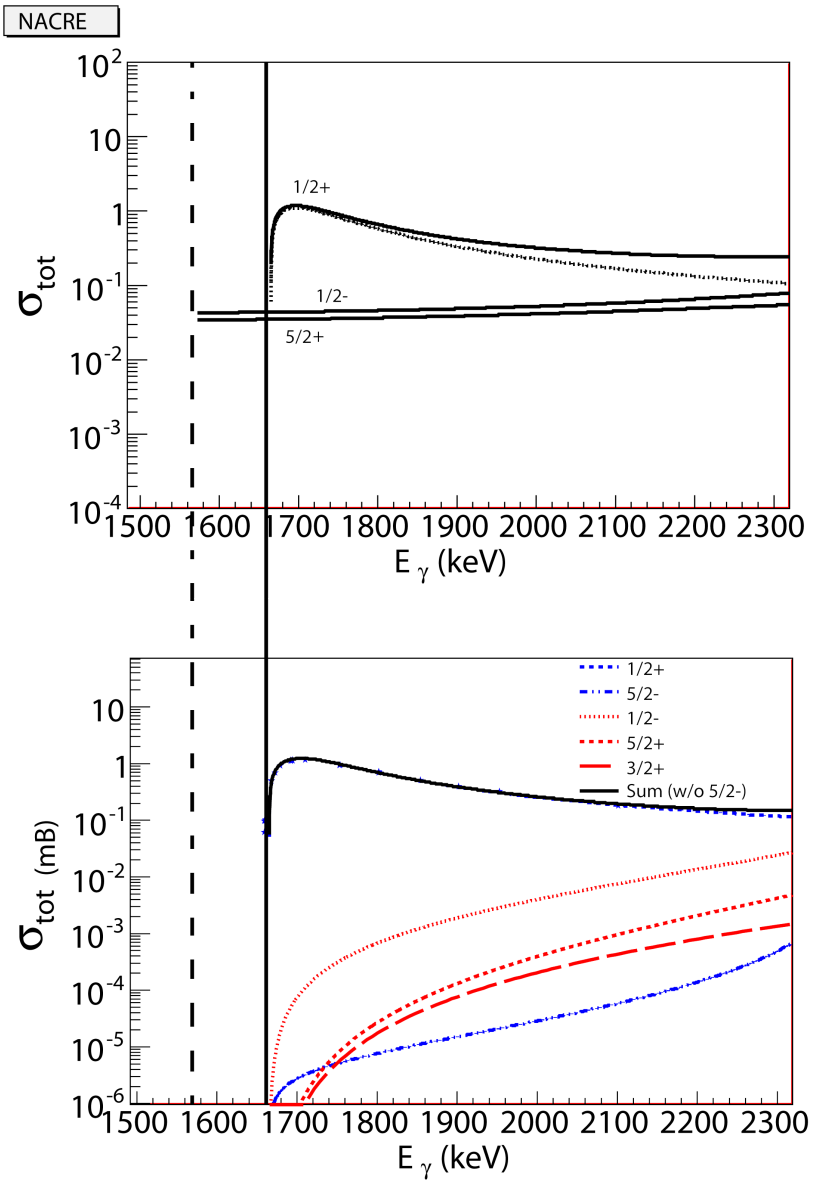

Figure 6.6: A graphical display of the differences between energy-independent (top), and energy-dependent (bottom) treatments of the cross-sections at threshold. The vertical solid line represents the two-body threshold, while the vertical dashed line represents the three-body threshold. The behavior of captured neutrons near threshold should exhibit energy dependence irrespective of the level into which they are captured.

Table 6.1: This table is a reproduction of Table 1 from Ref. [Bur10] with additions and slight modifications. It contains a "summary of the resonance parameters and reduced transition probabilities of the $1/2^+$ state of ^{9}Be deduced from different experiments. Ref. [Bar00] contains a reanalysis of the data of Ref. [Kue87]." Ref. [Bar83] contains analysis of the data of [Fuj82].

Reaction	Ref.	E_R(MeV)	Γ_n(keV)	Γ_γ(eV)	B(E1)↓(e^2fm^2)
(e,e')	[Cle68]	1.78	150±50	0.3	0.050±.020
(e,e')	[Kue87]	1.684	217±10	0.27	0.054
(e,e')	[Gli91]	1.68	200±20	0.34	0.068
(e,e')	[Bar00]	1.732	270	0.75	0.137
(e,e')	[Bur10]	1.748	274±8	0.302±0.045	0.054
(γ,n)	[Bar83]	1.733	227±50	0.577	0.106±.018
(γ,n)	[Ang99]	1.731	227±15	0.51±0.10	0.094±.020
(γ,n)	[Uts00]	1.748	283±42	0.598	0.107±.007
(γ,n)	[Sum02]	1.735	225±12	0.568	0.104±.002
(γ,n)	Present	1.7387±0.0008	226±3	0.745±0.008	0.135±.001

6.1.3 $\alpha(\alpha n,\gamma)^9$Be Rate Calculation

In principle, the precision of the ^{9}Be$(\gamma,n)^8$Be reaction cross-section should extend to the deduced astrophysical $\langle\alpha\alpha n\rangle$ rate. The quantities used for calculating the $\langle\alpha\alpha\rangle$ rate come from well known α + α scattering data [Wüs92], and the calculation of penetrabilities come from Coulomb wave function libraries, which are well established.

Recalling Fig. 5.11, the present rate, when compared to the NACRE rate, is a factor of 4 lower at the lowest calculated temperatures, while 30 - 35% larger at the astrophysical temperatures of interest for the r-process ($1 \leq T_9 \leq 5$) . The relative smallness of the rate at low temperatures is a direct result of treating all neutron partial widths with energy dependence. With the assumption of the correct analytic form for s,p,and d-wave neutrons coupling to ^{8}Be for all of the resonances described, all broad neutron partial widths have a an energy dependence which determines their shape close to the threshold. Fig. 6.6 demonstrates the effect on the cross-section for energy dependent vs. energy independent treatment of resonances. When treated without energy dependence, the tails of the higher-lying resonances terminate abruptly at the threshold. This directly leads to an inflated rate at low temperatures, along with the unintuitive result of a dominant contribution to the rate by the $1/2^-$ and $5/2^+$ states at these temperatures. Incidentally, the low rate of Ref. [Sum02], at low temperatures, appears to be a serendipitous result of using different definitions of E_n for the $1/2^+$ and $5/2^+$ resonances (Ref. [Sum02] did not observe a $1/2^-$ state). This description accounts for the seeming discontinuity at $T_9 = 0.025$ in Fig. 5.11.

The present results for the $\langle\alpha\alpha n\rangle$ rate at the important r-process temperatures are 25-

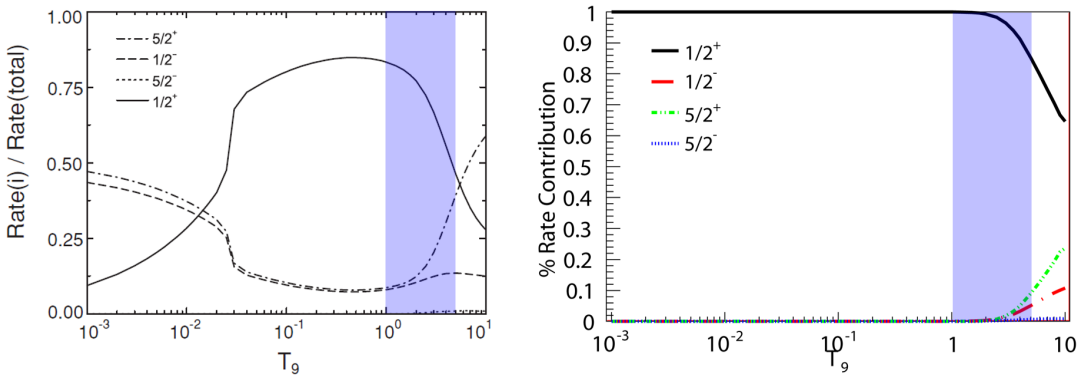

Figure 6.7: Two plots highlighting the relative contribution of each resonance to the rate as a function of temperature. The recent evaluation of Burda *et al.* [Bur10] is shown left, and the present evaluation is shown right. The important r-process temperatures are shaded.

35% larger than the rates of Refs. [Ang99, Sum02]. The present rate is consitantly about 30% than the NACRE rate for $1 \leq T_9 \leq 5$. Agreement with the NACRE rate marginally improves as $T_9 \rightarrow 10$. Figure 6.7 shows that for the present evaluation, the $1/2^+$ state is the primary contributor to the rate at all temperatures, contrary to the results of Burda *et al.* [Bur10]. However, contributions from other states may be signifigant for $T_9 \geq 2$. This implys that the choice of branching ratios is important for an accurate $\langle \alpha\alpha n \rangle$ rate determination. In the present evaluation, branching ratios determined from Ref. [Chr66] were used.

Abundance Predictions

Computer models of nucleosynthesis at the site of Type II supernovae often have at least three input parameters which determine the conditions of the explosion. These parameters are the dynamical time for the explosion, τ, the entropy/baryon (or rather the number of photons/baryon), s/k, and the electron fraction, Y_e [Sas06]. One approach to discerning "good" parameters, is a phenomenological one. That is, a range of reasonable parameters is estimated, and the parameter space is tested to find the combination of parameters which lead to the r-process [Sur10]. Now, recall the claims from Chap. 1, that the astrophysical rate of the $\alpha(\alpha n, \gamma)^9$Be reaction lays the ground work for the r-process. It is observed, that different $\langle \alpha\alpha n \rangle$ rates can have substantially different abundance yields for the same set of parameters. The present rate has not been used to produce an abundance plot, however some inferences can be made. The present rate is ~ 30% larger than the NACRE rate [Ang99] and so, will yield an abundance plot which most closely resembles the inflated NACRE rate prediction shown in Fig. 1.9.

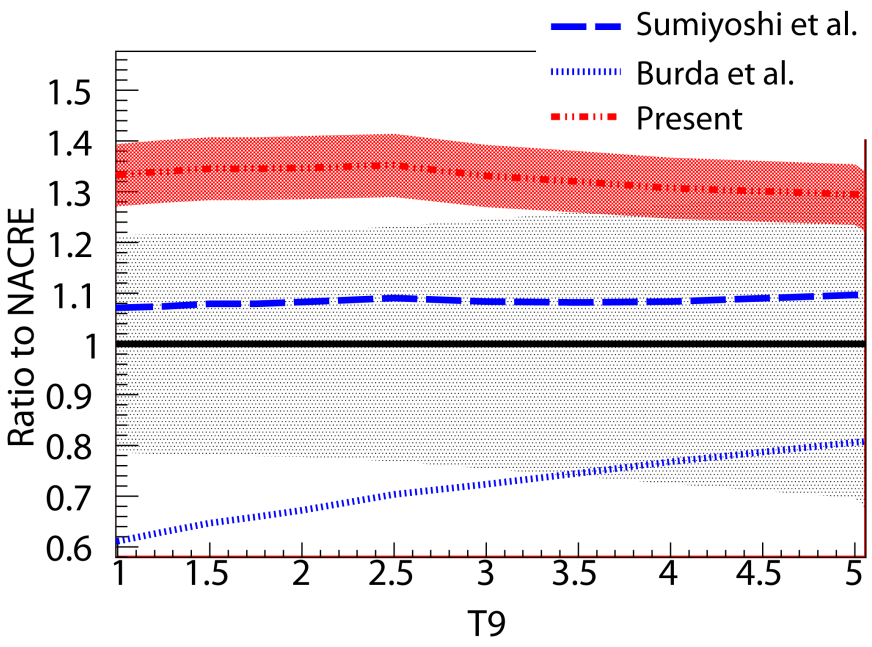

Figure 6.8: Zoomed in plot of the ratio of the present rate to the NACRE rate. This window represents the most important temperature range for r-process.

6.2 Conclusions

Accurate measurements of the ^{9}Be$(\gamma, n)^{8}$Be reaction cross section have been used to interpret the ^{8}Be$(n, \gamma)^{9}$Be reaction cross section, for calculating the astrophysical $\alpha(\alpha n, \gamma)^{9}$Be reaction rate. Applying energy dependent corrections for all neutron and γ-ray partial widths which approach the threshold gives rise to smaller rates when $T_9 \leq 0.025$. For $T_9 \geq 2$, contributions to the rate from higher lying resonances are substantial, and so accurate handling of branching ratios is important. With proper branching ratios, the present rate should be accurate at the level of $\pm 5\%$. This new precise rate should shrink the parameter space which abundance codes use for investigating the conditions necessary for the r-process at Type II supernovae sites.

7 Appendices

7.1 Appendix 1: Method for Determining Evaporated Target Thickness

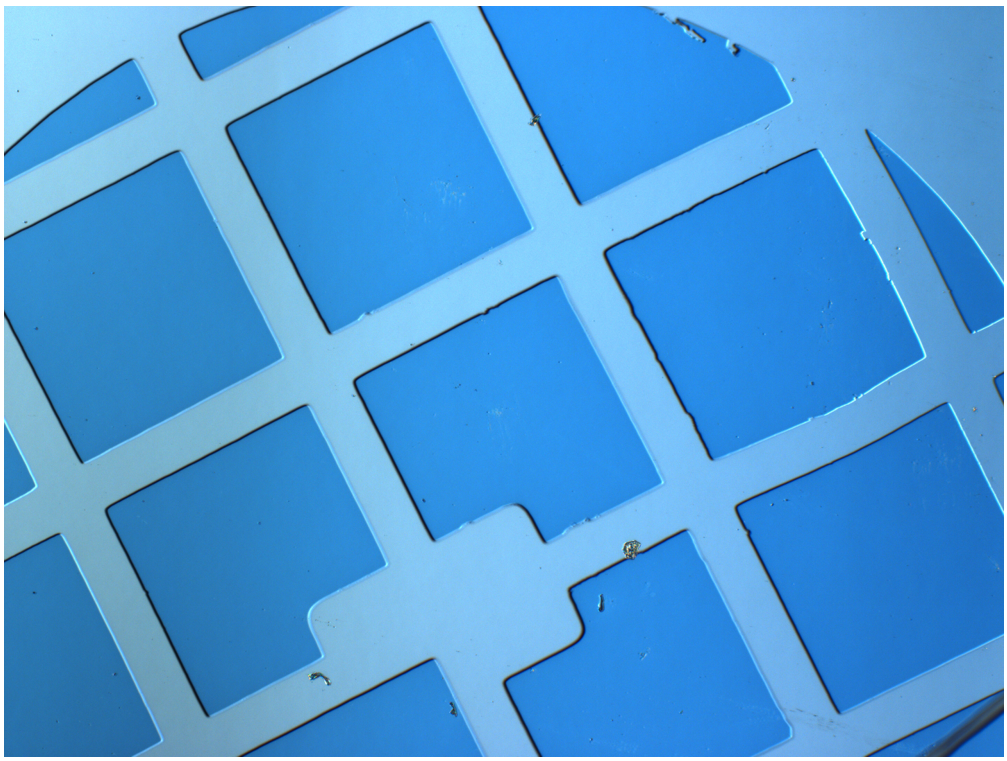

Figure 7.1: Photograph of Si wafer with deposited LiF. The removal of the contact-mask created regions with no deposited LiF (light blue). Differences in height were established by profilometry.

For the $^{7}\mathrm{Li}(p,n)^{7}\mathrm{Be}$ experiment, targets were prepared by evaporating LiF powder onto thin carbon foils. The LiF sample was concurrently evaporated onto substrates of atomically

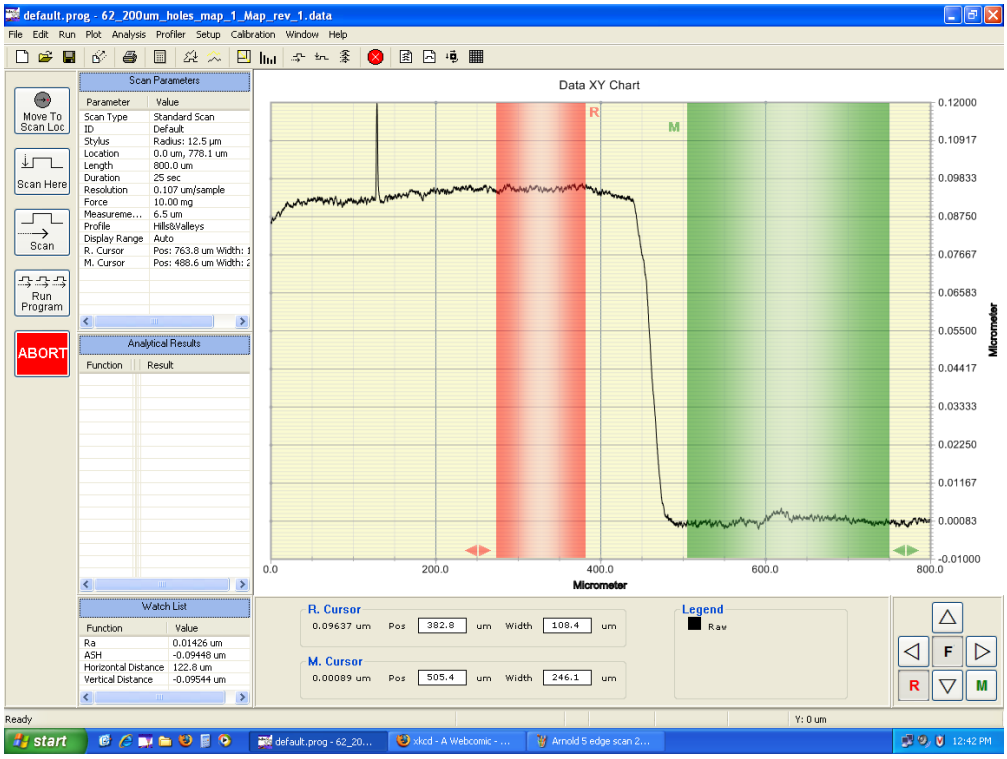

Figure 7.2: Screenshot of the relative height scan determined by profilometry. Software determines the difference between the average heights located within the broad vertical bands.

smooth silicon wafers. Wafers and foils were partnered and arranged symmetrically with respect to the evaporating sample. Assuming that the same average thickness of LiF was deposited onto the wafers and the carbon foils, profilometry was used to determine the LiF target thickness. Various contact-masks were applied to the wafers prior to evaporation and removed after evaporation and prior to measurements. A probe similar to an AFM tip scanned across 800 μm of the sample in one direction and recorded the differences in the height of the sample relative to the silicon wafer. Five scans over different sections of the wafer-partner to the target foil used in this experiment yielded a thickness of 39.8 ± 1.4 μg/cm^2 of LiF. This converts to an atomic density of 9.24e+17 Li atoms/cm^2. The isotopic abundance of ^{7}Li in natural Li is 92.5% [dL03] yielding a density of 8.54e+17 ^{7}Li nuclei/cm^2 for the sample with an uncertainty of ± 3.5%.

7.2 Appendix 2: The Data

Table 7.1 contains the ^{9}Be$(\gamma,n)^{8}$Be cross section data from January and July. Run numbers 79-367 are July runs, and run numbers 2109 and above are January run numbers. The column "Type of Run" uses shorthand like "NR" which stands for "Normal Run" and "Pb Test #", where the # is the thickness of lead in inches. The absolute cross section measurement, and a measurement which was normalized to the ^{2}H$(\gamma,n)^{1}$H cross section is included along with uncertainties.

Table 7.1: This Table contains the analyzed ^{9}Be$(\gamma,n)^{8}$Be cross section data obtained and used in the present work.

Run No.	Type of Run	γ-ray Energy	Absolute Measurement of σ_{Total} for ^{9}Be$(\gamma,n)^{8}$Be (mb)	Unc. (mb)	σ_{Total} for ^{9}Be$(\gamma,n)^{8}$Be Normalized to ^{2}H$(\gamma,n)^{1}$H (mb)	Unc. (mb)
79	Pb Test 0	2.937	1.457	0.494	1.556	0.617
80	Pb Test .5	2.937	1.141	0.452	1.271	0.556
81	Pb Test .5	2.937	1.321	0.113	1.170	0.110
82	Pb Test 1	2.937	1.339	0.152	1.344	0.175
83	Pb Test 2	2.937	1.322	0.074	1.234	0.072
84	Pb Test 2	2.937	1.372	0.078	1.294	0.076
85	Pb Test 2	2.937	1.459	0.059	1.388	0.046
90	Pb Test 4	2.937	1.389	0.048	1.351	0.015
91	Pb Test 3	2.937	1.334	0.046	1.285	0.018
92	Pb Test 3	2.937	1.319	0.061	1.288	0.056
96	NR	2.402	0.557	0.019	0.553	0.006
99	NR	2.414	1.056	0.036	1.046	0.008
102	NR	2.423	2.200	0.074	2.188	0.018
106	NR	2.433	2.867	0.097	2.877	0.034
109	NR	2.441	1.981	0.067	1.966	0.021
114	NR	2.453	1.189	0.041	1.183	0.012
118	NR	2.461	0.736	0.026	0.733	0.010
121	NR	2.469	0.450	0.017	0.444	0.008
126	Pb Test 4	2.389	0.197	0.008	0.195	0.004
128	Pb Test 3	2.389	0.220	0.011	0.216	0.008
154	NR	1.498	-0.001	-0.001	N/A	N/A
157	NR	1.550	0.002	0.000	N/A	N/A

Table 7.1: (Continued)

Run No.	Type of Run	γ-ray Energy	Abs.σ_{Total} (mb)	Unc. (mb)	Norm.σ_{Total} (mb)	Unc. (mb)
162	NR	1.575	-0.002	-0.001	N/A	N/A
165	NR	1.625	0.001	0.000	N/A	N/A
168	NR	1.659	0.083	0.003	N/A	N/A
171	extra Be Run	1.659	0.120	0.010	N/A	N/A
173	NR	1.679	1.169	0.040	N/A	N/A
176	NR	1.673	0.872	0.031	N/A	N/A
179	NR	1.668	0.629	0.024	N/A	N/A
180	NR*	1.668	0.630	0.023	N/A	N/A
183	NR	1.694	1.508	0.052	N/A	N/A
184	Pb Test 2	1.694	1.447	0.049	N/A	N/A
185	targ atten	1.694	1.498	0.053	N/A	N/A
187	Pb Test 2	1.694	1.460	0.054	N/A	N/A
189	Pb Test 0	1.694	1.422	0.091	N/A	N/A
197	NR	1.710	1.484	0.051	N/A	N/A
206	NR	1.729	1.367	0.047	N/A	N/A
214	NR	1.753	1.191	0.041	N/A	N/A
216	targ atten	1.754	1.194	0.042	N/A	N/A
220	NR	1.802	0.911	0.032	N/A	N/A
221	Pb Test 3	1.802	0.907	0.032	N/A	N/A
222	Pb Test 0	1.802	0.861	0.033	N/A	N/A
225	NR	1.854	0.675	0.023	N/A	N/A
228	NR	1.902	0.523	0.019	N/A	N/A
231	NR	1.953	0.416	0.015	N/A	N/A
234	NR	2.002	0.334	0.012	N/A	N/A
236	Pb Test 0	2.002		0.019	N/A	N/A
239	NR	2.101	0.238	0.008	N/A	N/A
242	NR	2.204	0.193	0.007	N/A	N/A
246	NR	2.253	0.186	0.007	N/A	N/A
258	NR	2.309	0.182	0.007	N/A	N/A
263	NR	2.385	0.212	0.008	N/A	N/A
267	NR	2.408	0.236	0.009	N/A	N/A
271	NR	2.511	0.290	0.010	0.283	0.003
274	NR	2.609	0.340	0.012	0.342	0.004

Table 7.1: (Continued)

Run No.	Type of Run	γ-ray Energy	Abs.σ_{Total} (mb)	Unc. (mb)	Norm.σ_{Total} (mb)	Unc. (mb)
281	NR	2.706	0.495	0.018	0.485	0.008
286	NR	2.809	0.772	0.027	0.764	0.012
290	NR	2.914	1.233	0.042	1.232	0.014
293	NR	2.864	1.003	0.034	0.988	0.011
296	NR	3.012	1.567	0.053	1.554	0.013
302	NR	3.116	1.023	0.035	0.990	0.012
307	NR	2.361	0.196	0.008	N/A	N/A
313	NR	2.962	1.479	0.050	1.463	0.013
316	NR	3.051	1.451	0.050	1.431	0.019
319	NR	3.150	0.821	0.029	0.803	0.011
322	Pb Test 4	3.197	0.556	0.020	0.536	0.009
322	NR	3.197	0.554	0.020	0.534	0.009
338	NR	2.304	0.176	0.008	N/A	N/A
343	NR	3.004	1.509	0.051	1.492	0.014
345	Pb Test 3	3.006	1.489	0.055	1.493	0.029
351	Pb Test 4	1.692	1.473	0.050	N/A	N/A
353	Pb Test 0	1.692	1.421	0.050	N/A	N/A
355	Pb Test 3	1.692	1.444	0.050	N/A	N/A
362	Pb Test 4	2.811	0.781	0.026	0.796	0.005
363	Pb Test 0	2.811	0.721	0.034	0.757	0.043
367	Pb Test 4	3.200	0.589	0.021	0.596	0.010
2109	NR	3.258	0.368	0.014	0.365	0.007
2113	NR	3.304	0.354	0.014	0.350	0.008
2117	NR	3.405	0.307	0.012	0.305	0.006
2121	NR	3.518	0.280	0.010	0.279	0.004
2129	NR	3.591	0.287	0.010	0.289	0.004
2132	NR	3.794	0.355	0.012	0.357	0.005
2135	NR	4.001	0.415	0.014	0.402	0.005
2149	NR	4.205	0.510	0.018	0.478	0.006
2151	NR	4.376	0.517	0.018	0.500	0.008
2159	NR	4.579	0.596	0.048	0.589	0.009
2162	NR	4.782	0.694	0.025	0.671	0.011
2166	NR	5.001	0.821	0.029	0.748	0.014

Table 7.1: (Continued)

Run No.	Type of Run	γ-ray Energy	Abs.σ_{Total} (mb)	Unc. (mb)	Norm.σ_{Total} (mb)	Unc. (mb)
2169	NR	5.177	0.843	0.033	0.830	0.013
2182	NR	2.488	0.370	0.013	0.368	0.002
2195	NR	2.567	0.277	0.010	0.276	0.005
2197	NR	2.675	0.423	0.015	0.427	0.007
2200	NR	2.770	0.629	0.022	0.632	0.026
2202	NR	2.866	0.979	0.033	1.000	0.011
2206	NR	2.970	1.330	0.046	1.355	0.016
2208	NR	3.050	1.162	0.040	1.160	0.015
2245	NR	2.607	0.320	0.012	0.327	0.007
2250	NR	2.717	0.481	0.017	0.486	0.007
2252	NR	2.812	0.743	0.026	0.747	0.009
2256	NR	2.914	1.207	0.041	1.228	0.013
2260	NR	3.013	1.320	0.045	1.335	0.014
2262	NR	3.120	0.789	0.027	0.759	0.006
2265	NR	3.217	0.445	0.016	0.438	0.007

7.3 Appendix 3: Fit Parameters

Each data set from January and July were fit using the function

$$0.0320097703 * 10 * x * [0] * 2.0 * ([1] * (x - 1665.4))^{(0.5)}/((x - [2])^2 + ([1] * (x - 1665.4)))$$
$$+$$
$$0.0320097703 * x * 0.0110574568 * 10 * [3] * (2.0 * [4] * (0.00075322)^{(3/2)} * (x - 1665.4)^{(3/2)}/(1 + (0.00075322) * (x - 1665.4)))/((x - [5])^2 + (1/4) * (2.0 * [4] * (0.00075322)^{(3/2)} * (x - 1665.4)^{(3/2)}/(1 + (0.00075322) * (x - 1665.4)))^2)$$
$$+$$
$$0.0960293108 * x * 10 * [6] * (2.0 * [7] * (0.00075322)^{(5/2)} * (x - 1665.4)^{(5/2)}/(9. + 3. * (0.00075322) * (x - 1665.4) + (0.00075322)^2 * (x - 1665.4)^2))/((x - [8])^2 + (1/4) * (2.0 * [7] * (0.00075322)^{(5/2)} * (x - 1665.4)^{(5/2)}/(9. + 3. * (0.00075322) * (x - 1665.4) + (0.00075322)^2 * (x - 1665.4)^2))^2)$$
$$+$$
$$0.0640195405 * x * 10 * [9] * (2.0 * [10] * (0.00075322)^{(5/2)} * (x - 1665.4)^{(5/2)}/(9. + 3. * (0.00075322) * (x - 1665.4) + (0.00075322)^2 * (x - 1665.4)^2))/((x - [11])^2 + (1/4) * (2.0 * [10] * (0.00075322)^{(5/2)} * (x - 1665.4)^{(5/2)}/(9. + 3. * (0.00075322) * (x - 1665.4) + (0.00075322)^2 * (x - 1665.4)^2))^2)$$
$$+$$
$$0.0640195405 * x * 0.0110574568 * 10 * [12] * (2.0 * [13] * (0.00075322)^{(3/2)} * (x - 1665.4)^{(3/2)}/(1 + (0.00075322) * (x - 1665.4)))/((x - [14])^2 + (1/4) * (2.0 * [13] * (0.00075322)^{(3/2)} * (x - 1665.4)^{(3/2)}/(1 + (0.00075322) * (x - 1665.4)))^2)$$

where x is γ-ray energy with units keV and the bracketed numbers [0] - [14] are the fitting parameters. The following table catalogs the parameters obtained. The formula includes factors of 10 and such, so that the resulting scale of the parameters conformed to the desired units. The B(E1) strengths have units of e^2fm^2 while the B(M1) strengths are in units of nuclear magnaton squared ($\mu_N^2 \approx 0.01$ e^2fm^2). The factor ϵ and the reduced partial widths γ^2 have units of keV. The resonance energy also has units of keV.

Table 7.2: This Table contains the the parameters obtained from fitting the data. E_R was fixed for two highest resonances and so the uncertainty in those parameters ([11] and [14]) is accordingly zero.

	January Abs.	Unc.	January Norm.	Unc.	July Abs.	Unc.	July Norm.	Unc.
B(E1) [0]	0.0000	0.0000	0.0000	0.0000	0.1355	0.0014	0.0000	0.0000
ϵ [1]	0.0000	0.0000	0.0000	0.0000	174.7060	5.4400	0.0000	0.0000
E_R [2]	0.0000	0.0000	0.0000	0.0000	1738.6500	0.7797	0.0000	0.0000
B(M1) [3]	4.6886	0.9111	4.3755	0.3662	4.0823	0.5546	5.4097	0.2935
γ^2 [4]	434.2270	22.1385	428.8390	9.9009	417.6480	28.9178	465.2870	9.0484
E_R [5]	2844.1100	26.8067	2840.7100	11.7215	2821.6900	19.4020	2855.0400	8.6810
B(E1) [6]	0.0173	0.0032	0.0193	0.0013	0.0247	0.0017	0.0205	0.0009
γ^2 [7]	1273.7300	127.6990	1375.3200	46.1369	1456.1700	62.6965	1356.3300	30.4210
E_R [8]	2994.2000	7.7409	2991.0500	2.6305	3005.7200	2.8760	3008.9700	1.0708
B(E1) [9]	0.0599	0.0055	0.0610	0.0022	0.0000	0.0000	0.0000	0.0000

Table 7.2: (Continued)

	January Abs.	Unc.	January Norm.	Unc.	July Abs.	Unc.	July Norm.	Unc.
γ^2 [10]	2952.8300	163.6020	3013.3200	69.9394	0.0000	0.0000	0.0000	0.0000
E_R [11]	4704.0000	0.0000	4704.0000	0.0000	0.0000	0.0000	0.0000	0.0000
B(M1) [12]	7.2038	0.8885	6.4670	0.3149	0.0000	0.0000	0.0000	0.0000
γ^2 [13]	599.2820	103.8050	520.1840	49.3461	0.0000	0.0000	0.0000	0.0000
E_R [14]	5590.0000	0.0000	5590.0000	0.0000	0.0000	0.0000	0.0000	0.0000

7.4 Appendix 4: Rate Code

The rate code was adapted from an $\langle \alpha\alpha\alpha \rangle$ rate code written in Fortran. The code was graciously given to me by A. Coc via C. Iliadis. The physical constants from the file "phyconst.incl" are included at the end.

```
c234567
      program aanP

      implicit none

      include 'phyconst.incl'

      integer     nb_steps,      nw_gamow   ,nw_reson
      parameter (nb_steps=1000,nw_gamow=4,nw_reson=100)
      integer     nb_steps_aa, nb_steps_bn
      parameter (nb_steps_bn = 600)

      real*8 amass_a, amass_b, amass_c, amass_b9, amass_n

      real*8 e_bn, e_aa, h_aa, h_bn
      real*8 j12, j52, e_neutron, sigma_coef
      real*8 GG12p, GG52p, GG12m, GN12p, GN12m, GN52p, GG52m

      real*8 dbdbd, d_lambda
      real*8 E_hoyle, er_hoyle, er_hoyle0 ,e_gamma, e_gamma0,
     &   e_b_gs, e_b_gs0, e_be_ns
      real*8 Gamma_tot, Gamma_gamma, Gamma_gamma0,Gamma_alpha_b,
     & Gamma_alpha_c, Gamma_alpha_b0,  Gamma_alpha_c0,
     & Gamma_gamma1, Gamma_alpha_b1,  Gamma_alpha_c1,
     & omega_gamma, tau_b,
     & Gamma_g_be9_1,Gamma_g_be9_2, Gamma_g_be9_3, Gamma_g_be9_4,
     & Gamma_n_be9_1,Gamma_n_be9_2, Gamma_n_be9_3, Gamma_n_be9_4
      real*8 red_gamma_alpha_b, red_gamma_alpha_c, red_Gamma_gamma
      real*8 red_gamma_n_be9_1, red_gamma_n_be9_2, red_gamma_n_be9_3,
     & red_gamma_n_be9_4, omega_gamma1, omega_gamma2, omega_gamma3,
     & omega_gamma4
      real*8 red_gamma_g_be9_1, red_gamma_g_be9_2, red_gamma_g_be9_3,
     & red_gamma_g_be9_4
      real*8 factor_aa, factor_bn
      real*8 rho_aa, rho_bn, ak_aa, ak_bn, rk2_aa, rk2_bn
      real*8 eta_bn, eta0_bn, radius_bn, red_mass_bn
      real*8 eta_aa, eta0_aa, radius_aa, red_mass_aa
      real*8 gamow_max, t9, t923, bkt, e_min0
      real*8 sv_aan, sv_aan1, sv_aan2, raan, sig_bn, sig_aa, sum_bn
      real*8 sigma_gn_1, sigma_gn_2, sigma_gn_3, sigma_gn_4, sigma_gn
      real*8 pas, pen, penj
      real*8 Red_GamN12p, Ggfactor1, Ggfactor2
```

```
      real*8 lil_gam_52p, lil_gam_12m, lil_eps_12p, xi

      real*8 e_min(2,3), e_max(2,3), GPeak0(2)
      real*8 e_min_nbe(2,3), e_max_nbe(2,3), dE_step(2,3)
      integer    i_aa,      i_bn
      parameter (i_aa = 2, i_bn = 1)
      integer k_aa, k_bn, l_aa, l_bn, kl_bn, ii, jj, kk
      integer i_bd, i_temp
      integer nint_aa, nint_bn
      logical l_newt

      real*8 ERez12p, ERez12m, ERez52p, ERez52m
      real*8 GamN12p, GamN12m, GamN52p, GamN52m, Gn
      real*8 GamG12p, GamG12m, GamG52p, GamG52m
      real*8 B_Strength12p, B_Strength12m, B_Strength52p, B_Strength52m
      real*8 B_R_12p, B_R_12m, B_R_52p, B_R_52m

      integer   nb_temp   ,nb_bd
      parameter(nb_temp=60,nb_bd=21)

      real*8 fc(10),gc(10),dfc(10),dgc(10)
      real*8 pen_bn(3*nb_steps)


!*********************************************************************

      complex*16 f(0:10), g(0:10), fp(0:10), gp(0:10), sig(0:10)
      complex*16 z, eta, zlmin
      integer nl, kfn, mode, jpr, jfail
      parameter (nl=8, kfn=-1, mode=1)

!*--------------------------------------------------------------------*

      integer mx_svtab
      parameter (mx_svtab=60)
      real*8 t9_tab(mx_svtab)
      data   t9_tab /
     &       0.001, 0.002, 0.003, 0.004, 0.005, 0.006, 0.007, 0.008,
     &       0.009, 0.010, 0.011, 0.012, 0.013, 0.014, 0.015, 0.016,
     &       0.018, 0.020, 0.025, 0.030, 0.040, 0.050, 0.060, 0.070,
     &       0.080, 0.090, 0.100, 0.110, 0.120, 0.130, 0.140, 0.150,
     &       0.160, 0.180, 0.200, 0.250, 0.300, 0.350, 0.400, 0.450,
     &       0.500, 0.600, 0.700, 0.800, 0.900, 1.000, 1.250, 1.500,
     &       1.750, 2.000, 2.500, 3.000, 3.500, 4.000, 5.000, 6.000,
     &       7.000, 8.000, 9.000,10.000/

!*--------------------------------------------------------------------*
```

```
      real*8 aabe, beac, aang, raab

      jpr = 0
      zlmin = cmplx(0.d0,0.d0)

      do kk = 0, 10
        f(kk) = 0.d0
        g(kk) = 0.d0
        fp(kk) = 0.d0
        gp(kk) = 0.d0
        sig(kk) = 0.d0
      enddo

      e_min0 = 1.d-3

!***********************************************************************
!234567890123456789012345678901234567890123456789012345678901234567890123456789012
!       1         2         3         4         5         6         7
!***********************************************************************

      amass_a = 4.00260325415d0 * cs_uma     ! Audi 2003
      amass_b = 8.00530510d0    * cs_uma     ! Audi 2003
      amass_b9 = 9.0d0*cs_uma + 11.347648d0 ! Audi 2003
      amass_n = cs_mneut                     ! Audi 2003

      e_b_gs0 = amass_b - 2.d0 * amass_a

      e_be_ns = amass_b9 - amass_b -amass_n  ! Q value
      e_be_ns = -1.0d0*e_be_ns ! Make it positive !!
      Gamma_alpha_b0 = 5.57d-6 ! (MeV) WUS92

! Resonance parameters for 9Be(g,n) (changed 10/07/2010)
      ERez12p =  1.73865d0      ! PRESENT
      ERez52m = 2.4314d0        ! PRESENT
      ERez12m =  2.840d0        ! PRESENT
      ERez52p =  3.000d0        ! PRESENT
c
      GamN12p = 2.26d-1       ! PRESENT
      GamN52m = 7.7d-4          ! PRESENT changed from d-5 to d-4
      GamN12m = 3.856d-1        ! PRESENT
      GamN52p = 2.118d-1        ! PRESENT
c
c      Red_GamN12p = 0.813152     ! PRESENT
      lil_gam_12m = 0.4365d0    ! Present 01/2011
      lil_gam_52p = 1.365d0     ! Present 01/2011
      lil_eps_12p = 0.1747d0    ! Present 01/2011
```

```
      xi = 0.75322d0              ! Present 01/2011
c
      GamG12p = 7.452d-7        ! PRESENT
      GamG52m = 9.7d-8          ! PRESENT
      GamG12m = 1.23d-6         ! PRESENT
      GamG52p = 0.578d-6        ! PRESENT
c
      B_Strength12p = 0.13547d0  ! PRESENT
      B_Strength52m = 0.59d0  ! PRESENT
      B_Strength12m = 4.639d0  ! PRESENT
      B_Strength52p = 0.0204d0  ! PRESENT
c
      B_R_12p = 1.0d0           ! PRESENT
      B_R_52m = 1.0d0 !6.d-2          ! PRESENT
      B_R_12m = 1.0d0 !3.2d-1         ! PRESENT
      B_R_52p = 1.0d0 !4.6d-1         ! PRESENT
!       Factors from  NACRE
      Ggfactor1 = (16.0d0*cs_pi/9.0d0)*cs_finesc*(1/cs_hbarc_nu)**2
      Ggfactor2 = (16.0d0*cs_pi/9.0d0)*cs_finesc*(1/(2.0d0*cs_mprot))**2
      j12 = 0.25
      j52 = 0.75
!*********************************************************************
!*********************************************************************

      red_mass_aa = amass_a/2.d0 ! alpha + alpha reduced mass in MeV
      eta0_aa = 2.d0**2 * cs_finesc * sqrt ( red_mass_aa / 2.d0 )
      eta_aa  = eta0_aa / sqrt ( e_b_gs0 )
      radius_aa = 2.d0 * 1.45d0 * 4.d0 ** (1.d0/3.d0)
      !radius_aa = 6.d0
      rk2_aa = 2.d0 * red_mass_aa / cs_hbarc_nu**2
      ak_aa = sqrt ( 2.d0 * red_mass_aa * e_b_gs0 ) / cs_hbarc_nu
      rho_aa = ak_aa * radius_aa
      eta = cmplx(eta_aa,0.d0)
      z = cmplx(rho_aa,0.d0)
      call wclbes(z,eta,zlmin,nl,f,g,fp,gp,sig,kfn,mode,jfail,jpr)
      if(jfail.ne.0) then
        write(*,*) ' jfail = ',jfail
        stop ' Failed '
      end if
      pen = rho_aa/(f(0)**2+g(0)**2)
      red_gamma_alpha_b = Gamma_alpha_b0 / pen

!*********************************************************************

      red_mass_bn  = amass_b*amass_n/(amass_b+amass_n) ! reduced mass n + 8Be
!*********************************************************************
```

```
      GPeak0(i_aa) = ( cs_pi * cs_finesc * 2.d0*2.d0 / cs_c9boltz ) **
     &  (2.d0/3.d0) * ( red_mass_aa  / 2.d0 ) ** (1.d0/3.d0)

      pas = 1.d-3

!*********************************************************************
!*********************************************************************
!       do 101 i_bd = -9, 6 ! BEGIN LOOP ON BD
      do 101 i_bd = 0, 0 ! BEGIN LOOP ON BD
!*********************************************************************
!*********************************************************************

      d_lambda = i_bd * pas
      dbdbd = 5.77d0 * d_lambda

      e_b_gs   = e_b_gs0   - 12.208 * d_lambda

      if(e_b_gs.lt.0.d0) go to 101


!*********************************************************************

      ak_aa = sqrt ( 2.d0 * red_mass_aa * e_b_gs ) / cs_hbarc_nu
      eta_aa  = eta0_aa / sqrt ( e_b_gs )
      rho_aa = ak_aa * radius_aa
      eta = cmplx(eta_aa,0.d0)
      z = cmplx(rho_aa,0.d0)
      call wclbes(z,eta,zlmin,nl,f,g,fp,gp,sig,kfn,mode,jfail,jpr)
      if(jfail.ne.0) then
        write(*,*) ' jfail = ',jfail
        stop ' Failed '
      end if
      pen = rho_aa/(f(0)**2+g(0)**2)

      Gamma_alpha_b1 = red_Gamma_alpha_b * pen

!*********************************************************************

      write(6,2011)Gamma_alpha_b1,
     & GamN12p, GamN12m, GamN52p, GamN52m,
     & GamG12p, GamG12m, GamG52p, GamG52m
!       write(16,2011)Gamma_alpha_b1,Gamma_alpha_c1,Gamma_gamma1
2011  format(//1p,' Ga(Be)  = ',e10.4,
     & //1p,'Gn(12p) = ',e10.4,'  Gn(12m) = ',e10.4,
     & //1p,'Gn(52p) = ',e10.4,'  Gn(52m) = ',e10.4
     & //1p,'Gg(12p) = ',e10.4,'  Gg(12m) = ',e10.4,
     & //1p,'Gg(52p) = ',e10.4,'  Gg(52m) = ',e10.4//1p)
```

```
      tau_b = cs_hbarc_nu / cs_clight * 1.d-13 / Gamma_alpha_b1
      write(6,2013) tau_b
!       write(16,2013)tau_b
2013  format(' tau(Be) = ',1p,e10.4,' (s)'//)
      write(6,2012)
!       write(16,2012)
2012  format(5x,'T9',7x,'Numerical',6x,'Formula',8x,'Ratio')

!**********************************************************************
!**********************************************************************
!       do 100 i_temp = 22, mx_svtab ! BEGIN LOOP ON T
      do 100 i_temp = 1, nb_temp ! BEGIN LOOP ON T
!**********************************************************************
!**********************************************************************

!       t9 = 0.04 + i_temp * 0.01
      t9 = t9_tab(i_temp)
      bkt = t9 / cs_c9boltz
      t923 = t9 ** (2.d0/3.d0)


      l_newt = .true.
      do ii = 1, 3
      do jj = 1,2
        e_min(jj,ii) = 1.d9
        e_max(jj,ii) = 0.d0
      end do
      end do


      nb_steps_aa = nb_steps

!**********************************************************************

        nint_aa = 2
        gamow_max = GPeak0(i_aa) * T923
        gamow_max = gamow_max + nw_gamow * 4.d0*sqrt(gamow_max*bkt/3.d0)
! First interval
        e_min(i_aa,1) = e_min0
        e_max(i_aa,1) = gamow_max
        if(gamma_alpha_b1 .gt. 1.d-8)then
! Second interval
          e_min(i_aa,2) = e_b_gs - nw_reson * Gamma_alpha_b1
          e_max(i_aa,2) = e_b_gs + nw_reson * Gamma_alpha_b1
          if (e_min(i_aa,2) .lt. e_max(i_aa,1) )then
! Avoid overlap
            e_max(i_aa,1) = e_min(i_aa,2)
```

```
          end if
! Third interval ?
          if (e_max(i_aa,2) .le. gamow_max )then
             e_min(i_aa,3) = e_max(i_aa,2)
             e_max(i_aa,3) = gamow_max
             nint_aa = 3
          end if
          if(e_min(i_aa,2).lt.e_min(i_aa,1))stop 'ERROR on e_min 2 aa'
          if(e_min(i_aa,3).lt.e_min(i_aa,1))stop 'ERROR on e_min 3 aa'
        else
! Very narrow resonance
          nint_aa = 1
          nb_steps_aa = 1
        endif



!*********************************************************************

        nint_bn = 2
        gamow_max = 40*bkt  !
! First interval
        e_min(i_bn,1) = 1.d-6
        e_max(i_bn,1) = gamow_max
! Second interval
          e_min(i_bn,2) = 2.4 ! make sure to get narrow resonance
          e_max(i_bn,2) = 2.5 ! using small steps
          if (e_min(i_bn,2) .lt. e_max(i_bn,1) )then
! Avoid overlap
            e_max(i_bn,1) = e_min(i_bn,2)
          end if
! Third interval ?
        if (e_max(i_bn,2) .le. gamow_max )then
          e_min(i_bn,3) = e_max(i_bn,2)
          e_max(i_bn,3) = gamow_max
          nint_bn = 3
        end if

        if(e_min(i_bn,2).lt.e_min(i_bn,1))stop 'ERROR on e_min 2 ab'
        if(e_min(i_bn,3).lt.e_min(i_bn,1))stop 'ERROR on e_min 3 ab'


!*********************************************************************


!     Factors as in NACRE page 41
```

```
      factor_aa =  cs_avogadro * ( 8.d0*cs_pi * cs_hbarc_nu /
     & red_mass_aa**2 ) * ( red_mass_aa / ( 2.d0*cs_pi * bkt )) ** 1.5d0

      factor_bn = cs_avogadro * ( 8.d0*cs_pi / red_mass_bn**2 ) *
     & ( red_mass_bn / ( 2.d0 * cs_pi * bkt ) ) ** 1.5d0

!*****************************************************************


      sv_aan = 0.d0


      do k_aa = 1, nint_aa


      h_aa = (e_max(i_aa,k_aa)-e_min(i_aa,k_aa)) / (nb_steps-1)

      do l_aa = 1, nb_steps_aa

        e_aa = e_min(i_aa,k_aa) + h_aa * (l_aa - 1)

        eta_aa  = eta0_aa / sqrt ( e_aa )
        ak_aa = sqrt ( 2.d0 * red_mass_aa * e_aa ) / cs_hbarc_nu
        rho_aa = ak_aa * radius_aa
        eta = cmplx(eta_aa,0.d0)
        z = cmplx(rho_aa,0.d0)
        call wclbes(z,eta,zlmin,nl,f,g,fp,gp,sig,kfn,mode,jfail,jpr)
        if(jfail.ne.0) then
          write(*,*) ' jfail = ',jfail
          stop ' Failed '
        end if
        pen = rho_aa/(f(0)**2+g(0)**2)
        Gamma_alpha_b = red_Gamma_alpha_b * pen

!       sigma(alpha+alpha)/Gamma_alpha*E*Delta_E with (1+delta_aa) factor

        sig_aa= 2.d0 * cs_pi / rk2_aa * Gamma_alpha_b /
     &  ( ( e_aa - e_b_gs )**2 + Gamma_alpha_b**2/4.d0 ) * h_aa


        sum_bn = 0.d0

        kl_bn = 0

        do k_bn = 1, nint_bn

          h_bn = (e_max(i_bn,k_bn)-e_min(i_bn,k_bn)) / (nb_steps_bn-1)! deprime
```

```
      do l_bn = 1, nb_steps_bn

         kl_bn = kl_bn + 1

         e_bn = e_min(i_bn,k_bn) + h_bn * (l_bn - 1)              !eprime

         e_neutron = e_bn

         e_gamma = e_bn + e_be_ns + e_aa - e_b_gs

         sigma_coef =cs_pi*cs_hbarc_nu**2/(2.d0*red_mass_bn)

         ! Energy Dependent Widths
         ! Neutron Widths
         !GN12p = Red_GamN12p * sqrt((ERez12p - e_be_ns))
         !if (e_neutron.ge.0.0) then
          GN12p = GamN12p * sqrt(e_neutron/(ERez12p - e_be_ns))
          !GN12m = GamN12m * sqrt(e_neutron/(ERez12m - e_be_ns))
          !GN52p = GamN52p * sqrt(e_neutron/(ERez52p - e_be_ns))
          GN12m = 2.0*lil_gam_12m*(xi*e_neutron)**(1.5)/
     &     (1.0+(xi*e_neutron))
          GN52p = 2.0*lil_gam_52p*(xi*e_neutron)**(2.5)/
     &     (9.0+3.0*(xi*e_neutron)+(xi*e_neutron)**2)
         !else
         !  GN12p = GamN12p * sqrt(e_bn/(ERez12p - e_be_ns))
         !  GN12m = GamN12m * sqrt(e_bn/(ERez12m - e_be_ns))
         !  GN52p = GamN52p * sqrt(e_bn/(ERez52p - e_be_ns))
         !endif
         ! Gamma Widths
         GG12p = Ggfactor1*e_gamma**3*B_Strength12p
         GG12m = Ggfactor2*e_gamma**3*B_Strength12m
         GG52p = Ggfactor1*e_gamma**3*B_Strength52p
         GG52m = Ggfactor2*e_gamma**3*B_Strength52m
         !GG12p = GamG12p * (e_gamma/ERez12p)**3
         !GG12m = GamG12m * (e_gamma/ERez12m)**3
         !GG52p = GamG52p * (e_gamma/ERez52p)**3
         !GG52m = GamG52m * (e_gamma/ERez52m)**3

         sigma_gn_1 = 4.d0*j12 * GG12p * GN12p  /
     &     ((e_gamma - ERez12p)**2 + (GN12p+GG12p)**2/4.d0)

         sigma_gn_2 = 4.d0*j12 * GG12m * GN12m /
     &     ((e_gamma - ERez12m)**2 + (GN12m+GG12m)**2/4.d0)

         sigma_gn_3 = 4.d0*j52 * GG52p *GN52p /
     &     ((e_gamma - ERez52p)**2 + (GN52p+GG52p)**2/4.d0)
```

```
            sigma_gn_4 = 4.d0*j52 * GG52m * GamN52m /
     &      ((e_gamma - ERez52m)**2 + (GG52m+GamN52m)**2/4.d0)

            sigma_gn =  sigma_gn_1   +
     &                  B_R_12m*sigma_gn_2   +
     &                  B_R_52p*sigma_gn_3   +
     &                  B_R_52m*sigma_gn_4

            sig_bn =  sigma_coef*sigma_gn

            sum_bn = sum_bn + sig_bn * exp(-e_bn/bkt)*h_bn

          end do ! l_bn loop

         end do ! k_bn loop

!          l_newt = .false.

         sum_bn = sum_bn * factor_bn
         sv_aan = sv_aan + sig_aa * sum_bn * exp(-e_aa/bkt)


        end do ! l_aa loop

      end do ! k_aa loop

!      N_A^2 <sigma v> is in cm^6 mole^-1 s^-1 but here units are fm

!       sv_aan = sv_aan * factor_aa * cs_clight * 1.d13 * 1.d-78
      sv_aan = sv_aan * factor_aa * cs_clight * 1.d13 * 1.d-78
!      sv_aan = sv_aan + 5.26d-6 / t9**3 *exp(-21.361/t9)

      sv_aan1 =  8.759d-10 /16./3. * exp(-(e_b_gs+e_be_ns)/bkt)/bkt**3

! From eq. 4 in Nomoto et al. AA 1985 (corrected fo extra \rho's)
      sv_aan2 = cs_avogadro**2 * 3.d0**1.5d0 * 6 * cs_2pi ** 3 * 1d-65
      sv_aan2 = sv_aan2 * (cs_hbarc_nu**2/amass_a/bkt)**3
      sv_aan2 = sv_aan2 * omega_gamma / cs_hbarc_nu * cs_clight
      sv_aan2 = sv_aan2 * exp(-(e_b_gs+e_be_ns)*cs_c9boltz/t9)
      sv_aan2 = sv_aan2 + 5.26d-6 / t9**3 *exp(-21.361/t9)

! From eq. 5 in Nomoto et al. AA 1985
      aabe = 2.d0 * 5.4389d4 * Gamma_alpha_b1 * 1.d6 *
     &  exp(-cs_c9boltz * e_b_gs / t9 ) / t9**1.5d0
      beac = 3.5327d4 * Gamma_alpha_c1 * Gamma_gamma1 /
     & (Gamma_alpha_c1 + Gamma_gamma1) * 1.d6 *
```

```
     &  exp(-cs_c9boltz * e_be_ns / t9 ) / t9**1.5d0
       aang = 3.d0 * aabe * beac * tau_b
       aang = aang + 5.26d-6 / t9**3 *exp(-21.361/t9)


       sv_aan = max(sv_aan, 1.d-100)
       sv_aan2 = max(sv_aan2, 1.d-100)
       aang = max(aang, 1.d-100)

       raan =  sv_aan / sv_aan2
       raab =  sv_aan2 / aang

!        if(gamma_alpha_c1 .gt. 1.d-7)then
!          write(6,2002)t9,sv_aan
!        else
!          write(6,2002)t9,sv_aan2
!        end if

       write(6,2002)t9,sv_aan,sv_aan2,raan,nint_bn,nint_aa
!        write(16,2002)t9,log10(sv_aan),log10(sv_aan2),raan
2002   format(f10.4,1p,5e14.4)
!        stop 'TEMPO'

100    continue ! END LOOP ON T

101    continue ! END LOOP ON BD

       close(16)
1002   format('    T9    ',50f12.4)
2005   format(a8,1p,5e14.4)
       end
```

This is the contents of the file "phyconst.incl" which supplied the physical constants used in the rate code.

```
c234567
C  'PDG04' = The Review of Particle Physics, Eidelman et al., PL B592, 1 (2004)
C         and 2005 partial update for edition 2006 converted to cgs
      character*42 ch_const
      parameter (ch_const='Physical constants 03/06/09 phyconst.incl ')
C                           12345678901234567890123456789012345678901234
C-----  Math
      real*8      cs_pi, cs_2pi
      parameter (cs_pi=0.31415926535897932384626433832795028d+01)
      parameter (cs_2pi=2.d0*cs_pi)
      real*8      cs_log_2
      parameter (cs_log_2=0.69314718055994530941723212145817658d+00)
      real*8      cs_log_10
      parameter (cs_log_10=2.30258509299405d+00)
C-----  Nucl
      real*8      cs_mev2g  ! MeV to g conversion
      parameter (cs_mev2g=1.78266181d-27) ! PDG04
      real*8      cs_uma,               cs_uma_g
      parameter (cs_uma = 931.494043, cs_uma_g=1.66053886d-24) ! MeV04
      real*8      cs_mprot, cs_mneut, cs_melec
      parameter (cs_mprot=938.272029, cs_mneut=939.565360)
      parameter (cs_melec=0.510998918)
      real*8      cs_1h_uma,               cs_4he_uma
      parameter (cs_1h_uma= 1.007825032, cs_4he_uma=4.002603254)
      real*8 cs_tau_n, cs_err_tau_n
      parameter (cs_tau_n = 885.7d0, cs_err_tau_n= 0.8d0) ! PDG08
      real*8 cs_bdeut
      parameter (cs_bdeut=2.224566) ! Deuton inding energy Audi03
C-----  Phys
      real*8      cs_finesc
      parameter (cs_finesc=1.d0/137.03599911d0)
      real*8       cs_gravity,          cs_avogadro
      parameter (cs_gravity=6.6742d-8,cs_avogadro=6.0221415d23) ! PDG04
      real*8      cs_gas_constant
      parameter (cs_gas_constant=8.31434d7)
      real*8       cs_clight
      parameter (cs_clight=299792458.d2) ! PDG04
      real*8       cs_stefan
      parameter (cs_stefan=5.670400d-5) ! PDG04
      real*8       cs_aradcst
      parameter (cs_aradcst=4.d0*cs_stefan/cs_clight)
c      parameter (cs_aradcst=7.565767d-15) ! PDG04
      real*8      cs_kboltz, cs_kboltz_nu, cs_c9boltz
      parameter (cs_kboltz=1.3806505d-16) ! PDG04
      parameter (cs_kboltz_nu=8.617343d-11) ! PDG04
      parameter (cs_c9boltz = 1.e-9/cs_kboltz_nu) ! 11.605
```

```
      real*8      cs_planck,                cs_hbar
      parameter (cs_planck=6.6260693d-27, cs_hbar=cs_planck/cs_2pi) ! PDG04
      real*8    cs_hbarc,  cs_hbarc_nu ! MeV fm
      parameter (cs_hbarc=cs_hbar*cs_clight, cs_hbarc_nu=197.326968) ! PDG04
C-----  Astro /Cosmo
      real*8     cs_year2sec
      parameter (cs_year2sec=31558149.8) ! Sideral (2005)
      real*8     cs_mparsec
      parameter (cs_mparsec = 3.0856775807d24) ! PDG04
      real*8     cs_t_cmb, cs_t_nu_cmb, cs_tnuga ! (11.d0/4.d0)^1/3
      parameter (cs_t_cmb = 2.725d0)
      parameter (cs_tnuga=1.401019665d0,cs_t_nu_cmb=cs_t_cmb/cs_tnuga)
      real*8      cs_hubble100
      parameter (cs_hubble100=1.d7/cs_mparsec)
      real*8      cs_critical_density
      parameter (cs_critical_density = 3.d0*cs_hubble100**2/
     & 8.d0/cs_pi/cs_gravity) ! g/cm3

C-----  Spergel et al. ApJS 170 (2007) 377 [astro-ph/0603449]
C         (WMAP only, 1st column, Table 5 according to K.)
      real*8     cs_omega_m, cs_omega_l, cs_omega_b_h2, cs_hubble_h,
     & cs_omega_b
      parameter (cs_omega_m=0.237d0, cs_omega_l=1.d0-cs_omega_m,
     & cs_omega_b_h2 = 2.230d-2, cs_hubble_h = 0.735,
     & cs_omega_b = cs_omega_b_h2 / cs_hubble_h **2 )
C-----  Particle Physics units
      real*8 cs_pu_time, cs_pu_length, cs_pu_mass
      parameter ( cs_pu_length = cs_hbarc_nu / 1.d16 ) ! cm -> GeV-1
      parameter ( cs_pu_time = cs_pu_length / cs_clight ) ! s -> GeV-1 ???
      parameter ( cs_pu_mass = cs_mev2g * 1.d3 ) ! g -> GeV
C  e.g. cs_critical_density/cs_pu_mass*cs_pu_length**3 ! in GeV-4 JPU756
      real*8 cs_mplanck, cs_lplanck, cs_tplanck
      parameter ( cs_mplanck = 2.17645051E-05 ) ! sqrt(cs_hbarc/cs_gravity)
      parameter ( cs_lplanck = 1.61624281E-33 ) ! sqrt(hbar*G/c^3)
      parameter ( cs_tplanck = cs_lplanck / cs_clight )
```

Bibliography

[Alb04] D. E. Alburger, R. E. Chrien, R. J. Sutter, and J. F. Wishart, "Search for the three-body photodisintegration of Be", Phys. Rev. C **70**, 064611 (2004).

[Ang99] C. Angulo et al., "A compilation of charged-particle induced thermonuclear reaction rates", Nuclear Physics A **656**, 3 (1999).

[Arn96] D. Arnett, *Supernovae and Nucleosynthesis; An Investigation of the history of matter from the big bang to the present*, Princeton University Press, 1996.

[Bar83] F. Barker, "The first excited state of ^{9}Be", Can. J. Phys. **61**, 1371 (1983).

[Bar00] F. Barker, "The low-energy $^9Be(\gamma, n)^8Be$ cross section", Aus. J. Phys. **53**, 247 (2000).

[Ber67] B. L. Berman, R. L. V. Hemert, and C. D. Bowman, "Threshold Photoneutron Cross Section for Be^9", Phys. Rev. **163**, 958 (1967).

[Bir85] Y. Birenbaum, S. Kahane, and R. Moreh, "Absolute cross section for the photodisintegration of deuterium", Phys. Rev. C **32**, 1825 (1985).

[Bla52] J. M. Blatt and V. F. Weisskopf, *Theoretical Nuclear Physics*, John Wiley & Sons, Inc., 1952.

[Bur72] C. A. Burke, Ph.D. thesis, University of Oregon, 1972.

[Bur74] C. A. Burke, M. T. Lunnon, and H. W. Lefevre, "$^7Li(p, n_0)^7Be$ angular distributions to E_p = 3.8 MeV", Phys. Rev. C **10**, 1299 (1974).

[Bur10] O. Burda, P. von Neumann-Cosel, A. Richter, C. Forssén, and B. A. Brown, "Resonance parameters of the first $1/2^+$ state in ^9Be and astrophysical implications", Phys. Rev. C **82**, 015808 (2010).

[Cau62] G. R. Caughlan and W. A. Fowler, "The Mean Lifetimes of Carbon, Nitrogen, and Oxygen Nuclei in the CNO Bicycle.", apj **136**, 453 (1962).

[Cau88] G. R. Caughlan and W. A. Fowler, "THERMONUCLEAR REACTION RATES", 1988.

[Cha32] J. Chadwick, "The Existence of a Neutron", Proceedings of the Royal Society of London. Series A, Containing Papers of a Mathematical and Physical Character **136**, pp. 692 (1932).

[Cha06] M. Chadwick et al., "ENDF/B-VII.0: Next Generation Evaluated Nuclear Data Library for Nuclear Science and Technology", Nuclear Data Sheets **107**, 2931 (2006), Evaluated Nuclear Data File ENDF/B-VII.0.

[Chr66] P. R. Christensen and C. L. Cocke, "Neutron decay of the 2.43 Mev and 3.03 MeV states in 9Be to 8Be(g.s.)", Nuclear Physics **89**, 656 (1966).

[Cle68] H.-G. Clerc, K. Wetzel, and E. Spamer, "Inelastic electron scattering from ^{9}Be: Levels below 10 MeV", Nuclear Physics A **120**, 441 (1968).

[Cro91] S. Croft, "The absolute yield, angular distribution and resonance widths of the 6.13, 6.92 and 7.12 MeV photons from the 340.5 keV resonance of the ^{19}F(p,$\alpha\gamma$)^{16}O reaction", Nuclear Instruments and Methods in Physics Research Section A: Accelerators, Spectrometers, Detectors and Associated Equipment **307**, 353 (1991).

[Des01] P. Descouvemont, "Microscopic three-cluster study of the low-energy of ^{9}Be photodisinitegration", Eur. Phys. J. A **12**, 413 (2001).

[Des02] P. Descouvemont, "Microscopic study of α clustering in the ^{9,10,11}Be isotopes", Nuclear Physics A **699**, 463 (2002).

[DG92] A. De Graeve, R. Van de Vyver, A. Zieger, C. Van den Abeele, L. Van Hoorebeke, D. Ryckbosch, H. Ferdinande, F. De Smet, B. Ziegler, P. Wilhelm, and H. Arenhövel, "Absolute total cross sections for deuteron photodisintegration between 7 and 19 MeV", Phys. Rev. C **45**, 860 (1992).

[Dix91] S. Dixit, W. Bertozzi, T. N. Buti, J. M. Finn, F. W. Hersman, C. E. Hyde-Wright, M. V. Hynes, M. A. Kovash, B. E. Norum, J. J. Kelly, A. D. Bacher, G. T. Emery, C. C. Foster, W. P. Jones, D. W. Miller, B. L. Berman, and D. J. Millener, "Structure of ^{9}Be from proton scattering at 180 MeV", Phys. Rev. C **43**, 1758 (1991).

[dL03] J. R. de Laeter, J. K. Böhlke, P. De Bièvre, H. Hidaka, H. S. Peiser, K. J. R. Rosman, and P. D. P. Taylor, Pure Appl. Chem. **75**, 683 (2003).

[Edg57] R. D. Edge, "The (γ, n) reaction in ^{9}Be at intermediate energies", Nuclear Physics **2**, 485 (1956-1957).

[Efr98] V. Efros, H. Oberhummer, A. Pushkin, and I. Thompson, "Low-energy photodisintegration of ^{9}Be and $\alpha + \alpha + n \leftrightarrow ^{9}$Be at astrophysical conditions", Eur. Phys. J A , 447 (1998).

[Esh05] K. Eshwarappa, Ganesh, K. Siddappa, Y. Kashyap, A. Sinha, P. Sarkar, and B. Godwal, "Estimation of photoneutron yield from beryllium target irradiated by variable energy microtron-based bremsstrahlung radiation", Nuclear Instruments and

Methods in Physics Research Section A: Accelerators, Spectrometers, Detectors and Associated Equipment **540**, 412 (2005).

[Fie06] B. D. Fields and K. A. Olive, "Big bang nucleosynthesis", Nuclear Physics A **777**, 208 (2006), Special Isseu on Nuclear Astrophysics.

[Fre99] C. Freiburghaus, S. Rosswog, and F.-K. Thielemann, "r-process in neutron star mergers", Astrophysical Journal **525**, 121 (1999).

[Fre04] M. Freer and N. Ashwood, "Helium clustering in Be isotopes", Nuclear Physics A **738**, 10 (2004), Proceedings of the 8th International Conference on Clustering Aspects of Nuclear Structure and Dynamics.

[Fuj82] M. Fujishiro, T. Tabata, K. Okamoto, and T. Tsujimoto, "Cross section of the reaction ^{9}Be(γ, n) near threshold", Can. J. Phys. **60**, 1672 (1982).

[Gal98] R. Gallino, C. Arlandini, M. Busso, M. Lugaro, C. Travaglio, O. Straniero, A. Chieffi, and M. Limongi, "Evolution and Nucleosynthesis in Low-Mass Asymptotic Giant Branch Stars. II. Neutron Capture and the s-Process", The Astrophysical Journal **497**, 388 (1998).

[Gib59a] J. H. Gibbons and R. L. Macklin, "Total Neutron Yields from Light Elements under Proton and Alpha Bombardment", Phys. Rev. **114**, 571 (1959).

[Gib59b] J. H. Gibbons, R. L. Macklin, J. B. Marion, and H. W. Schmitt, "Precision Measurement of the $Be^9(\gamma,\ n)$ Cross Section", Phys. Rev. **114**, 1319 (1959).

[Gli91] J. P. Glickman, W. Bertozzi, T. N. Buti, S. Dixit, F. W. Hersman, C. E. Hyde-Wright, M. V. Hynes, R. W. Lourie, B. E. Norum, J. J. Kelly, B. L. Berman, and D. J. Millener, "Electron scattering from ^9Be", Phys. Rev. C **43**, 1740 (1991).

[Gor92] A. M. Goryachev, G. N. Zalesny, and I. V. Pozdnev, "Cross Section of (γ, n) Reaction on ^{9}Be in the Energy Range from Threshold to 20 MeV", Bulletin of the Russian Academy of Sciences: Physics **56** (1992).

[Ham49] B. Hamermesh, M. Hamermesh, and A. Wattenberg, "The Angular Distribution of the Photo-Neutrons from Beryllium", Phys. Rev. **76**, 611 (1949).

[Ham53] B. Hamermesh and C. Kimball, "The Photodisintegration Cross Section of Beryllium at 2.185 MeV", Phys. Rev. **90**, 1063 (1953).

[Har03] K. Y. Hara, H. Utsunomiya, S. Goko, H. Akimune, T. Yamagata, M. Ohta, H. Toyokawa, K. Kudo, A. Uritani, Y. Shibata, Y.-W. Lui, and H. Ohgaki, "Photodisintegration of deuterium and big bang nucleosynthesis", Phys. Rev. D **68**, 072001 (2003).

[Hel72] R. Hellborg and L. Ask, "The Relative Intensities and Angular Distributions of Gamma Rays from the Nuclear Reaction ^{19}F(p,$\alpha\gamma$)^{16}O", Physica Scripta **6**, 47 (1972).

[Hub89] J. H. Hubbell and S. M. Seltzer, "Tables of X-Ray Mass Attenuation Coefficients and Mass Energy-Absorption Coefficients from 1 keV to 20 MeV for Elements Z = 1 to 92", NIST Standard Reference Database 126 (1989).

[Hug75] R. J. Hughes, R. H. Sambell, E. G. Muirhead, and B. M. Spicer, "The photoneutron cross section of ^{9}Be", Nuclear Physics A **238**, 189 (1975).

[Ili07] C. Iliadis, *Nuclear Physics of Stars*, Wiley-VCH, 2007.

[Ita01] N. Itagaki, S. Okabe, and Kiyomi, "Molecular-Orbital Structure in Light Neutron Rich Nuclei", Prog. Theo. Phys. Sup. **142**, 297 (2001).

[Ita03] N. Itagaki, K. Hagino, T. Otsuka, S. Okabe, and K. Ikeda, "Importance of clustering in light neutron-rich nuclei", Nuclear Physics A **719**, C205 (2003).

[Jak61] M. J. Jakobson, "Photodisintegration of Be^9 from Threshold to 5 MeV", Phys. Rev. **123**, 229 (1961).

[Joh62] W. John and J. M. Prosser, "Photodisintegration Cross Section of Beryllium near Threshold", Phys. Rev. **127**, 231 (1962).

[Kue87] G. Kuechler, A. Richter, and W. von Witsch, "Line Shape an Excitation Strength of the First Excited State in ^{9}Be$*$", Z. Phys. A **326**, 447 (1987).

[Lan86] K. Langanke, M. Wiescher, and F. K. Thielemann, "The triple-alpha-reaction at low temperatures", Zeitschrift fr Physik A Hadrons and Nuclei **324**, 147 (1986), 10.1007/BF01325126.

[Lit97] V. N. Litvinenko et al., "Gamma-Ray Production in a Storage Ring Free-Electron Laser", Phys. Rev. Lett. **78**, 4569 (1997).

[Lod03] K. Lodders, "Solar System Abundances and Condensation Temperatures of the Elements", The Astrophysical Journal **591**, 1220 (2003).

[Mar99] R. C. Martin, J. B. Knauer, and P. A. Balo, "Production, Distribution and Applications of Californium-252 Neutrons Sources", Oak Ridge National Laboratory Report (1999).

[MCN07] MCNPX *User's Manual*, 2007. https://mcnpx.lanl.gov/

[Mob50] R. C. Mobley and R. A. Laubenstein, "Photo-Neutron Thresholds of Beryllium and Deuterium", Phys. Rev. **80**, 309 (1950).

[Mor89] R. Moreh, T. J. Kennett, and W. V. Prestwich, "$^2H(\gamma, n)$ absolute cross section at 2754 keV", Phys. Rev. C **39**, 1247 (1989).

[Muk05] I. Mukha, M. Kavatsyuk, A. Algora, L. Batist, A. Blazhev, J. Dring, H. Grawe, M. Hellstrm, O. Kavatsyuk, R. Kirchner, M. L. Commara, C. Mazzocchi, C. Plettner, and E. Roeckl, "The reaction of triple radiative capture [alpha][alpha](n,γ)^{9}Be studied in a β decay of ^{9}Li", Nuclear Physics A **758**, 647 (2005), Nuclei in the Cosmos VIII.

[Nom85] K. Nomoto, F. Thielemann, and S. Miyaji, "The triple alpha reaction at low temperatures in accreting white dwarfs and neutron stars", Astronomy and Astrophysics **149**, 239 (1985).

[Nor10] J. Nordhaus, A. Burrows, A. Almgren, and J. Bell, "DIMENSION AS A KEY TO THE NEUTRINO MECHANISM OF CORE-COLLAPSE SUPERNOVA EXPLOSIONS", Astrophysical Journal **720**, 694 (2010).

[Noy54] J. C. Noyes, J. E. Van Hoomissen, W. C. Miller, and B. Waldman, "Photodisintegration Thresholds of Deuterium and Beryllium", Phys. Rev. **95**, 396 (1954).

[Ots03] K. Otsuki, G. J. Mathews, T. Kajino, S. Honda, W. Aoki, A. Aprahamian, and K. Vaughan, "Nuclear cosmochronometry and universality in the r-process abundances", Nuclear Physics A **721**, C1024 (2003).

[Pag30] L. Page and W. W. Watson, "Nuclear Electrons", Phys. Rev. **35**, 1584 (1930).

[Per56] J. K. Perring and T. H. R. Skyrme, "The Alpha-Particle and Shell Models of the Nucleus", Proceedings of the Physical Society. Section A **69**, 600 (1956).

[Qia07] Y.-Z. Qian and G. Wasserburg, "Where, oh where has the r-process gone?", Physics Reports **442**, 237 (2007), The Hans Bethe Centennial Volume 1906-2006.

[Rus48] B. Russell, D. Sachs, A. Wattenberg, and R. Fields, "Yields of Neutrons from Photo-Neutron Sources", Phys. Rev. **73**, 545 (1948).

[Sal52] E. E. Salpeter, "Nuclear Reactions in the Stars. I. Proton-Proton Chain", Phys. Rev. **88**, 547 (1952).

[Sal70] A. Salyers, "Photodisintegration of ^9Be", Phys. Rev. C **2**, 1653 (1970).

[Sas06] T. Sasaqui, K. Otsuki, T. Kajino, and G. Mathews, "Light-Element Reaction Flow and the Conditions for r-Process Nucleosynthesis", Astrophysical Journal **645**, 1345 (2006).

[Sch05] R. Schiavilla, "Induced polarization in the ^{2}H$(\gamma, n)^2$H reaction at low energy", Phys. Rev. C **72**, 034001 (2005).

[Sek76] K. K. Sekharan, H. Laumer, B. D. Kern, and F. Gabbard, "A neutron detector for measurement of total neutron production cross sections", Nuclear Instruments and Methods **133**, 253 (1976).

[Sho99] K. Shoda and T. Tanaka, "Clusters in the photodisintegration of ^9Be", Phys. Rev. C **59**, 239 (1999).

[Sie02] L. Siess, M. Livio, and J. Lattanzio, "Structure, Evolution, and Nucleosynthesis of Primordial Stars", The Astrophysical Journal **570**, 329 (2002).

[SJ93] J. K. Sprinkle Jr., H. O. Menlove, M. C. Miller, and P. A. Russo, Los Alamos National Lab Report No. LA-12496-MS , 11 (1993).

[Smi57] A. B. Smith, P. R. Fields, and J. H. Roberts, "Spontaneous Fission Neutron Spectrum of Cf^{252}", Phys. Rev. **108**, 411 (1957).

[Sne50] A. H. Snell, E. C. Barker, and R. L. Sternberg, "Photo-Disintegration Cross Sections of Deuterium and Beryllium for the Gamma-Rays of Sodium 24 and Gallium 72", Phys. Rev. **80**, 637 (1950).

[Sum02] K. Sumiyoshi, H. Utsunomiya, S. Goko, and T. Kajino, "Astrophysical reaction rate for $\alpha(\alpha$n,$\gamma)^9$Be by photodisintegration", Nuclear Physics A **709**, 467 (2002).

[Sun09] C. Sun, Ph.D. thesis, Duke University, 2009.

[Sur10] R. Surman and G. Mclaughlin, "Private Communication", 2010.

[Ter01] M. Terasawa, K. Sumiyoshi, T. Kajino, G. Mathews, and I. Thanihata, "New Nuclear Reaction Flow During r-Process Nucleosynthesis in Supernoavae: Critical Role of Light Neutron-Rich Nuclei", Astrophysical Journal **562**, 470 (2001).

[Tho09] A. K. Thompson, "Source Activity", private communication, 2009.

[Til04] D. Tilley, J. Kelley, J. Godwin, D. Millener, J. Purcell, C. Sheu, and H. Weller, "Energy levels of light nuclei A=8,9,10", Nuclear Physics A **745**, 155 (2004).

[Uts00] H. Utsunomiya, Y. Yonezawa, H. Akimune, T. Yamagata, M. Ohta, M. Fujishiro, H. Toyokawa, and H. Ohgaki, "Photodisintegration of ^9Be with laser-induced Compton backscattered γ rays", Phys. Rev. C **63**, 018801 (2000).

[van94] L. van Wormer, J. Goerres, C. Iliadis, M. Wiescher, and F. Thielemann, "Reaction rates and reaction sequences in the rp-process", apj **432**, 326 (1994).

[vO06] W. von Oertzen, M. Freer, and Y. Kanada-En'yo, "Nuclear clusters and nuclear molecules", Physics Reports **432**, 43 (2006).

[Wüs92] S. Wüstenbecker et al., "Atomic effects on $\alpha-\alpha$ scattering to the ^{8}Be ground state", Z. Phys. A **326**, 205 (1992).

[Wel09] H. R. Weller, M. W. Ahmed, H. Gao, W. Tornow, Y. K. Wu, M. Gai, and R. Miskimen, "Research opportunities at the upgraded HIγS facility", Progress in Particle and Nuclear Physics **62**, 257 (2009).

[Woo92] S. E. Woosley and R. D. Hoffman, "The α-process and the r-process", apj **395**, 202 (1992).

[Woo94] S. E. Woosley, J. R. Wilson, G. J. Mathews, R. D. Hoffman, and B. S. Meyer, "The r-process and neutrino-heated supernova ejecta", Astrophysical Journal **433**, 229 (1994).

[Woo05] S. Woosley and T. Janka, "The physics of core-collapse supernovae", Nat. Phys. , 147 (2005).